UNIVERSIDADE FEDERAL DE MINAS GERAIS

Escola de Engenharia

Programa de Pós-Graduação em Engenharia Mecânica

Clara Estillac Leal Silva

Rotary thermomagnetic motor prototype for energy harvesting: design, production and performance characterization

Belo Horizonte
2025

Clara Estillac Leal Silva

Rotary thermomagnetic motor prototype for energy harvesting: design, production and performance characterization

Dissertação de mestrado apresentado ao curso de Pós-Graduação em Engenharia Mecânica da Universidade Federal de Minas Gerais, como requisito parcial à obtenção do grau de Mestre em Engenharia Mecânica.

Orientador: Prof. Dr. Paulo Vinícius Trevizoli

Coorientador: Prof. Dr. Marcelo Araújo Câmara

Belo Horizonte

2025

Silva, Clara Estillac Leal.
S586r Rotary thermomagnetic motor prototype for energy harvesting [recurso eletrônico] : design, production and performance characterization / Clara Estillac Leal Silva. – 2025.
1 recurso online (120 f. : il., color.) : pdf.

Orientador: Paulo Vinicius Trevizoli.
Coorientador: Marcelo Araújo Câmara.

Dissertação (mestrado) – Universidade Federal de Minas Gerais, Escola de Engenharia.

Inclui bibliografia.

1. Engenharia mecânica – Teses. 2. Desenvolvimento sustentável – Teses. 3. Resíduos metalúrgicos – Teses. 4 Motores – Teses. 5. Magnetismo – Teses. 6. Energia – Conversão – Teses. I. Trevizoli, Paulo Vinícius. II. Câmara, Marcelo Araújo. III. Universidade Federal de Minas Gerais. Escola de Engenharia. IV. Título.

CDU: 621(043)

Ficha catalográfica elaborada pelo bibliotecário Marcio A. A. Gomes CRB/6 2812
Biblioteca Prof. Mário Werneck, Escola de Engenharia da UFMG

UNIVERSIDADE FEDERAL DE MINAS GERAIS
ESCOLA DE ENGENHARIA
PROGRAMA DE PÓS-GRADUAÇÃO EM ENGENHARIA MECÂNICA

FOLHA DE APROVAÇÃO

"ROTARY THERMOMAGNETIC MOTOR PROTOTYPE FOR ENERGY HARVESTING: DESIGN, PRODUCTION AND PERFORMANCE CHARACTERIZATION"

CLARA ESTILLAC LEAL SILVA

Dissertação submetida à Banca Examinadora designada pelo Colegiado do Programa de Pós-Graduação em Engenharia Mecânica da Universidade Federal de Minas Gerais, constituída pelos Professores Dr. Paulo Vinicius Trevizoli (Orientador - Departamento de Engenharia Mecânica-UFMG), Dr. Marcelo Araújo Câmara (Coorientador-Departamento de Engenharia Mecânica-UFMG), Dr. Jader Riso Barbosa Jr (Universidade Federal de Santa Catarina) e Dr. Tino Gottschall (Helmholtz-Zentrum Dresden-Rossendorf), como parte dos requisitos necessários à obtenção do título de **"Mestre em Engenharia Mecânica"**, na área de concentração de **" Energia e Sustentabilidade"**.

Dissertação aprovada no dia 16 de julho de 2025.

Por:

Documento assinado eletronicamente por **Paulo Vinicius Trevizoli**, **Professor do Magistério Superior**, em 27/07/2025, às 19:50, conforme horário oficial de Brasília, com fundamento no art. 5º do Decreto nº 10.543, de 13 de novembro de 2020.

Documento assinado eletronicamente por **Marcelo Araujo Camara**, **Professor do Magistério Superior**, em 28/07/2025, às 14:35, conforme horário oficial de Brasília, com fundamento no art. 5º do Decreto nº 10.543, de 13 de novembro de 2020.

Documento assinado eletronicamente por **Jader Riso Barbosa Junior**, **Usuário Externo**, em 30/07/2025, às 20:13, conforme horário oficial de Brasília, com fundamento no art. 5º do Decreto nº 10.543, de 13 de novembro de 2020.

Documento assinado eletronicamente por **Tino Gottschall**, **Usuário Externo**, em 02/08/2025, às 16:10, conforme horário oficial de Brasília, com fundamento no art. 5º do Decreto nº 10.543, de 13 de novembro de 2020.

A autenticidade deste documento pode ser conferida no site https://sei.ufmg.br/sei/controlador_externo.php?acao=documento_conferir&id_orgao_acesso_externo=0, informando o código verificador **4413036** e o código CRC **ECE4004A**.

To my parents, Betânia and Valdir,
who have dedicated their lives so that I could choose my own path.

ACKNOWLEDGEMENTS

I am profoundly grateful and would like to express my heartfelt thanks to my advisor, Prof. Paulo Vinícius Trevizoli. His patience, encouragement, knowledge, and experience were indispensable to the development of my master's research and to my personal growth as a researcher. He stands as a true example of determination, mentorship, and academic excellence. His work as the founder and coordinator of StreamLab continues to impress me and will undoubtedly remain a lasting source of inspiration.

My sincere thanks to my co-advisor, Prof. Marcelo Câmara, whose guidance was fundamental in patiently bringing the ideas of this work to fruition. He has consistently demonstrated exceptional mentorship, both within and beyond the engineering field, and has played a significant role in shaping my development as a researcher and individual. Also, I am very thankful to all of the StreamLab professors: Prof. Thiago Torres, Prof. Carmela Braga and Prof. Hugo Michel.

Besides, I would like to thank the committee: Dr. Tino Gottschall and Prof. Jader Riso Barbosa Jr. for their time and contributions to this master's thesis.

I would like to express my gratitude to the financial support from Fundação de Amparo à Pesquisa do Estado de Minas Gerais (FAPEMIG), through scholarship and Grants No. APQ-00877-21 (Demanda Universal) and No. APQ-00735-23 (Demanda Universal); Conselho Nacional de Desenvolvimento Científico e Tecnológico (CNPq) through Grant No. 405970/2021-8; and Centro de Termografia Científica (CEMTEC) for its support in the development of this work. I am also thankful to the Universidade Federal de Minas Gerais and to the Programa de Pós-Graduação em Engenharia Mecânica (PPGMEC).

I would also like to express my gratitude to my colleagues and dear friends from the StreamLab team: Dalila Torres, Vinícius de Jesus, Higor Rios, Marcos Tadim, Pedro Chaves, Arthur Pires, Lívia Soledade, Matheus Bastos and Renan Reis. This achievement was truly the result of collective effort; it took a village. Without each of you, this work would not have been possible. Thank you as well for your sincere support; your friendship and good humor helped ease the challenges along the way and made this journey genuinely fun and enjoyable. Thanks also to my other friends that have somehow contributed to this master's degree, either with technical or emotional support: Prof. Pedro Bastos, Prof. Rafael Ferreira, Prof. Luiz Fernando, Prof. Luis Antônio and Francielle Paz.

I am deeply grateful to my entire family. First and foremost, to my parents, Betânia Estillac and Valdir Silva, for their constant support in every aspect of my life. To my brother, Caio Estillac; my godparents, Elisa and Eduardo Estillac; and my aunt, Juliana Moraes. To my cousins, my lifelong companions, Bernardo Estillac, Lucas Estillac, Sarah

Estillac, Manuela Moraes, and Amanda Moraes. You are my foundation and knowing that I have you by my side gives me strength to face every challenge. Thanks also to my little friends, Jude and Dingo, for always being there for me.

I would also like to thank my beloved fiancé, Rafael Borges. You have stood by my side throughout this entire journey, always cheering me up. It is a true privilege to share my life with you. Thank you for your love, patience and companionship.

Last but not least, I am grateful to πR. You have been my greatest challenge so far, but also my most valuable teacher, showing me that patience and persistence do pay off. I have grown with you, both as a researcher and as a person. Today, I am more experienced, braver, and more resilient. I hope you continue to inspire and challenge many others; if so, then my work will not have been in vain. It has been a remarkable journey, thank you.

“Nasce um projeto.
Primeiro é areia fofa.
Impulso e querer partir.
As pessoas do entorno assitem aos passos.
Mapeiam as pegadas perenes que acabam na faixa de areia escura.

.

Ali, a água cobre os passos, os pés já são comidos pelo fundo.
É fácil saltar sobre as ondas pequenas.
Os rabiscos, os ensaios, as ideias libertam e não exigem compromisso.

.

As ondas médias trazem frio às pernas,
às coxas, o limite está na altura do umbigo e rouchhh!
Já se tem medo, já se sente falta.

.

Empurra-se o peito contra a força do mar.
Os cumes crescem e ameaçam tomar o corpo. Avançar é duro.
Chuta-se o fundo e atira-se o corpo contra as paredes líquidas.
Sente o sal, a epuma, o turbilhão suga os braços e os cabelos.
Boca seca, ardem os olhos.
Faltam referências, pontos fixos, falta ar.
Encontra-se força na vontade de chegar,
o destino explica o ponto de partida, o sonho explica a razão.
Cada onda é uma batalha que pede e toma tudo.
Avança-se aos quase nadas.
Às vezes a onda nos dá brecha, às vezes nos leva pra trás.

.

Não dá pé.
A cabeça imersa, presa a respiração.
Cada cume e vale é uma nova aposta de que essa fase
vai passar.

.

Passa. E a língua do mar é grande demais
para conter um corpo em ação.
As pequenas grandes ondas estão nas costas.
O mar aberto à frente mostra um
horizonte possível e sem fim.
Em uma praia, em outro lado, as ondas serão a favor da chegada.
E, ao chegar, o projeto tem fim."
(De cara para o vento, Tamara Klink)

ABSTRACT

Low-grade waste heat is abundantly available in most energy conversion processes, however, its low temperature, typically defined as below 100°C, limits the efficiency of conventional thermal cycles. As a result, it remains largely untapped, representing a significant recovery potential. In this context, thermomagnetic motors (TMM) emerge as an alternative for converting this waste heat into usable mechanical energy, thereby improving the overall efficiency of existing systems. The present dissertation is devoted to the design, production and performance characterization of a novel rotary TMM prototype with a fin rotor. A stationary L-shaped magnetic circuit (MC), comprising four magnetic field volumes, was designed using COMSOL Multiphysics (AC/DC module formulation) simulations. The MC was subsequently manufactured and assembled in-house, and its magnetic field was experimentally characterized. Thin gadolinium (Gd) plates, available in the laboratory, were then employed as magnetocaloric material (MM) fins for the rotor. Finally, the transmission system, consisting of a bipartite shaft and corresponding upper and lower house bearings, was manufactured and assembled, completing the production of the TMM prototype. For the performance characterization tests, a fluid treatment and distribution station was used to supply the fluid streams required for the motor operation, as well as for measuring all the relevant operational parameters. The tests were conducted using both the two- and four-magnetic-volumes configurations of the MC, under multiple temperature and flow rate conditions. Regarding the fluid stream temperatures, tests were carried out using the two-magnetic volumes configuration, with warm fluid temperatures ranging from 35°C to 50°C combined with cold fluid temperatures of 5°C and 10°C, at a flow rate of 10 LPM per nozzle (LPM/nozzle), corresponding to a total flow rate of 20 LPM. As for the flow rate conditions, tests were performed with flow rates ranging from 5.0 to 22.5 LPM/nozzle for the two-magnetic volumes configuration and from 5.0 to 11.75 LPM/nozzle for the four-magnetic volumes configuration. In this case, cold and warm fluid temperatures were held constant at 5°C and 45°C, respectively. Torque and rotational speed were measured in all tests, allowing the experimental characterization of torque versus speed and produced power versus speed curves. The developed prototype presented metrics that outperformed state-of-the-art TMM prototypes, with a maximum rotational speed of 348.5 RPM, a holding torque of 2.3 N·m and a maximum produced power of 4.6 W. Finally, the results enabled discussions on the influence of the number of magnetic field volumes, as well as fluid stream temperatures and flow rates, on TMM performance.

Keywords: sustainable development; waste heat recovery; energy conversion; energy harvester; thermomagnetic motor; magnetic circuit; magnetocaloric materials; TRL4 prototype; torque and mechanical power.

RESUMO

Rejeitos térmicos de baixo nível então presentes em abundância na maioria dos processos de conversão de energia, entretanto, sua baixa temperatura, tipicamente definida como inferior a 100°C, limita a eficiência dos ciclos térmicos convencionais. Como resultado, essa energia permanece em grande parte inexplorada, representando um potencial de recuperação significativo. Nesse contexto, motores termomagnéticos (MTMs) emergem como uma alternativa para converter esse rejeito em energia mecânica útil, melhorando a eficiência de sistemas existentes. A presente dissertação tem como objetivo o projeto, fabricação, e caracterização do desempenho de um novo protótipo de MTM com rotor de aletas. Um circuito magnético (CM) estacionário em formato de L, contendo quatro volumes magnéticos, foi projeto utilizando simulações implementadas no COMSOL Multiphysics (formulação AC/DC). O CM foi, em sequência, fabricado e montado internamente, e o campo magnético foi caracterizado experimentalmente. Placas delgadas de gadolínio (Gd), disponíveis no laboratório, foram utilizadas como as aletas de material magnetocalórico (MM) do rotor. Finalmente, o sistema de transmissão, composto por um eixo bipartido e seus respectivos mancais superior e inferior, foi fabricado e montado, completando a fabricação do protótipo do MTM. Para os testes de caracterização de desempenho, foi utilizada uma estação de tratamento e distribuição de fluido para suprir as correntes de fluido necessárias para a operação do motor, bem como para medir todos os parâmetros operacionais relevantes. Os testes foram realizados utilizando ambas as configurações com dois e quatro volumes magnéticos do CM, para diversas condições de temperatura e vazões. Em relação às temperaturas das correntes de fluido, testes foram feitos utilizando a configuração de dois volumes magnéticos, com as temperaturas da corrente quente variando de 35°C a 5°C combinadas com as temperaturas do fluido frio de 5°C e 10°C, a uma vazão de 10 LPM por bocal (LPM/bolcal), correspondente a uma vazão total de 20 LPM. Já para as condições de vazão, os testes foram conduzidos para vazões variando de 5 a 22.5 LPM/bocal para a configuração de dois volumes magnéticos e de 5 a 11.75 LPM/bocal para a configuração de quatro volumes magnéticos. Nesse caso, as temperaturas dos fluidos frio e quente foram mantidas constantes em 5°C e 45°C, respectivamente. Torque e velocidade de rotação foram medidas em todos os testes, permitindo a caracterização experimental das curvas de torque versus velocidade e potência produzida versus velocidade. O protótipo desenvolvido apresentou métricas de desempenho que superaram protótipos de MTM do estado-da-arte, com uma velocidade máxima de 348,5 RPM, um torque máximo de 2,3 N·m e uma potência produzida máxima de 4,6 W. Finalmente, os resultados possibilitaram a discussão sobre a influência do número de volumes magnéticos, bem como da temperatura e da vazão das correntes de fluido, no desempenho do MTM.

Palavras-chaves: desenvolvimento sustentável, reaproveitamento de rejeito térmico; conversão de energia; motores termomagnéticos; circuito magnético; materiais magentocalóricos; protótipo TRL4; torque e potência mecânica.

List of Figures

List of Tables

List of abbreviations and acronyms

Acronyms

MC	Magnetic Circuit
MCE	Magnetocaloric Effect
MHE	Magnetic Heat Exchanger
MM	Magnetic Material
PLC	Programmable Logic Controller
TMM	Thermomagnetic Motor

List of symbols

A	MM cross sectional area	[m^2]
B	Magnetic flux density	[T]
B_r	Remanence	[T]
F	Force	[N]
H	Magnetic field	[A/m]
H_c	Coercivity	[A/m]
H_{dem}	Internal demagnetizing field	[T]
l	MM length	[m]
M	Magnetization	[A.m^2]
N_D	Demagnetization factor	[-]
Nu	Nusselt number	[-]
Re	Reynolds number	[-]
S_e	Electronic entropy	[J/K]
S_l	Lattice entropy	[J/K]
S_m	Magnetic entropy	[J/K]
T	Temperature	[K]
T_T	Magnetic phase transition temperature	[K]
$\dot{W}$	Power	[W]

Greek

$\dot{\vartheta}$	Volumetric flow rate	[LPM]
μ_r	Relative magnetic permeability	[T/m.A]
σ	Specific magnetization	[A.m^2/kg]
τ	Torque	[N.m]
Φ	Magnetic induction	[T.m^2]

χ	Magnetic susceptibility	[emu/cm^3.Oe]
ω	Rotational speed	[RPM]

Composed Symbols

ΔP	Pressure drop	[kPa]
ΔT_{ad}	Adiabatic temperature change	[K]

Subscripts and Superscripts

apl	Applied
C	Cold stream variables
H	Warm stream variables
h	High
l	Low
prod	Produced
R	Reference
res	Resulting
*	Dimensionless

Constants

μ_0	Magnetic permeability of vacuum	$4\pi \times 10^{-7}$ T.m/A

Contents

1 INTRODUCTION

Global energy demand has steadily increased over the past few decades, and this trend is expected to continue at a rate of 0.5% over the next ten years (INTERNATIONAL ENERGY AGENCY, 2021). To meet this growing demand, fossil fuels are preferred for primary energy production, as they are well-established and relatively inexpensive. However, these conventional energy sources are major contributors for greenhouse gas emissions and other pollutants, further aggravating global warming. In 2015, the Paris Agreement (UNFCCC, 2015) proposed limiting global warming to 1.5°C by reducing harmful emissions to a net zero by 2050. To achieve this goal and mitigate the environmental impact of fossil fuel use, it is essential to take several key actions, notably the development of renewable energy technologies and the enhancement of the efficiency of conventional energy systems.

Concerning to the latter, waste heat recovery technologies emerge as a promising alternative, especially because approximately 50% of the global energy input is lost as waste heat (FORMAN et al., 2016; FIRTH et al., 2019). In addition, 60% of the waste heat exhibits temperatures lower than 100°C (categorized as low-grade waste heat) and can be found across a wide range of industrial processes. The main sources of low-grade waste heat are exhaust gases from heating systems, such as burners, furnaces, industrial dryers, and heat exchangers, and cooling water for industrial ovens (HUR et al., 2023). Despite its abundance, low-grade waste heat has a low Carnot efficiency and, from an exergy perspective, as it represents only 21% of the overall rejected heat potential. Nevertheless, it still offers an opportunity to improve the efficiency of conventional thermal systems and, for that purpose, innovative technologies are essential.

Energy harvesters are technologies used to convert low-grade waste heat into usable energy. The Rankine Organic Cycle and the Kalina Cycle are alternative energy conversion cycles that utilize organic fluids with lower boiling points than water to harness energy. Although these cycles remain the leading technologies in this field, they require complex power plants with costly components, and their rights are concentrated among a few companies. Therefore, solid-state energy harvesters, although typically exhibiting low efficiencies between 1% and 10%, emerge as a promising alternative, as they offer several advantages, such as the absence of harmful discharges during operation, minimal maintenance requirement, low operational costs, compactness, robustness, and self-sufficiency, enabling their use in remote locations. Among the main solid-state technologies are thermoelectric generators, pyroelectric systems, thermoelastic systems, thermogalvanic cells, and thermomagnetic systems (KISHORE; PRIYA, 2018b). Thermomagnetic devices can be categorized into generators and motors, in which generator directly convert the waste heat into electricity and the motors convert it into mechanical energy (KISHORE; PRIYA,

2018a).

Thermomagnetic motors (TMM) operate based on the temperature dependence of the magnetic properties of soft-ferromagnetic materials near their magnetic phase transition temperature (T_T). These devices typically feature a magnetic field source, a magnetic material heat exchanger (MHE), and pumping systems for supplying warm and cold fluid streams. Their operation relies on creating a force imbalance between the magnetic force and a second type of force, which could be an elastic, gravitational, or magnetic force, depending on the design of the prototype. The magnetic force is proportional to the MM's temperature-dependent specific magnetization, and it varies by supplying flows of warm and cold fluids during specific phases of the thermodynamic cycle.

As a result of the force imbalance, the TMM produces either reciprocating or rotary motion. Reciprocating devices are characterized by non-continuous and low-frequency operation. Depending on the design, it may be necessary to counterbalance the magnetic force by using an additional mechanism, such as a spring (elastic) or gravitational force, which limits the operational frequency. They may also require complex valving systems due to the alternating flow of warm and cold fluids through the MHE during different periods of the thermodynamic cycle. Rotary devices, on the other hand, rely only on the magnetic force imbalance, enabling continuous operation at higher frequencies. However, depending on the design, they may face similar complexities regarding fluid flow systems.

The first TMM patent was proposed by Tesla (1889). However, due to technological limitations related to the magnetic field generation and the MM's properties, research in this field did not advance significantly throughout the 20^{th} century. In recent years, advancements in respect to permanent magnets with high $B - H$ energy (CROAT et al., 1984; SAGAWA et al., 1984), magnetic circuits (MC) geometries and designs (HALBACH, 1980; BJøRK et al., 2010), and in novel magnetocaloric materials with transition temperatures around room-temperature (GSCHNEIDNER; PECHARSKY, 2000) have revitalized the studies in this research field. To date, approximately 60 patents have been proposed, but only a few prototypes have been built and tested (MURAKAMI; NEMOTO, 1972; TAKAHASHI et al., 2006; FRANZITTA et al., 2013; KISHORE et al., 2020; KANEKO et al., 2021; MEHMOOD et al., 2021; RIOS et al., 2024).

Most existing prototypes still exhibit limited torque outputs and fail to sustain continuous motion, which restricts their rotational speed. These limitations can primarily be attributed to two factors: first, the inadequate design of the magnetic field source, resulting in low intensity and poorly distributed magnetic flux densities, crucial for achieving higher torques; and second, ineffective heat transfer between the MM and the working fluid streams, which increases the time required for the MM to shift its magnetic phase, thereby reducing operational frequencies.

In this context, the present research proposes the design, production, and experimental

testing of a novel rotary thermomagnetic motor. The design was oriented toward the main goal of developing a prototype capable of operating continuously at speeds on the order of 180 RPM (3 Hz). To achieve this, the initial decision was to design a rotary device in which the MM would be free to spin, while the magnetic field source remains stationary. Then, significant efforts were dedicated to the proper design and construction of the magnetic field source, aiming to enhance the magnetic field intensity and its gradient distribution along the desired direction. Furthermore, the interaction between the magnetic field gradient and the MM was thoroughly investigated. The MM geometry must enable rapid temperature variation, which require high thermal capacity fluid flows combined with effective heat transfer. Therefore, by supplying warm and cold fluids at appropriate locations within the field gradient distribution, it is possible to achieve the target performance metrics. As will be presented and discussed throughout this master's thesis, the built and tested prototype advances the current state-of-the-art by demonstrating experimental metrics for rotational speed, torque, and power output that surpass those of previously reported prototypes in the open literature.

1.1 OBJECTIVES AND CONTRIBUTIONS

The objective of the present dissertation is to design, construct and experimentally characterize a novel rotary thermomagnetic motor for energy harvesting applications.

To accomplish this objective, the following activities were pursued:

- Identify the key parameters for designing a successful TMM;
- Design, fabricate and assemble, *in house*, the novel concept of TMM, including a permanent magnet magnetic circuit, the MM rotor, and the transmission system;
- Develop a fluid distribution system to evenly supply the warm and cold streams at their respective regions of the rotor through properly designed nozzles;
- Perform experimental test under different operating conditions of warm and cold streams temperature and flow rates, and experimentally characterize torque and rotational speed;
- Construct the torque versus speed and power versus speed characteristic curves for motors, and evaluate the influence of different operational conditions on these curves.

1.2 OUTLINE OF THE DISSERTATION

The present dissertation was divided into six chapters as follows. In chapter 2 – *Fundamentals* – the fundamentals for TMM are presented, from the magnetism principle and

magnetic material properties to TMM main components, types, and operational principles. The thermodynamic cycle of TMM is also discussed. In Chapter 3 – *State of the Art* – a review of energy harvesting technologies and TMM prototypes is presented. Additionally, a comprehensive overview of TMM-related patents to date is provided. Chapter 4 – *Materials and Methods* – describe the designing and production processes of the experimental apparatus, including the MC, the rotor and transmission system and the fluid distribution station required for the motor operation. The chapter also details the experimental procedures, the data acquisition, and post-processing for the performance characterization tests. Chapter 5 – *Results and Discussion* – presents the numerical and experimental results for the MC, as well as the experimental results for the TMM performance. In addition, the influence of the operational parameters on the performance results is quantified and discussed. Finally, Chapter 6 summarizes the final considerations and recommendations for future works.

2 FUNDAMENTALS

2.1 MAGNETISM

Magnetism can be demonstrated as the capacity of a force field to attract ferrous objects acting at a distance. The origin of this magnetism in solids arises from the alignment of the magnetic moments of their atomic electrons. Once the magnetic moments are aligned, there is a magnetic charge neutralization inside the material. However, neutralization discontinuities on the material edges result in a free magnetism charge, which produces an external magnetic field and causes it to be attracted by the applied magnetic field (COEY, 2010). There are various types of magnetic ordering, including ferromagnetic, antiferromagnetic, and ferrimagnetic materials. Materials that do not magnetically order when submitted to an external field can be classified as either paramagnetic or diamagnetic. A closer examination of these categories follows below.

Ferromagnetic materials, such as iron, nickel, and some rare earths, are materials that have their electronic magnetic moments aligned in parallel independently of their submission to an external magnetic field. However, it is unusual to obtain those materials in a magnetized state on regular conditions, which can be explained by the magnetic domains theory proposed by Weiss (1906). The theory suggests that ferromagnetic materials are divided into several magnetic domains and that the magnetic moments of each of these domains are spontaneously aligned in different directions, canceling each other and resulting in a non-magnetic overall state. Therefore, for magnetizing those materials, it is necessary to apply an external magnetic field to them, aligning all their domains in the same direction. Moreover, these materials have a characteristic temperature, also known as magnetic phase transition temperature (T_T), above which the alignment of the electronic magnetic moments disappear, and the material begins to exhibit paramagnetic behavior (SPALDIN, 2010). Thermomagnetic motors operate based on the ferro-paramagnetic phase transition around T_T.

Nevertheless, if the magnetic moments tend to align antiparallel rather than parallel, it leads to antiferromagnetism or ferrimagnetism, depending on the topology of the material's crystal lattice (COEY, 2010). Antiferromagnetic materials have two interleaved identical electronic sublattices, each of which are spontaneously magnetized below a certain critical temperature. However, these equivalent magnetic moments are aligned in opposite directions, resulting in zero net spontaneous magnetization and a response to external fields similar to that of paramagnetic materials. In ferrimagnetic materials, by contrast, the interleaved electronic sublattices are inequivalent, meaning that the magnetization of one sublattice is greater than that of the oppositely oriented sublattice. As a

result, a net spontaneous magnetization is present below a critical temperature, even in the absence of an applied magnetic field.

Furthermore, paramagnetism occurs only in materials that exhibit net magnetization but whose magnetic moments are only weakly coupled to each other. As a result, their alignment is reduced by particles thermal agitation, weakening the material attraction by an externally applied magnetic field. Diamagnetism, by contrast, is a change in orbital motion that occurs in all materials when they are submitted to an external magnetic field. However, it is such a weak phenomenon that it is typically overshadowed by much stronger interactions in materials that have net magnetization. As a result, only materials that do not exhibit net magnetization are classified as diamagnetic (SPALDIN, 2010).

Finally, ferromagnetic materials can be further classified into soft and hard ferromagnetic materials. Soft ferromagnetic materials, such as ferrosilicon, permalloy (iron-nickel alloy), and ferrites, as well as pure elements like iron, cobalt, and nickel, are considered temporary magnets. They become magnetized when subjected to an external magnetic field and lose their magnetization once the field is removed. Conversely, hard ferromagnetic materials, such as Alnico (an alloy of aluminum, nickel, and cobalt) and permanent magnets like NdFeB (neodymium-iron-boron) and SmCo (samarium-cobalt), exhibit permanent spontaneous magnetization at sufficiently low temperatures. Once magnetized by an applied field strong enough to reach saturation, they retain their magnetization even after the external field is removed (COEY, 2010).

2.2 MAGNETIC PROPERTIES

A thorough understanding of the magnetic properties of materials is essential for their proper selection and use in practical applications. First, the magnetic induction (Φ) is defined as the material's response to an applied magnetic field (H). The relationship between Φ and H is given by Eq. 4.2, in which $M(H,T)$ denotes the material's magnetization and μ_o represents the magnetic permeability of vacuum ($4\pi \times 10^{-7}$ T.m/A). $M(H,T)$ is a magnetic property associated with the electronic magnetic moments alignments and it's a function of both H and the MM's temperature. The magnetic flux density (B) is the magnetic induction inside the medium and, therefore, is related to Φ through Eq. 2.2, in which A represents the MM cross sectional area (SPALDIN, 2010).

$$\Phi = \mu_o(H + M) \tag{2.1}$$

$$B = \frac{\Phi}{A} \tag{2.2}$$

Likewise, susceptibility (χ) and permeability (μ) are magnetic properties that indicate how a material's magnetization varies with the applied magnetic field. The susceptibility

χ informs on how susceptible a MM is to this applied field and it can be calculated as the magnetization ratio to the applied magnetic field. Ferromagnetic materials exhibit a magnetic susceptibility that is significantly greater than one, while paramagnetic materials have a susceptibility only slightly above one. The permeability μ, also referred to as relative permeability (μ_r) indicates how permeable a MM is to an applied magnetic field. It can be calculated as the ratio of magnetic induction to the applied magnetic field. In ferromagnetic materials, the higher the μ_r, the greater the intensity of the magnetic field resulting from the magnetic moments alignment (FARIA, 2005). In addition, a material's magnetization also depends on its temperature. The magnetic phase transition temperature (T_T) is a characteristic point below which the alignment of magnetic moments increases, resulting in higher magnetization, and above which this ordering is reduced, leading to lower magnetization (COEY, 2010).

Material's intrinsic magnetic properties depend on its resulting magnetic field (H_{res}) acting inside the material. H_{res} is smaller than the applied field (H_{apl}) by an amount equal to the internal demagnetizing field (H_{dem}), as given by Eq. 2.3. H_{dem} is, therefore, a magnetic loss caused by an internal magnetic field, opposing the applied magnetic field, that is generated during the magnetization of a sample. It is a function of a demagnetization factor N_D, which depends only on the material's geometry and ranges from 0 to 1 (Eq. 2.4)[1]

$$H_{res} = H_{apl} - H_{dem} \tag{2.3}$$

$$H_{dem} = N_D M \tag{2.4}$$

Finally, it is also important to define the magnetic force (F_{mag}), shown in Eq. 2.5, in which ρ is the MM specific mass, ϑ is the MM volume, ∇B is the magnetic flux density gradient, and σ is the MM specific magnetization, which is a function of its temperature (T) and the resulting magnetic field (H_{res}) (GAMA et al., 2016). Therefore, the magnetic force is directly proportional to the MM mass, the MM magnetic properties (σ), and the magnetic field source properties, including the intensity of the magnetic field and the magnetic flux density gradient.

$$F_{mag} = -\rho\vartheta\sigma\left(T, H_{res}\right)\nabla B \tag{2.5}$$

[1] Equations 2.3 and 2.4 are presented here in a simplified form for didactic purposes. It is acknowledged that the demagnetization factor is a second-order tensor, while the magnetic fields are vector quantities. (SPALDIN, 2010).

Figure 2.1 – Permanent magnets hysteresis loop. Source: (FURLANI, 2001)

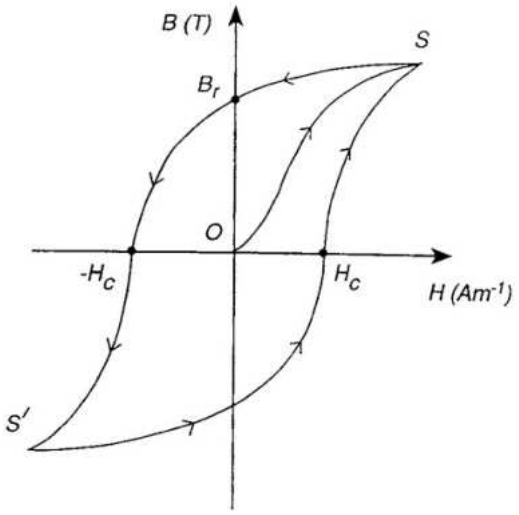

2.2.1 PERMANENT MAGNETS

Ferromagnetic materials exhibit magnetic hysteresis, which prevents their magnetization from being reduced to zero once the external magnetic field has been removed. Permanent magnets, which are hard ferromagnetic materials, present broad hysteresis loops, as shown in Fig. 2.1, in which magnetic induction (B) is plotted as a function of the magnetic field (H). The material, initially at a non-magnetic state (position O), is submitted to an external magnetic field until its magnetization reaches its saturation value (position S). From this point forward, if the applied magnetic field is removed, the material remains magnetized with a slightly lower magnetization than its saturation. The magnetic induction that remains on the material after the magnetic field has been removed is named remanence (B_r). Subsequently, to demagnetize the permanent magnet, it is necessary to apply a magnetic field direction opposite to its magnetization, with an intensity known as coercivity (H_c). To reinstitute permanent magnet properties after demagnetization, it is necessary to re-submit it to an external magnetic field. The demagnetization curve points ($B-H$) also have their energy product distribution, with a maximum value (BH_{max}), on the interval between $H = 0$ and $H = -H_c$ (FURLANI, 2001). It is also important to mention that permanent magnets can lose their remanence if heated above their maximum operating temperature. This property is particularly critical in thermomagnetic motor applications, as it constrains the maximum allowable temperature of the warm reservoir or the input waste heat.

The remanence of a permanent magnet represents the maximum magnetic flux density it can produce. However, when the magnet is properly integrated into a magnetic circuit (MC), it is possible to generate magnetic field intensities within an air gap that exceed the magnet's remanent field (COEY, 2002). Thus, properly selecting permanent magnets

Figure 2.2 – Comparison between first-order (blue lines) and second-order (dashed line) transition magnetization as a function of temperature curves. Source: (SILVA, 2022)

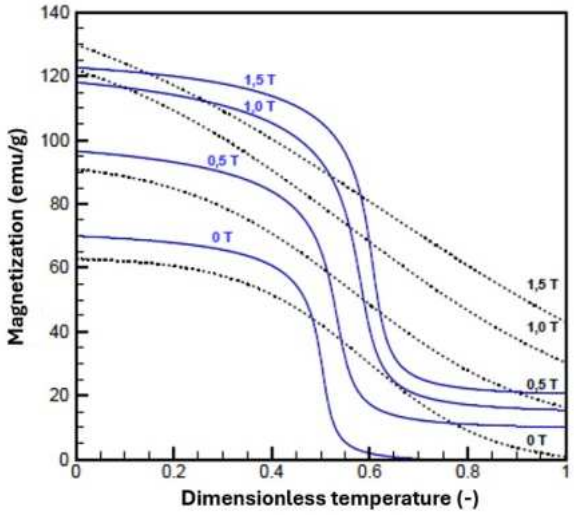

for a MC is a crucial task for obtaining the designed magnetic field intensity. In this context, NdFeB permanent magnets stand out for their BH_{max} energy values and exhibit high coercivity and remanence, being the most used for the MC of the state-of-the-art thermomagnetic devices (KISHORE; PRIYA, 2018a).

2.2.2 MAGNETOCALORIC MATERIALS: TYPES OF PHASE TRANSITION

Within the broad category of magnetic materials, magnetocaloric materials (MM) are distinguished for exhibiting the Magnetocaloric Effect (MCE).These materials can be classified according to the type of phase transition: first-order or second-order (LYUBINA, 2017). First-order materials couple a magneto-structural or magneto-elastic transition (PECHARSKY; GSCHNEIDNER JR., 1997; PLANES et al., 2009; SKOKOV et al., 2012). Second-order materials present only a change in the magnetic ordering.

A comparison between the two transition types is depicted in the $M \times T$ curves in Fig. 2.2. It is observed that the first-order transition occurs more abruptly and, consequently, in a narrower temperature range, than the second-order transition. Nevertheless, first-order magnetic materials exhibit thermal and magnetic hysteresis (GUTFLEISCH et al., 2016). The thermal hysteresis can be visualized as a difference in the magnetic properties when comparing the heating and cooling processes at a fixed external field, as illustrated in Fig. 2.3. As a result, the internal area of the temperature-entropy ($T - s$) diagram is broader, but it tends to reduce the useful MCE (CHRISTIAANSE et al., 2017).

Regarding the use of first-order materials in TMM, thermal hysteresis represents a trade-off. On one hand, the larger internal area of the $T - s$ diagram reflects an enhancement in the specific work of the thermodynamic cycle. On the other hand, it leads to longer cycle periods, reducing the produced power. Therefore, the advantage of using first-order

Figure 2.3 – First-order MM s-T diagram with thermal hysteresis. Source: (de JESUS et al., 2024)

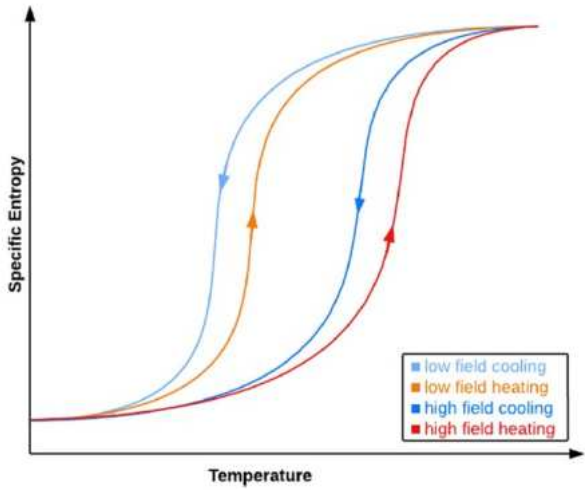

magnetic materials in TMM must be evaluated during the TMM design, taking into account both the magnetocaloric material and the heat transfer properties (de JESUS et al., 2024).

2.2.3 MAGNETOCALORIC EFFECT

The Magnetocaloric Effect (EMC) is the material's response to variations in the applied magnetic field, manifesting either as an isothermal entropy change (ΔS_{mag}) or as an adiabatic temperature change (ΔT_{ad}), as shown in Fig. 2.4.The total entropy of MM can be divided into three contributions: the electronic entropy (S_e), the lattice entropy (S_l) and the magnetic entropy (S_m), all of which are a function of temperature, at constant pressure. In particular, the magnetic entropy also depends on the applied magnetic field. Since the electronic and lattice entropy components depend solely on the temperature, they remain constant when the MM is submitted to a magnetic field variation under isothermal conditions. In contrast, the magnetic entropy component changes due to its additional dependence on the magnetic field intensity. Therefore, the MCE is observed as an isothermal entropy variation equivalent to the change in magnetic entropy. Alternatively, the MCE manifests as an adiabatic temperature change when the magnetic entropy varies in response to a change in the applied magnetic field. In response, the electronic and lattice entropies change equally in magnitude but in opposite sign to the magnetic entropy, resulting in zero net entropy change. As a result, the temperature of the MM increases (TISHIN; SPICHKIN, 2003).

Second-order MM have their overall entropy as a continuous function of temperature; therefore, it is possible to apply the Second Law of Thermodynamics for obtaining a relation between their isothermal entropy change and their specific heat, as indicated in Eq. 2.6 (PECHARSKY et al., 2001).In addition, an approximated relation for the adiabatic temperature is indicated in Eq. 2.7.

Figure 2.4 – Magnetocaloric effect isothermal and adiabatic expressions in a T-s diagram. Source: (TREVIZOLI, 2015)

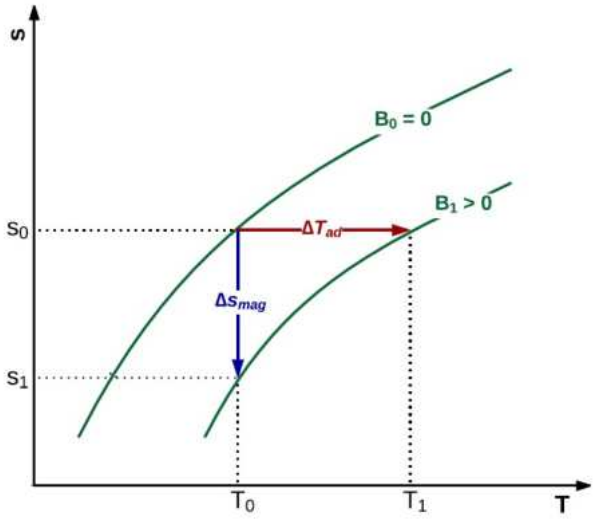

Figure 2.5 – $T - S$ diagram of the first-order magnetic phase transition, illustrating the entropy discontinuity and the T_T change for two magnetic fields, H1 and H2. Adapted from: (PECHARSKY et al., 2001)

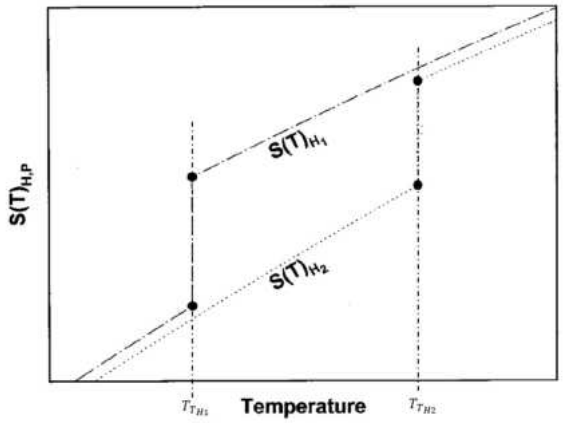

$$\Delta S_{mag}\left(T\right)_{H,P} = \int_0^T \frac{\left[C\left(T\right)_{H_h} - C\left(T\right)_{H_l}\right]_P}{T} dT \tag{2.6}$$

$$\Delta T_{ad}\left(T\right)_{\Delta H,P} \approx -\frac{T_1}{C\left(T_1\right)_{H_h,P}} \cdot \Delta S_m\left(T\right)_{\Delta H,P} \tag{2.7}$$

Furthermore, the MCE is also reversible for second-order MM, indicating that the material returns to its original state at the end of each cycle, with no entropy generated (NIELSEN et al., 2009). Due to this reversibility, the $+\Delta T_{ad} \times T$ curve along the magnetization process is different from the $-\Delta T_{ad} \times T$ curve for the demagnetization process.

Finally, the magnetic hysteresis and the discontinuity in entropy as a function of temperature, exhibited by first-order MM, result in a shift of T_T under different applied magnetic fields, as illustrated in Fig. 2.5 (PECHARSKY et al., 2001). Due to these effects, the MCE of first-order MM is intensified on the magnetic phase transition region, being the

isothermal entropy change significantly higher than that of second-order MM and named, accordingly, Giant Magnetocaloric Effect (GMCE) (PECHARSKY; GSCHNEIDNER JR., 1997).

2.3 THERMOMAGNETIC MOTORS

2.3.1 MAIN COMPONENTS

Thermomagnetic motors (TMM) consist of five main components: the magnetic field source, the MHE, the transmission system, the pumping system, and the heat sink and source (KISHORE; PRIYA, 2018a). These components are briefly explained.

The magnetic field source, is responsible for generating the magnetic field and establishing a magnetic field gradient along a designed direction. For energy harvesting applications, the field source must consist of permanent magnets. Moreover, to improve their use, the $B - H$ product of the permanent magnets should be close to the maximum value characteristic of the selected grade. This is, in regions with low $B - H$ products, soft magnetic materials can replace permanent magnets, guiding the magnetic flux lines along a magnetic circuit (MC).

The MC can contain as many magnetic volumes as desired.The greater the number of air gaps, the higher the resultant magnetic force and torque. However, increasing the magnetic volumes also implies in a larger mass of permanent magnets. Furthermore, the MC can have various geometries (BJøRK et al., 2010), which must be carefully selected and designed in conjunction with the MHE to enhance field intensity and ensure a proper gradient distribution, in order to magnetize the largest mass of MM.

The transition temperature of the MM must lie between the heat sink and heat source temperatures. For energy harvesting applications, the heat source typically consists of low-grade waste heat, while the heat sink should be at ambient temperature. Magnetocaloric material alloys can have tunable transition temperatures, depending on their stoichiometric composition. Additionally, it is important to ensure that the warm fluid stream temperature does not exceed the maximum operating temperature of the permanent magnets, especially in open TMM systems, where the fluid may be in direct contact with the magnets.

The Magnetic Heat Exchanger (MHE) is defined here as a consolidated structure in which the magnetocaloric material, shaped into a specific geometry, is assembled to maintain its form and enable heat exchange with fluid streams. It can consist of a continuous solid rod or ring of MM, or be segregated into multiple MM segments, allowing for a variety of geometries such as parallel plates or fins, discs, rings, cylindrical shells with packed beds or porous media, among others. The design of the MHE and MM geometries should aim to minimize demagnetizing losses while simultaneously maximizing the heat transfer area

and the convective heat transfer coefficient. Minimizing demagnetization directly affects the resulting magnetic force (de JESUS et al., 2024), whereas increasing the heat transfer area and convective coefficient influences the operational frequency of the thermomagnetic motor (TMM).

The transmission system primarily consists of a rotating shaft and its bearing houses. The rotating shaft is responsible for transmitting the torque and power produced by the TMM to its final application. As well, to prevent its interaction with the magnetic field the shaft must be made of a non-magnetic material.

The pumping system is responsible for driving the working fluid flow from the heat source and sink towards the MHE. It may include various components, such as pumps,solenoid valves, general-purpose valves, piping, manifolds, nozzles, and necessary instrumentation. The geometry of the MHE, combined with a well-designed pumping system is critical to achieving high-efficiency TMM. For energy harvesting applications, the pumping power is the only active energy input, since the heat source provides primarily available (waste) energy. Therefore, if the energy output of the TMM significantly exceeds the input pumping power, the system can be considered a promising solution for practical applications.

2.3.2 TYPES OF THERMOMAGNETIC MOTORS

Thermomagnetic motors can be divided into two main types: reciprocating and rotary, as presented in Fig.2.6.

The reciprocating concept was first proposed by Tesla (1889); however, in that patent, the heating and cooling of the thermomagnetic material were not performed by fluid streams. In the present context, it is considered that the warming and cooling processes are driven by forced convection, as in Fig. 2.6a.

In reciprocating devices, the magnetic force generated by the magnetic heat exchanger (MHE) is counterbalanced by an external force, which could be elastic (CORRêA et al., 2023; RIOS et al., 2024), gravitational (EVARISTO et al., 2022), or even another magnetic force source (KANEKO et al., 2021). The imbalance between these forces results in linear motion. In addition, when the MHE reaches its final equilibrium position, the fluid stream must be shifted for the thermal cycle to progress.

For example, as shown in Fig. 2.6a, at the initial position the MHE is inside the air gap (high field region) and the warm flow is introduced. As the MM loses its ferromagnetic properties, the external force source moves the MHE out of the high-field region. In the final position, cold flow is supplied to the MM, restoring its ferromagnetic properties, until the magnetic force exceeds the applied external force, thus completing the cycle. In this case, the warm and cold fluid streams can be alternated using valving systems.

Rotary devices, in contrast, produce rotating motion due to the force imbalance between

Figure 2.6 – Types of thermomagnetic motors.

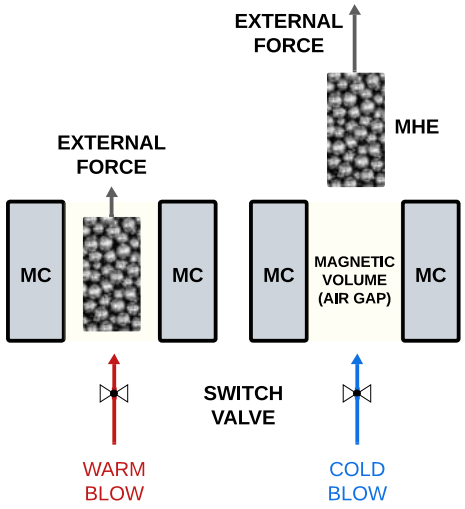

(a)

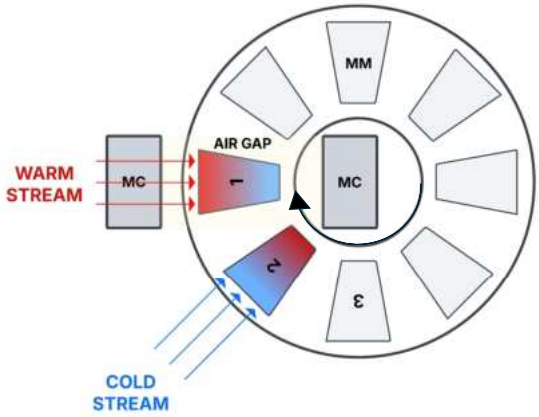

(b)

two distinct segments of MM. As illustrated in Fig. 2.6b, the MM inside the air gap (high field region) is heated by a warm fluid stream, causing it to lose its ferromagnetic properties. Meanwhile, the MM outside the air gap, which is still subjected to a residual field and field gradient, is cooled by a cold fluid stream, restoring its ferromagnetic properties. As the magnetic force acting on the segment inside the air gap becomes greater than that on the segment outside, the MM segments rotate. The externally placed segment then moves into the air gap, where it is subsequently heated. These processes are, therefore, continuously repeated.

In addition, rotary devices can be further classified into closed or open systems. The closed system is defined here as those in which the warm and cold streams each have their own tubing and valving, similar to the reciprocating concept. In this case, the fluid streams do not mix after exchanging heat with the MM. The open system is characterized by

Figure 2.7 – Diagram of the TMM operational cycle.

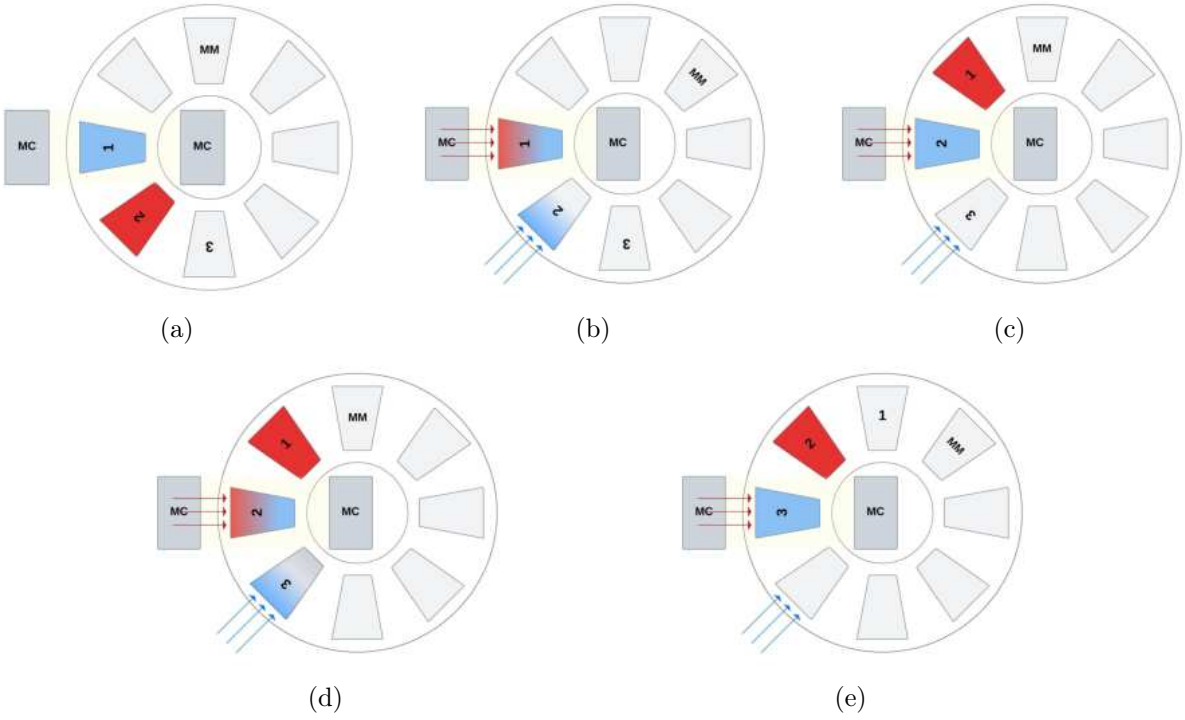

continuously supplied fluid streams that are mixed after exchanging heat with the MM.

When comparing different concepts, rotary devices stand out with several advantages. Reciprocating devices generally operate at lower frequencies and the need for alternating flow streams at the end positions often results in discontinuous motion, further limiting frequency. In contrast, well-designed rotary devices can operate continuously and at higher frequencies. Additionally, rotary motors can be directly employed in applications that require rotational motion, whereas reciprocating ones would require an additional mechanism to convert linear into rotational motion, introducing mechanical losses. Finally, for open rotary TMM, the fluid flow system can be simplified, as it does not require a complex valving system, which further reduces viscous losses. Finally, it is important to mention that in the present Master's Thesis, the designed and built prototype is an open rotary TMM.

2.3.3 THE THERMOMAGNETIC MOTOR CYCLE

Fig. 2.7 illustrates the operation of a TMM. Although the following explanation is focused on a rotary TMM, it is also applicable to reciprocating devices. As represented in Fig. 2.7a, the MM segment 1 is initially ferromagnetic. Consequently, it is attracted by the magnetic field and remains, in equilibrium, inside the air gap. Segments 2 and 3, on the other hand, are at a non-magnetic state and located outside the air gap, with minimum magnetic force. However, it is important to note that segment 2 is positioned in a region where both the applied magnetic field and the field gradient are small, but non-zero.

To start the motor's operation, segment 1 is heated by a warm fluid stream, while segment 2 is cooled by a cold fluid stream, as in Fig. 2.7b. As the temperature of segment 1 exceeds the MM T_T it transitions to a non-magnetic state. As a result, its specific magnetization approaches zero, significantly reducing the magnetic force, even inside the high field region (see Eq.2.5). Conversely, segment 2, is cooled below T_T and becomes ferromagnetic. Thus, its specific magnetization rises up, despite being located in a region with relatively low magnetic field intensity.

Segments 1 and 2 are continuously heated and cooled, respectively, until the magnetic force acting on segment 2 overcomes that on segment 1. At this point, segment 2 is attracted toward the high field region, reaching a new equilibrium position, while simultaneously pushing segment 1, as depicted in Fig. 2.7c.

Following, as in Fig. 2.7d, segment 2 now occupies the previous position of segment 1 and begins to be heated by the warm stream. Meanwhile, segment 3 moves into the position formerly held by segment 2, where it is cooled. This sequence restarts the process, which is continuously repeated as the MM segments rotate, as illustrated in Fig. 2.7e.

Throughout the heating and cooling processes, combined with the variations in the applied magnetic field, the MM undergoes a thermodynamic cycle, which can be described by either the Brayton or the Ericsson thermodynamic cycles. The main difference between these cycles is related to how the applied magnetic field is varied: the process is adiabatic for Brayton cycle and isothermal for Ericsson cycle. Thus, if magnetocaloric materials are used in the TMM, the magnetocaloric effect manifests as an adiabatic temperature change in the Brayton cycle, or as an isothermal entropy change in the Ericsson cycle (BESSA et al., 2018). Additionally, when comparing these cycles, there is a difference in the specific work output, with that of the Ericsson cycle being greater than that of the Brayton cycle. This difference tends to increase as the temperature difference between the heat source and sink decreases (de JESUS et al., 2024).

The Brayton cycle consists of four processes, described as follows. Fig. 2.8 schematically presents the $T - s$ diagram. Notice that at the initial condition, point 1, the MM is at a temperature higher than T_T and positioned outside the magnetic air gap; however, it still subjected to a residual field strength and field gradient.

- Process 1-2 (a): a cold stream cools the MM until its temperature gets lower than T_T and it becomes ferromagnetic. During this process, MM remains still outside the air gap, as segment 2 in Fig. 2.7b;
- Process 2-3 (b): the MM is attracted by the magnetic field moving along the magnetic field density gradient, until it finds a new equilibrium position inside the air gap, as segment 2 in Fig. 2.7c. Due to MCE, the MM undergoes a positive adiabatic temperature variation as a result of the field change;

Figure 2.8 – Brayton cycle $T - s$ diagram for a TMM. Adapted from (de JESUS et al., 2024)

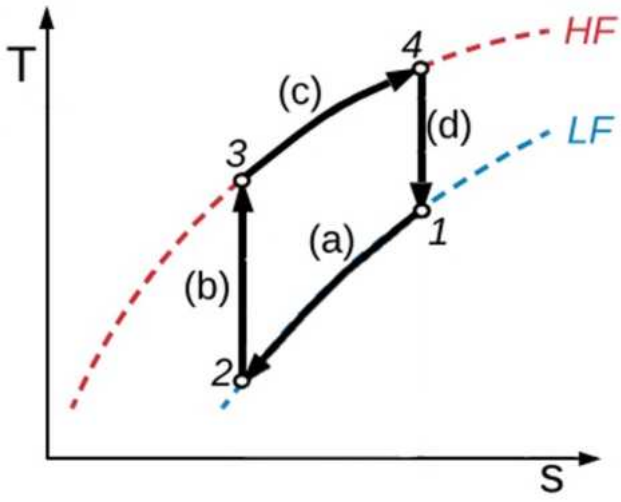

- Process 3-4 (c): a warm stream heats the MM until its temperature overcomes T_T and it returns to the non-magnetic phase. Throughout this process, the MM remains still inside the air gap, as segment 1 in Fig. 2.7b;
- Process 4-1 (d): the MM is removed from the magnetic volume presenting little resistance, as segment 1 in Fig. 2.7c. Due to MCE, the MM undergoes a negative adiabatic temperature variation as a result of the field change;

3 STATE OF THE ART

3.1 ENERGY HARVESTERS

Low-grade heat waste, with temperatures below 100°C, is widely available across a broad range of industrial processes, accounting for 66% of all discarded heat into the environment. Much of this thermal energy is transported by exhaust gases from heating systems, such as burners, furnaces, dryers and heat exchangers (HUR et al., 2023; INTERNATIONAL ENERGY AGENCY, 2021). Although its low temperature presents several challenges for recovery using conventional energy conversion cycles, it can still be converted into usable energy through the use of energy harvesting technologies, which are also notable for not producing any harmful discharges

Some alternative energy conversion cycles, such as the organic Rankine (HUNG et al., 1997) and the Kalina cycles (KALINA, 1983), can also be employed for low-grade waste recovery. The organic Rankine cycle works based on the use of organic fluids with boiling temperatures lower than that of water. Even though this system comprises a simple and reliable structure, it is still a challenge to find suitable fluids for proper operation. The Kalina cycle relies on the use of two fluids with different boiling points. However, although it can reach efficiencies close to the conventional Rankine cycle, it comprises a large and complicated plant, featuring costly components, and its patent ownership is still concentrated among a limited number of companies.

In this context, solid-state energy harvesters offer an attractive alternative for low-grade waste heat recovery. These devices are compact and operate without relying on large plants or machinery, usually requiring only a simple pumping system and no additional electricity. Therefore, they show promise for installation and operation in remote locations.

Among the main solid-state energy harvesters technologies are thermoelectric, pyroelectric, thermoelastic, thermogalvanic and thermomagnetic devices.

Studies on thermoelectric devices have increased since the discovery of the Bi_2Te_3 alloy in 1950, and they remain the only energy harvester currently in the market (HUR et al., 2023; KISHORE; PRIYA, 2018b). Thermoelectric modules operate based on the Seebeck effect, in which a temperature difference between a P-type and a N-type semiconductors, electrically connected in series, generates a electromotive force. When these semiconductors are connected to an external electric circuit, the electromotive force drives an electric current. Thermoelectric generators typically consist of multiple modules interconnected by metallic conductors, with maximum efficiency around 8% and power outputs typically below 10 W when operating as energy harvesters (ZEBARJADI et al., 2012; HAO et al., 2016).

Pyroelectric energy harvesters use naturally polarized dielectric materials that exhibit the pyroelectric effect. In this case, a change in temperature induces a variation in their spontaneous polarization. Accordingly, an increase in temperature leads to a reduction in polarization, whereas the opposite results on its enhancement. Pyromagnetic generators fundamentally consist of a dielectric material positioned between two electrodes connected to an external electric circuit. When the material's polarization changes due to temperature variation, an electric current is generated in the circuit to redistribute the charges on the electrodes and restore electrostatic equilibrium. Therefore, an alternating current can be produced by cyclically varying the material's temperature (LHERITIER et al., 2022; CHOI et al., 2023). Pyroelectric devices can operate at frequencies up to 1 Hz, limited by the heat transfer capacity of the dielectric material. They exhibit the higher produced power densities among the energy harvesters and are capable of charging wireless sensors, medical diagnostic devices, and microelectronics. However, its operation still faces the challenge of requiring a time-dependent temperature variation. Additionally, these devices can be associated to other energy conversion mechanisms, such as piezoelectric devices and wind generators (ZHANG et al., 2020).

The thermoelastic effect, present in some shape-memory alloys, causes the material to contract and transform into the austenite phase when heated above a certain transition temperature, and to expand back into the martensite phase when cooled below this temperature under external compression. Once fully transformed into the martensite phase, the material retains its deformation even after the compressive load is removed. Therefore, thermoelastic generators operate by cooling a shape memory alloy under compressive load until it fully transforms into the martensite phase, and then heating it to revert back to the austenite phase. This releases the applied load. Since the deformation during the heating stage is greater than during cooling, a net positive power output is produced. The values reported are around 1 W (AVIROVIK et al., 2014).

Thermogalvanic energy harvesters are devices that convert thermal energy into electrical energy through redox reactions driven by a temperature gradient. Thermogalvanic cells consist of an electrolyte layer positioned between two electrodes connected by an external electrical circuit. The system operates by applying a spatial temperature gradient across the electrolyte, establishing an electrochemical potential between the electrodes, which in turn drives redox reactions and generates voltage. This results in an electrical current flow through the external circuit (DUPONT et al., 2017; DUAN et al., 2018).

Finally, thermomagnetic energy harvesters can be classified into generators and motors, where the former directly convert thermal energy into electrical energy, while the latter convert it into mechanical energy. These devices operate based on the temperature dependence of the magnetic properties exhibited by soft-ferromagnetic materials, near their transition temperature. In thermomagnetic generators, the main components typi-

cally include a magnetic field source, which can be either a permanent magnet MC or an electromagnet, and a segment of MM enclosed in a coil connected to an external electric circuit. Heating the MM above its transition temperature (T_T) reduces the induced magnetic flux, while cooling it below T_T increases the magnetic flux. Therefore, alternating the material's temperature around T_T causes variations in magnetic flux intensity, inducing an alternating current in the coil and, consequently, in the external circuit (CHRISTIAANSE; BRÜCK, 2014; WASKE et al., 2019; JIANG et al., 2022; BAHL et al., 2024). Additionally, it is possible to improve these generators efficiency by cycling the applied magnetic field along with the material's temperature variation (SOLOMON, 1988). As for thermomagnetic motors (TMM), the magnetic force responsible for driving motion is directly proportional to the MM total mass, the applied magnetic field gradient, and the MM's specific magnetization. The latter depends on the MM's temperature and the resulting magnetic field. Thus, by alternately supplying and removing heat from the MM, shifting its magnetic ordering, it is possible to generate motion and mechanical power. Thermomagnetic motors usually have lower efficiencies compared to thermomagnetic generators. However, they offer greater versatility, as they can be used directly as actuators, providing either linear or rotary motion, or coupled to generators to produce electricity.

3.2 THERMOMAGNETIC MOTOR PROTOTYPES

In the context of rotary TMM prototypes, the first experimental work was published by Murakami e Nemoto (1972). The prototype is a rotor-stator assembly, in which the rotor consists of an acrylic disc with MM plates attached to its outer surface by brass pins, and the magnetic field is produced in the stator by an electromagnet. Although the employed MM is not specified, it is mentioned that its T_T is 50°C and, therefore, it is ferromagnetic at ambient temperature. The heating process is performed as the plates dip into a hot reservoir, while the cooling process is due to its exposure to the ambient temperature.In accordance with the results, the authors listed some suggestions for enhancing TMM efficiency such as: designing MC with higher magnetic field intensities, and using MM with higher magnetic flux density saturation, greater thermal conductivity and lower specific heat capacity. Neither rotational speed, torque, nor power measurements are reported.

Takahashi et al. (2006) developed a rotary TMM with three equally spaced C-shaped magnetic circuits, positioned around the exterior of a cylindrical MM shell rotor. The MM used is the $Fe_{54}Ni_{36}Cr_{10}$ alloy, with T_T around 100°C. The system achieved a maximum net power of 3.7 W at a rotational speed of 24 RPM, and a maximum torque of 1.8 N·m at 18 RPM, when operating with the thermal reservoirs at 95°C (warm) and 11°C (cold), and a volumetric flow rate of 1 L/s (equivalent to 20 LPM per nozzle). The authors also characterized losses due to hydrodynamics and electromagnetic breaking, and discussed how to mitigate these losses.

Mehmood et al. (2021) proposed a TMM that consists of two diametrically opposed C-shaped magnetic circuits, and a rotor comprising a non-magnetic disc with sixteen Gd blocks attached to its outer surface. The magnetic field produced by the MC has a maximum intensity of 0.4 T. The motor developed a maximum rotational speed of 242 RPM and a maximum torque of 0.05 N·m, with the thermal reservoirs at 327 K (warm) and 294 K (cold). Based on their results, the authors concluded that for enhancing the motor performance, it is necessary to increase the number of magnetic volumes and to select a MM geometry that enhances heat transfer.In a subsequent work, Kim et al. (2022) adapted this TMM using a single C-shaped MC and integrating five rotors mounted on a shared shaft. The assembly was connected in series with an electromagnetic generator and a triboelectric nanogenerator, enabling simultaneous energy harvesting. A 3:1 bevel gear mechanism was employed to increase the rotational speed to 270 RPM, resulting in a maximum output power of 1.1 W.

In regards to linear prototypes, Kaneko et al. (2021) designed and tested a purely magnetic TMM. The prototype consists of a double-C-shaped magnetic circuit, generating two magnetic regions with a peak magnetic field intensity of 0.89 T. Two magnetic heat exchangers, each filled with gadolinium spheres, are positioned within these regions, one in each magnetic volume. The motor works based on the imbalance between the magnetic forces acting on the heat exchangers. The authors reported a maximum frequency of 0.5 Hz and a peak produced power of 0.4 W.

Rios et al. (2024) proposed a linear TMM that utilizes a spring restoring mechanism. Thus, this motor operates through the interaction between magnetic and elastic forces. The designed prototype comprises a nested Halbach cylinder, which produces a maximum field strength of 1.35 T. The magnetic heat exchanger (MHE) is filled with gadolinium spheres, in a packed bed with a total mass of 54.5 g. Those authors reported a peak power output of 4.2 W at an operational frequency of 1.25 Hz.

Finally, some works have proposed simulation-based approaches for designing TMM, followed by prototype construction to validate their methodologies. Franzitta et al. (2013) modeled and built a rotor-stator TMM. The rotor consists of an array of tubes filled with gadolinium powder, and the stator of a single-pole DC machine stator, which produces a 0.9 T magnetic field. The authors found a good agreement by comparing the simulation results with the experimental data and reported a maximum rotational speed of 78.3 RPM and a 1.3 N·m stand-still torque.

Kishore et al. (2020) proposed a proof-of-concept prototype consisting of two gadolinium stripes attached to opposites sides of a shaft connected to a Peltier cooler. Two sets of permanent magnets, each comprising a flexible heater sandwiched between two permanent magnet blocks, produces two magnetic volumes. The device operates based on thermomagnetic mass oscillation, driven by the interaction of opposing magnetic forces.

Table 3.1 – TMM motor prototypes main maximum measured performance results

Author	Type	Speed	Torque	Produced Power
Takahashi et al. (2006)	Rotary	N.A	N.A	3.7 W
Franzitta et al. (2013)	Rotary	78.3 RPM	1.3 N·m	N.A
Kishore et al. (2020)	Linear	0.33 Hz	N.A	0.2 W/kg
Mehmood et al. (2021)	Rotary	242 RPM	0.05 N·m	1.05 W
Kaneko et al. (2021)	Rotary	0.5 Hz	N.A	0.4 W
Rios et al. (2024)	Linear	1.25 Hz	N.A.	4.2 W

The prototype exhibited an oscillation frequency of 0.33 Hz, and a power density of 0.2 W/kg of gadolinium was estimated from the force-displacement curve.

Table 3.1 summarizes the main performance results from each prototype. The acronym N.A. stands for *non-applicable*). From these results, it is evident that the current state-of-the-art prototypes are not able to attain high torques and rotational speeds. Moreover, many of these systems fail to sustain continuous motion, operating instead in intermittent cycles and at low frequencies. These limitations can be attributed to improper magnetic field source design associated with inadequate fluid flow and heat transfer properties, which are critical to enhance TMM performance metrics.

3.3 THERMOMAGNETIC MOTOR PATENTS

Since the late 19th century, more than forty patents on thermomagnetic motors have been filed from all over the world. The first patent was proposed by Nikola Tesla, in 1889 (TESLA, 1889). It describes a linear TMM, consisting of an MM segment, a permanent magnet or an electromagnet for generating the magnetic field, a heat source and a restoring force mechanism, such as the gravitational force or the elastic force of a spring, acting on the opposite direction to the magnetic force. The MM employed by Tesla is ferromagnetic at ambient temperature, being attracted to the high magnetic field region, which coincides with the heat source position. The MM is then heated up to its non-magnetic condition and is moved back to its initial position by the restoring force.

The first patent of a rotary TMM dates back to 1922 and it was filed by Schwartz (1922). The motor consists of a non-magnetic ring-shaped rotor filled with several MM segments that are ferromagnetic at ambient temperature. The magnetic field is generated by pairs of electromagnets, in which one is placed inside the ring and the other outside. Also, a hot blow is forced through the high magnetic field region between the electromagnets to drive the MM segments to their non-magnetic state.

Besides the two patents described above, only thirteen others were published in the 19th and 20th centuries. On the 21st century, the studies on TMM have been encouraged by the development of new technologies, such as high-BH energy permanent magnets (SAGAWA et al., 1984), magnetocaloric materials with first-order phase transition around

room temperature (GSCHNEIDNER; PECHARSKY, 2000) and magnetic circuits with high magnetic field intensity (HALBACH, 1980; BJøRK et al., 2010). As a result, twenty-nine new patents were filed.

These patents can be categorized according to the TMM designs: reciprocating, which has received less attention with only six patents, or rotary. In regards to rotary devices, fifteen have a disc-shaped rotor, with a few different concepts. Some have rotors consisting of discs entirely made of MM, while others describe a rotor made of a non-magnetic disc with round MM tablets on its upper surface. There are also designs with rotors that have MM segments assembled to the external surface of a non-magnetic disc through rods, as well as proposals with a MM layer attached to the external surface. Finally, some rotors are quite similar to the one in this work, consisting of several thin MM plates radially coupled to the upper surface of a non-magnetic disc. However, these inventions differ when comparing the MC designs and the heat transfer mechanisms.

The remaining rotary TMM patents feature MM rotors shaped as cylinders or rings. Furthermore, some patents claim TMM designs with a rotor-stator structure, while others describe rotary TMM coupled to electric generators. Another concept presents TMM consisting of MM segments attached to a transmission belt. Finally, the concept of scaling TMM by coupling more than one set of MC and MM rotor to the same rotating shaft is introduced.

Apart from the rotor and transmission system, the different concepts also differ in relation to the heat transfer mechanism and the magnetic field source. Among the reported heat transfer mechanisms are: (i) MM cooling by exposure to ambient temperature, (ii) MM heating or cooling by immersion in a tank with conditioned fluid, and (iii) forced fluid flow through the MM.

Regarding the magnetic field source, some inventions employ a single electromagnet or permanent magnet, while others use pairs or sets of permanent magnets. Finally, some patents describe magnetic circuits with geometries such as horseshoe, rectangular, cylindrical Halbach arrangement, and linear Halbach arrangement. Some of the filed patents did not describe either the heat transfer mechanism or the magnetic field generation structure employed. Table 3.2 summarizes these characteristics and associates them with the respective patents detailed within.

The prototype proposed in this work features a disc-shaped rotor with several thin MM plates mounted on its lower surface, combined with a permanent magnet MC arranged in a double-L Halbach configuration. This design creates four magnetic volumes with high magnetic field intensity. Regarding the heat transfer mechanism, the developed TMM employs forced warm and cold fluid streams directed into specific regions of the rotor. These combined features result in a prototype that is distinct from all those presented in Tab. 3.2.

Table 3.2 – Categorization of TMM Patents by Design, Heat Transfer Mechanism, and Magnetic Field Source

TMM Type	Rotor / System Design	Examples / Patents	Heat Transfer Mechanism	Magnetic Field Source
Reciprocating	–	Tesla (1889); Grigorij (1996); Robinson (2011); Coelho (2019); Fernandezi (2019); Kaneko (2019)	–	–
Rotary	Discs entirely made of MM	Katayama (1984); Vollers (1988); Jørgensen (1994); Hongbin (2001); Li (2008); Kuo (2015)	MM cooling by ambient exposure: Tesla (1889); Schwartz (1922); Norton (1928); Kemenczky (1976); Yoshida (1978); Jørgensen (1994); Grigorij (1996); Hongbin (2001); Guohua (2004); Hazelwood (2012); Tanaka (2013)	Single electromagnet: Kaliský (2006); Gee (2019). Permanent magnet: Tesla (1889); Norton (1928); Kemenczky (1976); Jørgensen (1994); Hongbin (2001); Kaliský (2006); Murata (2009a). Sets of permanent magnets: Vladislav (1993); Grigorij (1995), Grigorij (1996); Guohua (2004); Cernomazu (2008); Murata (2009b); Robinson (2011); Morimoto (2013); Tanaka (2013), Tanaka (2014a), Tanaka (2014b); Fernandezi (2019). Magnetic circuits: horseshoe (Pirc (1973); Yoshida (1978); Katayama (1984); Vollers (1988); Fuerthaller (1993); Stepanovich (2001); Masahiro (2002); Hazelwood (2012)) rectangular (Nishikawa (1997); Tanaka (2014b)), cylindrical Halbach (Coelho (2019)), linear Halbach (Kaneko (2019))
	Rotor of non-magnetic disc with MM tablets	Cernomazu (2008)	Immersion in conditioned fluid: Vollers (1988); Grigorij (1996); Nishikawa (1997); Tanaka (2013), Tanaka (2014a), Tanaka (2014b)	–
	MM segments on external surface	Vladislav (1993); Hazelwood (2012)	Forced fluid flow through MM: Schwartz (1922); Merkl (1969); Pirc (1973); Yoshida (1978); Hongbin (2001); Guohua (2004); Robinson (2011); Morimoto (2013); Tanaka (2014b); Gee (2019); Coelho (2012), Coelho (2019); Kaneko (2019)	–

TMM Type	Rotor / System Design	Examples / Patents	Heat Transfer Mechanism	Magnetic Field Source
	MM layer on external surface	Fuerthaller (1993); Guohua (2004)	–	–
	Thin MM plates radially coupled	Yoshida (1978); Grigorij (1995)	–	–
	Cylindrical or ring-shaped rotors	Norton (1928); Voznesenskij (1947); Kemenczky (1976); Nishikawa (1997); Masahiro (2009); Murata (2009b)	–	–
	Rotor-stator structure	Merkl (1969); Pirc (1973); Coelho (2012)	–	–
	Rotary coupled to electric generators	Morimoto (2013); Gee (2019)	–	–
	MM segments on transmission belt	Murata (2009a); Tanaka (2013)	–	–
	Scaling by coupling multiple MC and MM rotors	Tanaka (2014a), Tanaka (2014b)	–	–

4 MATERIALS AND METHODS

This chapter presents the experimental setup of the rotary thermomagnetic motor, detailing its design, construction, and performance characterization. The primary requirements for the experimental apparatus are as follows:

(i) Easy adjustment of the experimental operating parameters, such as the hot and cold reservoir temperatures, as well as the warm and cold volumetric flow rates, in order to achieve a wide range of experimental conditions.

(ii) Detailed measurement of operating parameters, such as the inlet temperatures, flow rates, and pressures of the warm and cold fluid streams; and output metrics, including torque and rotational speed, to ensure a comprehensive and reliable evaluation of the motor's performance.

(iii) A compact and robust overall structure, designed to maximize torque and power output while minimizing the use of permanent magnets and magnetic materials.

4.1 KEY DESIGN ELEMENTS IN TMM DEVELOPMENT

The key performance parameters of a TMM are the generated force or torque, and operational frequency, both of which directly influence the produced power. Thus, maximizing their values are desirable. In turn, achieving high torque and frequency has some contrasting relationships, which require critical consideration during the design process.

As described in Eq. 2.5, the magnetic force is strongly influenced by the MC parameters, including the generated magnetic field intensity, the magnitude and distribution of the magnetic flux density gradient, and the volume of the air gap. The latter directly affects the H_{apl} intensity.

First, a high magnetic field gradient is crucial for maximizing F_{mag}. Additionally, ∇B must be designed to favor the rotor motion, with the ideal scenario being a continuous gradient along the designed direction (SILVA; TREVIZOLI, 2023). Second, a strong H_{apl} is necessary for increasing F_{mag}, as it results in a higher $\sigma(T, H_{res})$. This can be achieved through the use of high BH energy permanent magnets, careful selection of soft ferromagnetic materials, and precise design of the MC geometry.

The MC design must also account for the geometric features of the magnetic heat exchanger (MHE), where the MM is placed to exchange heat with the fluid streams. The MHE should be able to move freely within the air gap, without obstruction or friction. However, increasing the air gap can significantly decrease the H_{apl}, creating a trade-off be-

tween the air gap height and field strength that must be carefully balanced. Furthermore, the MHE's geometry must be designed to minimize demagnetization losses by reducing the demagnetization factor N_D, ensuring that H_{res} remains close to H_{apl}, as expressed in Eqs. 2.4 and 2.3.

Both the TMM operational frequency and continuous motion depend directly on the effectiveness of the heat transfer between the MM segments and the warm and cold fluid streams. Therefore, the MM geometry should be designed to maximize the surface area and enhance the convective heat transfer coefficient. However, some constraints leads to a necessary compromise in the design. First, the MHE dimensions must remain compatible with the air gap volume, restricting the increase in the heat transfer area. Second, the increase in flow velocities to improve the heat transfer coefficient could result in larger viscous losses and pumping requirements.

Lastly, there is also a trade-off associated with the MM mass. Although increasing the MM mass increases F_{mag}, it simultaneously raises its thermal mass, leading to longer heating and cooling periods necessary to guarantee the magnetic phase shifting around T_T. Therefore, the operational frequency is reduced.

The prototype presented in this Master's Thesis was designed based on this preliminary analysis. Even so, it should be noted that, due to limitations in material availability, the designed geometry and mass were not optimized.

4.2 EXPERIMENTAL APPARATUS DESCRIPTION

The thermomagnetic motor (TMM) experimental apparatus is a laboratory-scale setup (TRL4[1]), mainly composed of a MC, which generates the magnetic field volume, a magnetocaloric material (MM) rotor, and a transmission system that delivers the produced torque and power to a given application.

The magnetic circuit (MC) is stationary and generates its magnetic field using high-BH energy permanent magnets. Its design, which will be detailed in Section 4.3, was developed to achieve an intense magnetic field and magnetic flux density gradient, both distributed to promote rotor motion. The proposed MM rotor consists of a non-magnetic material disc with radially arranged MM fins attached to its lower surface. Channels for the working fluid flow are formed between adjacent fins. Furthermore, the designed rotating shaft is bipartite and includes features such as rebounds and recesses to maintain concentric alignment with the assembled rotor, ensuring the torque and power transmission. Both designs, along with their production and assembly process, will be detailed in section 4.5. All of those main components, depicted in Fig. 4.1, are mounted on a versatile rack made of extruded aluminum profiles, which enables the adjustment of their positions.

[1] TRL4 corresponds to the fourth level of NASA's Technology Readiness Level (TRL) scale, which ranges from level 1 to 9, and indicates validation of the apparatus in a laboratory environment

Figure 4.1 – Rotary TMM prototype main components.

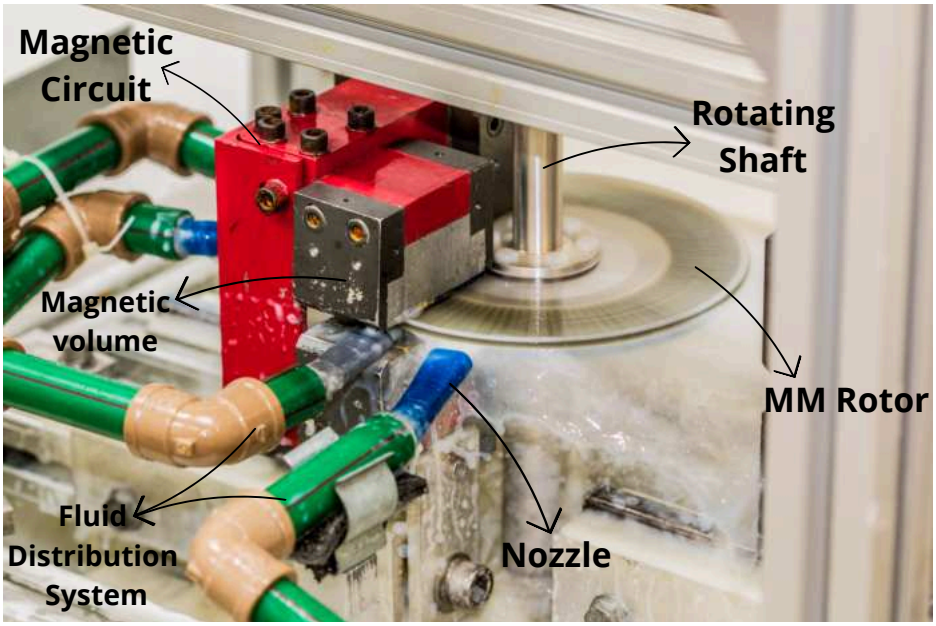

To enable the motor's operation and performance evaluation, the experimental apparatus includes a system for measuring the motor's angular speed and generated torque. Lastly, to supply the warm and cold fluid flow streams, there is a fluid treatment station that conditions and directs the fluid streams to specific regions of the rotor. This station is equipped with all the necessary instrumentation to monitor key operating parameters, including the temperature, pressure, and volumetric flow rate of the fluid streams.

4.3 MAGNETIC CIRCUIT

Some design requirements were considered in the development of the MC:

(i) To generate a 1.0 T magnetic field uniformly distributed within the magnetic volume, along with a field gradient directed from the magnetic volume center toward the front and back faces of the main permanent magnets.

(ii) Use of commercially available permanent magnet blocks.

(iii) Easy assembly of the rotor and shaft, along with convenient access for maintenance of the fins.

(iv) Ease in-house production using only conventional machining operations.

The MC design procedure was initiated by the investigation of several geometries that satisfied the requirements (i) and (iii). The selected configuration features a double-L shaped geometry, composed of 120.0 mm and 80.0 mm segments, where each L-shaped assembly is independent and generates two magnetic field volumes. This geometry enables

Figure 4.2 – The designed magnetic circuit.

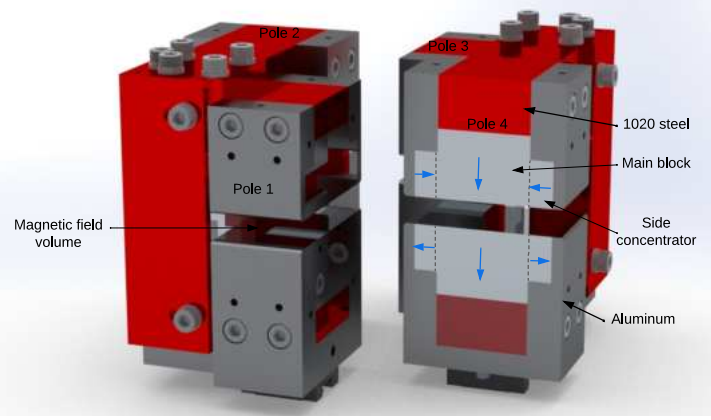

the TMM to operate in either a two or four magnetic field volumes configuration. Accordingly, the four magnetic field volumes configuration maximizes both produced torque and power, thereby meeting requirement (i). The asymmetry of the L-shaped structure enables the gadolinium fins to enter all four magnetic volumes parallel to their respective main permanent magnet block, producing equal magnetic forces on each volume and, therefore, achieving the desired continuous rotary motion.

High BH energy and commercially available NdFeB permanent magnets, disposed in a Halbach arrangement along with soft ferromagnetic material parts, were employed to ensure the expected magnetic field intensity. The main permanent magnet blocks are responsible for generating the magnetic field. Smaller magnets, also known as side concentrators, have their remanence flux perpendicular to the main magnets, and are used to minimize the magnetic flux lines leakage and promote a more uniform magnetic flux density distribution. The soft ferromagnetic material parts are used to guide the magnetic flux lines along the MC, strengthening the generated magnetic field. Finally, a 12.0 mm air gap was designed, exceeding the rotor's total thickness to allow unrestricted motion without significantly compromising the magnetic field intensity. This design also ensures that all the MC parts can be produced in-house using only conventional machining operations.

To facilitate the rotor and shaft structure assembly, two guideway slider blocks were placed under both L-shaped sets and coupled to linear guide rails. This system allows the two sets to slide apart from each other, leaving enough room for handling. When the assembly is completed, screws hold the sets at their positions.

Figure 4.2 illustrates the designed MC. The parts in red are the soft magnetic material, used to guide the magnetic flux lines along the MC. The ones in dark grey are aluminum parts, which only have structural functions. The silver regions are the NdFeB magnet blocks, and the arrows indicate their remanence flux densities orientations.

In addition to the geometric configuration investigation, numerical simulations were also performed to select: (i) the permanent magnets grades; (ii) the soft ferromagnetic material

used; (iii) the soft ferromagnetic segments thicknesses. The latter requires an in-depth investigation because ferromagnetic materials exhibit a strong dependence of their relative magnetic permeability on the magnetic flux density. As the flux density increases, the relative permeability decreases, approaching 1 (the relative permeability of air). When this occurs, the ferromagnetic material no longer effectively guides the magnetic flux lines, leading to a reduction in the generated field strength. Since the magnetic flux density is influenced by the cross-sectional area, there is a minimum thickness required to maintain the high relative permeability of the ferromagnetic material without significantly increasing the overall volume and mass of the magnetic circuit. In this context, several steel options were considered, including ABNT 1008, 1010, 1018, 1020, and 1030.

The properties and dimensions of the selected permanent magnets, are presented in Tab. 4.1 (BAKKER MAGNETS, 2024). Regarding the soft ferromagnetic material, simulations showed minimal variation in the generated magnetic field among the evaluated steel options. Therefore, due to local availability, the ABNT 1020 steel was selected for the L-shaped assemblies. Additionally, a thickness of 23.0 mm was selected for the steel parts, without compromising the generated field strength and the total mass/volume of the MC.

After the final assembly of the MC some deviations from the designed dimensions were observed; however, none exceeded the established tolerances, including the 1.5 mm tolerance for the air gap. The smallest measured gap was approximately 10.5 mm, which did not compromise the rotor's motion. Photographs of the assembled magnetic circuit are presented in Figure 4.3.

Table 4.1 – NdFeB permanent magnets dimensions and properties.

Type	Dimensions (mm)	Grade	Remanence (T)
Main	40 x 40 x 30	N42	1,29 ∼1,33
Concentrator	40 x 20 x 10	N42	1,29 ∼1,33

Figure 4.3 – Magnetic circuit built according to the dimensions obtained from the proposed design procedure: (a) complete magnetic circuit; (b) L-shaped assembly.

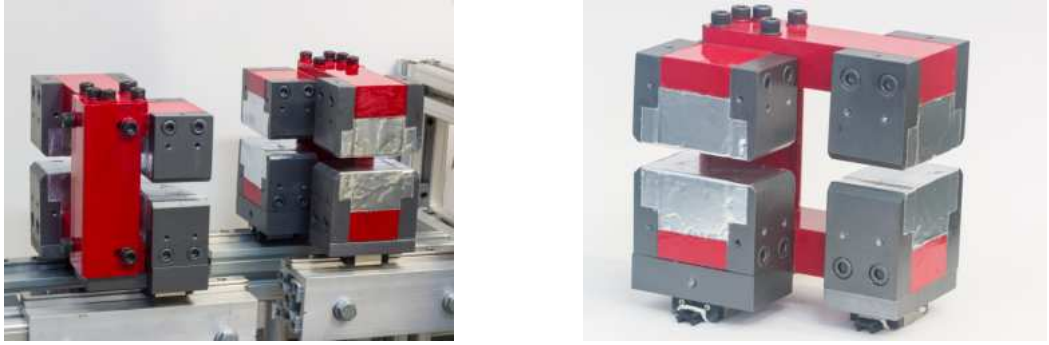

(a) (b)

4.3.1 NUMERICAL SIMULATIONS

The magnetic circuit simulations were conducted using COMSOL Multiphysics, AC/DC module, and Magnetic Fields No Currents formulation (v.6.2, licence Number 2106003). Due to the geometry of the designed MC and its coupling with the MM fins, as shown in Fig. 4.4, only three-dimensional simulations provided physically consistent results. Since the electric currents are negligible, the magnetic scalar potential, V_m, (Eq. 4.1) and the constitutive relation for permanent magnets (Eq. 4.2) can be combined and substituted into Gauss law for magnetism, leading to the magnetostatic formulation used (Eq. 4.3) (COMSOL Multiphysics ®, 2024):

$$\vec{H} = -\nabla V_m \tag{4.1}$$

$$\vec{B} = \mu_0 \mu_r \vec{H} + \vec{B}_r \tag{4.2}$$

$$-\nabla \cdot \left(\mu_0 \mu_r \nabla V_m - \vec{B}_r \right) = 0 \tag{4.3}$$

The simulations computed the magnetic flux density and its gradient. The simulated geometry also included the gadolinium fins volumes filled with air, as depicted in Figure 4.4, which permitted the evaluation of an average field in the plate volume. The input parameters were the permanent magnets remanent flux densities (see Table 4.1) and their orientations, the relative permeability, set tas 1.05 (BJøRK et al., 2010), and the soft magnetic materials relative permeabilities, considering its dependence on the magnetic flux density. The boundary conditions were set using a block of 300.0 mm x 300.0 mm filled with air surrounding the MC volume.

The simulations were performed using a mesh of about 250887 tetrahedral elements, with an average element quality of 0.8296. The convergence tolerance of 3.7×10^{-4}. It is also important to note that the design was verified for self-demagnetization and no issues were observed.

The magnetic flux density distribution and its gradient were evaluated along a series of concentric circles plotted on a cross-sectional plane at the center of the air gap (plane $x - y$ at $z = 0$). The first circle has a radius of 30.0 mm, and the subsequent circles are spaced in 5.0 mm intervals, up to the final radius of 90.0 mm. This is, starting from the edge of the inner concentrator to the edge of the outer concentrator, as illustrated by the blue circles in Fig. 4.5. These results are further used to validate the magnetic circuit design through comparisons with experimental measurements of the same variables.

Figure 4.4 – MC with gadolinium fins volumes for the magnetic flux density evaluation.

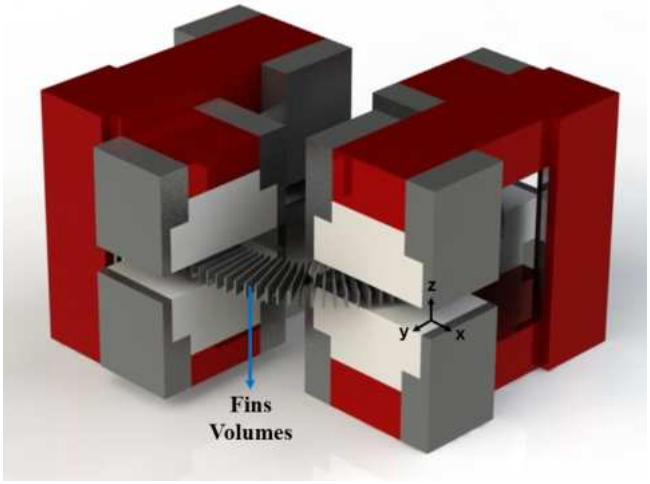

In addition, the plate volume-average magnetic flux density distribution and its gradient were also evaluated. Beyond the MC design, these results served as a reference for defining the heating and cooling regions of the MM rotor, which will be explained in Sec. 4.8.

Figure 4.5 – Schematic illustration of the magnetic flux density measurement domains: the orange dots represent the experimental measurement points, the blue circles indicate the radial locations where the magnetic flux density was numerically evaluated, and the dashed circle indicates the radial location where the peak magnetic flux density is observed.

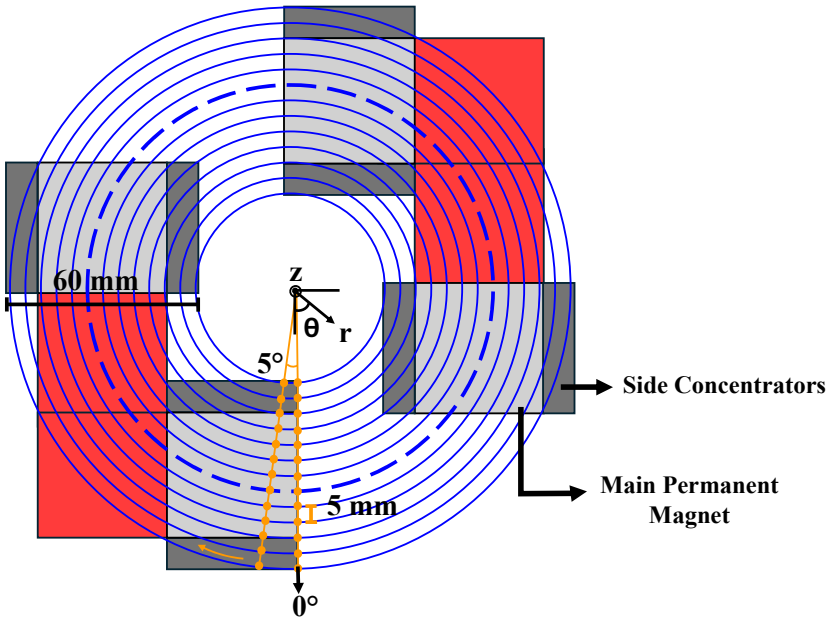

4.3.2 PRODUCTION AND ASSEMBLY

The magnetic circuit was produced and assembled in-house at the *Laboratório de Usinagem e Automação* and the *Laboratório de Sistemas Térmicos Emergentes (StreamLab)*, both part of the *Universidade Federal de Minas Gerais*.

The quality of the magnetic circuit production, particularly the adherence to the designed dimensional tolerances, is closely tied to the precision of the final assembly and, consequently, to the accurate reproduction of the intended magnetic field. The production and assembly processes are described in Appendix A.

4.3.3 EXPERIMENTAL CHARACTERIZATION

The experimental apparatus in Fig. 4.6 was assembled to characterize the magnetic flux density (B) distribution along the MC angular and radial directions and, therefore, validate the design procedure. A Gaussmeter (GlobalMag, model LMP – HALL - 20k) and a T1 Hall probe were used for the magnetic flux density measurements.

The apparatus features a rotating shaft, connected to an incremental encoder (IFM, model RVP510), and a mechanism coupled to the Hall probe to enable its displacement in the radial direction. This mechanism, as detailed in Figs. 4.6c and 4.6d, consists of an aluminum tube with twelve openings, in steps of 5.0 mm, for fitting a peg that holds the probe still. The shaft was placed at the center with the Hall probe at the center of the air gap.

The measurement procedure involved sweeping the magnetic volume in intervals of 5.0 mm along the radial direction, covering a length of 60.0 mm, and in 5.0° intervals in the angular direction. Fig. 4.5 illustrates the measurement domains, with the orange dots representing the measurement points at two angular positions, and the dashed circle indicating the radial location where the peak magnetic flux density is observed. This procedure was repeated twice: first to measure the z-component (B_z) and then to measure the θ-B_θ, hence, B is calculated by Eq. 4.4:

$$B = \sqrt{B_z^2 + B_\theta^2} \tag{4.4}$$

The uncertainties related to the magnetic flux density measurements were calculated by Eq. 4.5, in accordance with Holman (1993), in which u_{B_z} and u_{B_θ} are the combination of type A and type B uncertainties of the measurements, as described in Eq. 4.6.

$$u_B = \sqrt{\left(\frac{\partial B}{\partial B_z}\right) \cdot u_{B_z}^2 + \left(\frac{\partial B}{\partial B_{xy}}\right) \cdot u_{B_{xy}}^2 + 2 \cdot \frac{\partial B}{\partial B_z} \cdot \frac{\partial B}{\partial B_{xy}} \cdot u_{B_z} \cdot u_{B_{xy}}} \tag{4.5}$$

$$u_{B_i} = \sqrt{u_{B_{i,A}}^2 + u_{B_{i,B}}^2} \tag{4.6}$$

The type A uncertainty is calculated by Eq. 4.7, where S is the sample standard deviation and n is the sample size.

$$u_{B_{i,A}} = \frac{S}{\sqrt{n}} \tag{4.7}$$

Five sample measurements were used. The type B uncertainty is provided by the gaussmeter calibration certificate: 2% of the measured value and 2% full scale (2.0 T). Assuming a normal distribution, with a 95% confidence level and infinite degrees of freedom, the expanded uncertainty is calculated by Eq. 4.8.

$$U_B = 2 \cdot u_B \tag{4.8}$$

Figure 4.6 – Experimental apparatus for the magnetic circuit characterization: (a) complete apparatus; (b) mechanism developed to enable the probe displacement in the radial direction; (c) Measurement of the B_z component; (d) Measurement of the B_{xy} component.

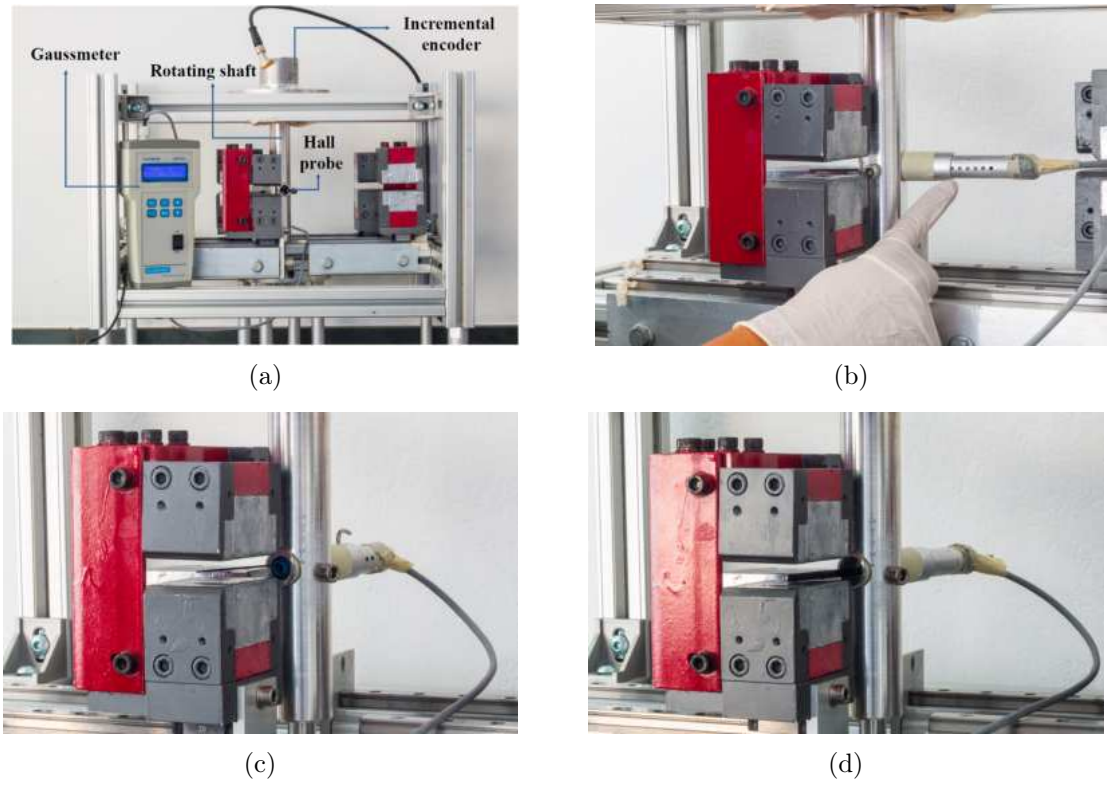

(a) (b)

(c) (d)

4.4 WORKING MATERIALS

The rotor fins are made of Gadolinium (Gd), which is a magnetocaloric material with a second-order magnetic phase transition around 293K (DAN'KOV et al., 1998). Although its T_T is not the most suitable for waste heat recover applications, as it requires cooling the cold fluid below ambient temperature, gadolinium was selected due to: (i) its current availability in the laboratory in different shapes such as plates and spheres; (ii) its magnetic and thermophysical properties are well known, which facilitates the analysis of the experimental data and; (iii) because it is a benchmark material for TMM applications near room temperature (KISHORE; PRIYA, 2018a; HUR et al., 2023).

Figure 4.7 – Gd fins dimensions.

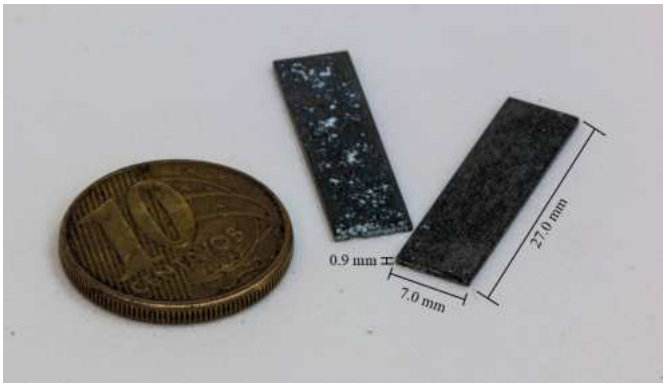

The Gd used was purchased from the company Huhhot Rongxin New Metal Smelting Co., (CHN), which reported a minimum purity of 99.9%. The fins have a thin plate shape, with the dimensions of 27.0 mm x 7.0 mm x 0.9 mm, as depicted in Fig. 4.7. Each fin weighs on average 1.22 g. Thus, since the rotor final structure features 100 plates, the total mass of MM is approximately 0.122 kg.

The working fluid is a mixture of distilled water with 10%vol of monoethylene glycol, and 5%vol of ME1. The monoethylene glycol functions as an antifreeze, while the ME1 serves as an anticorrosion fluid, as recommended by Döring et al. (2024).

4.5 ROTOR AND TRANSMISSION SYSTEM

4.5.1 ROTOR DESIGN

The rotor of the TMM prototype was designed follwing some requirements as listed below:

(i) The rotor structure must be composed of a non-magnetic material that offers sufficient strength and machinability;

(ii) The rotor structure has to accommodate 100 Gd fins, creating a converging channel between them. These channels must remain unobstructed to ensure proper fluid flow;

(iii) The heat transfer area must be maximized. Since the fins are bonded to the rotor structure, it is important to minimize the area allocated for the adhesive;

(iv) The final thickness of the rotor, including the fins, must be smaller than the air gap height. Thus, it is important to account for dimensional tolerances associated with the manufacturing process.

(v) During the prototype operation, the working fluid in contact with the fins must have an unobstructed path to exit the rotor region, flowing downward into the collecting container;

Figure 4.8 – Finned rotor design: (a) cross-section view; (b) perspective view.

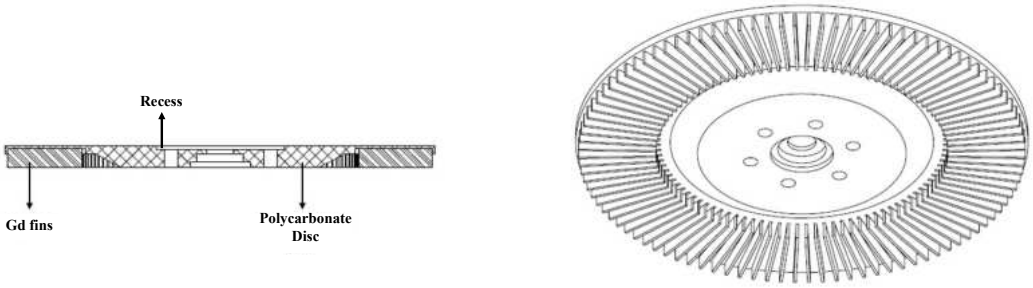

(a) (b)

(vi) Easy assembling and positioning, ensuring proper alignment of the shaft with the rotor surfaces, thereby, maintaining their concentricity.

The designed rotor consists of a polycarbonate disc with 158.0 mm diameter and 3.0 mm thickness. A total of 100 Gd fins are radially arranged on its lower surface, forming channels between them through which the working fluid flows and exchanges heat with the MM. The Gd fins are positioned 1.0 mm inward from the disc's outer edge. This ensures that the entire lengths of the fins remain inside the air gap, maximizing the active MM mass.

The fluid flow channels have a convergent nozzle shape, with an entrance distance of 4.0 mm and an exit distance of 2.3 mm. The bounding grooves, with 1.0 mm depth, were made on the lower surface of the disc. The designed depth ensured that the fins remain fixed, leaving 6.0 mm of the fins' height exposed to the working fluid. Therefore, considering the disc thickness and the exposed fin height, the rotor has a final thickness of 9.0 mm, allowing for unrestricted rotation even at the smallest air gap (10.5 mm).

Furthermore, the disc has a conical projection at its center to facilitate the downward flow of the fluid into the collection container. There are also recesses on the disc surfaces for the rotating shaft coupling, ensuring their concentricity. The designed rotor geometry is illustrated in Fig. 4.8.

4.5.2 TRANSMISSION SYSTEM DESIGN

The prototype transmission system features a rotating shaft and its respective upper and lower bearing housings. The shaft is responsible for transmitting the torque and mechanical power to a given application. The bearing houses are responsible for supporting the shaft with minimal friction losses and connecting it to the motor rack.

The rotating shaft is cylindrical, bipartite, and made of aluminum. The upper shaft has

Figure 4.9 – Coss-section view of the transmission system designed

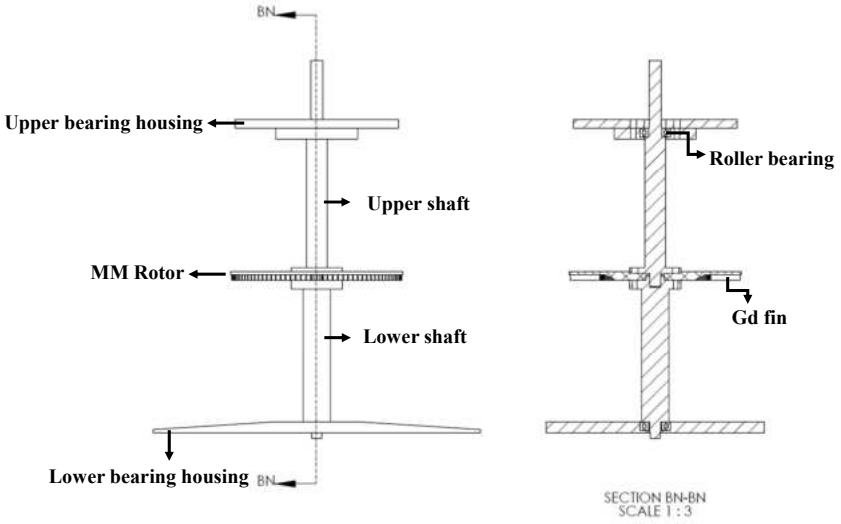

a 19.0 mm diameter, while the lower shaft has a diameter of 25.0 mm. At one end, each shaft has a diameter of 11.0 mm for its installation into the bearings. At their second end, both shafts feature a flange, which is screwed to the rotor. Still at the flanged ends, the upper and lower shafts have a protrusion and a corresponding recess, respectively. When installed, they ensure the proper alignment and concentricity.

The upper bearing housing is disc-shaped with 150.0 mm diameter. The lower bearing housing consists of a 200.0 mm x 300.0 mm plate with sloped sides, designed to facilitate fluid flow into the collection container Both bearing housings are made of aluminum. Their respective roller bearings were pressed-in-place at the center. The bearing housings are directly screwed to the motor rack, allowing for alignment adjustments to achieve the system's concentricity. Fig. 4.9 depicts the designed transmission system.

4.5.3 PRODUCTION AND ASSEMBLY

The rotor structure and the transmission system components were produced in-house, from raw materials employing mainly turning, CNC milling, and drilling operations. Particularly, the bonding grooves of the rotor were produced by micro-milling using a 0.8 mm milling cutter. The produced polycarbonate disc can be seen in Fig. 4.10. The cutting tools and parameters adopted, and the use of proper cutting fluids assured the attainment of the dimensional tolerances specified to each part.

For the final assembly of the rotor, the fins were bonded to the grooves using an epoxy adhesive (3M Scotch Weld DP 460 MS). Before the bonding process, the fins were partially covered with adhesive tape for protection, leaving exposed only the region intended to be inserted into the groove, as illustrated in Fig. 4.10b. To ease the handling and assure their right alignment, the fins were gradually bonded, respecting the adhesive full cure period between stages, as detailed in Fig. 4.11. After the bonding process, the rotor reached its designed total thickness of 9.0 mm, ensuring its fitting in the shortest air gap and the

Figure 4.10 – Produced polycarbonate rotor structure and details of the bonding grooves with one attached Gd fin.

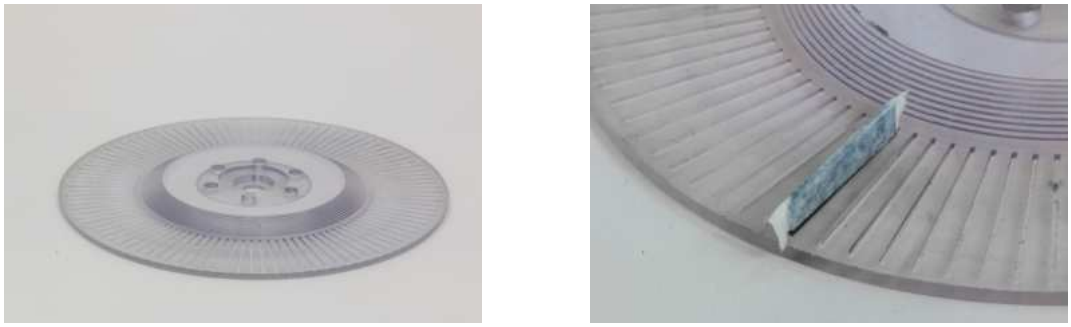

(a) (b)

rotor unrestrained motion.

For the bearing housings and shafts, a mechanical press was used to place the roller bearings with an interference fit. The same press was employed to couple the shafts to their respective bearings, also with an interference fit. The bearing houses, along with their coupled shafts, were then bolted to the motor rack aluminum profiles, as in Fig. 4.12a. Subsequently, the rotor was assembled into the rotating shaft (see Fig. 4.12b). In Fig. 4.12c, nylon bolts were used for coupling to avoid interaction with the magnetic field and, therefore, interference on the rotor's motion. Some adjustments were required to properly align the rotor, the shaft and the magnetic circuit, finishing the assembling as presented in Fig. 4.12d and Fig. 4.12e.

Figure 4.11 – Details of the Gd fins bonding process.

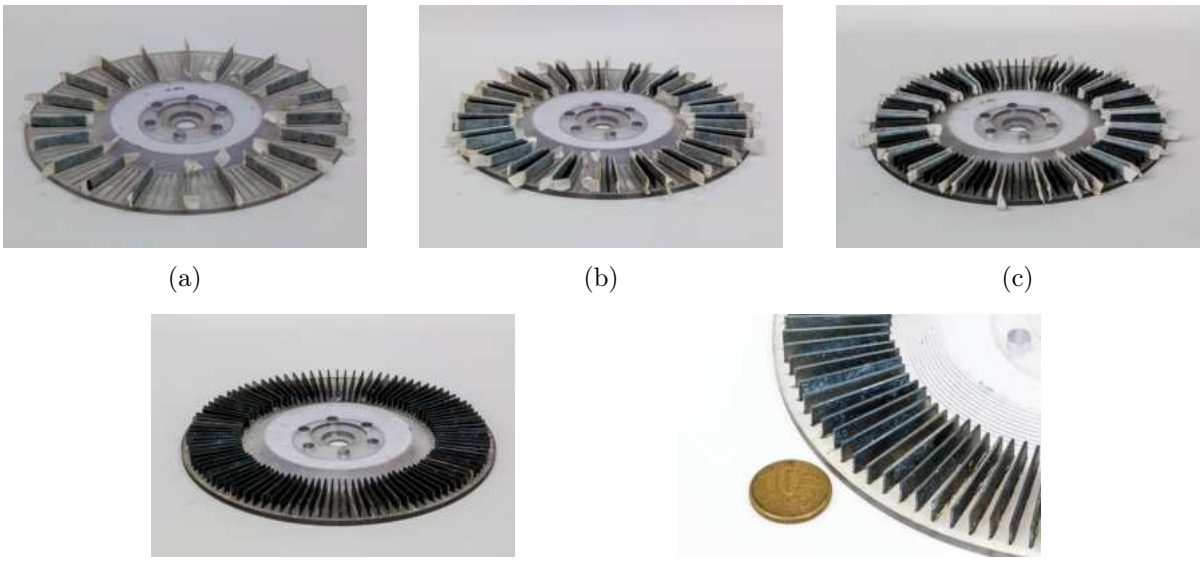

(a) (b) (c)

(d) (e)

Figure 4.12 – Transmission system and rotor assembly: (a) upper and lower rotational shafts connected to the motor rack by their respective bearing houses; (b) rotor assembly to the lower shaft; (c) complete assembly of the rotor and the transmission system; (d) transmission system centralized with the MC and; (e) details of the finned rotor and the MC after the final assembly.

(a)

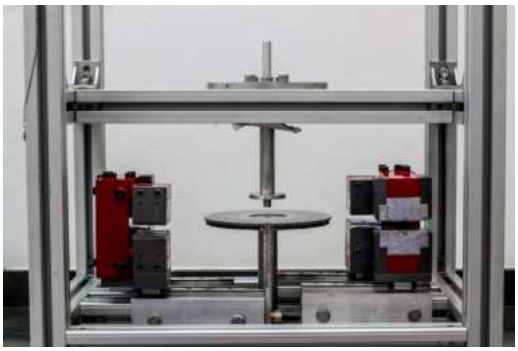

(b)

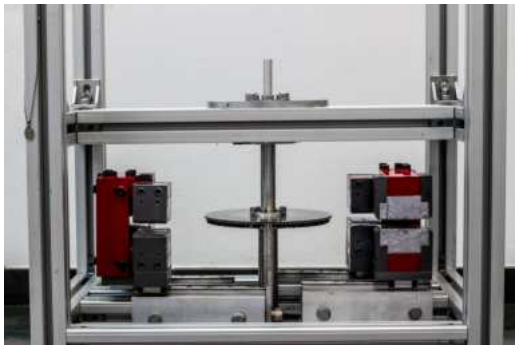

(c)

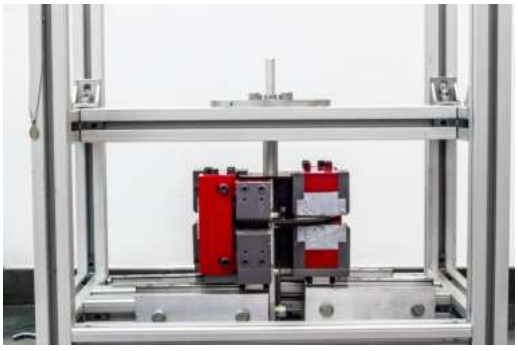

(d)

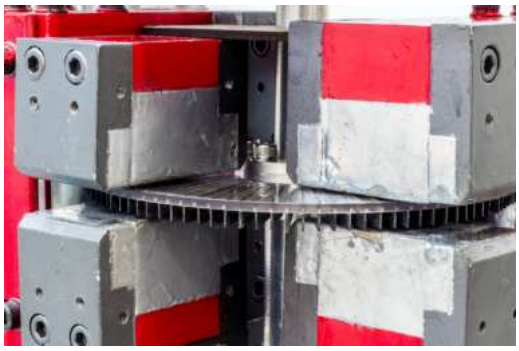

(e)

4.6 FLUID DISTRIBUTION SYSTEM

For the operation of the TMM prototype, it is necessary to deliver warm and cold fluid streams to specific positions along the rotor circumference, in accordance with the magnetic field gradient. Depending on the rotor dimensions, it is important to determine how many fins will be exchanging heat with the fluid streams. For the present design, for instance, three Gd fins are cooled or heated at the same time.Thus, divergent nozzles have been designed to fill, simultaneously, the four channels formed among three adjacent fins.

The PETG plastic nozzles, fabricated in-house via 3D printing, were designed with lateral inclinations of 20° for the cold-fluid nozzles and 12.7° for the warm-fluid ones, as in Fig. 4.13. These angles ensure that the flow is parallel to the longitudinal direction of the channel and, as a result, there is no flow forces contribution to the rotor operation. This is, the generated rotation is primarily driven by the magnetic force imbalance. In addition, the warm fluid nozzles have extended tips, allowing them to be positioned within the air gap. The fabricated nozzles are shown in Fig. 4.14. The methodology used to determine the nozzle positioning along the rotor circumference for the performance characterization tests is presented in Sec. 4.8.

The warm and cold fluid streams are supplied by a fluid treatment station designed for testing TMM prototypes. The treatment station has two identical independent sides, one for the warm and one for the cold fluid. Each side has a reservoir with a coil heat exchanger, which is controlled by a thermal bath. A self-suctioning pump (Dancor, model AP-3C) delivers the fluid to a plate heat exchanger, which is regulated by a second thermal bath. In total, four thermal baths are required.

Figure 4.13 – Divergent nozzle design.

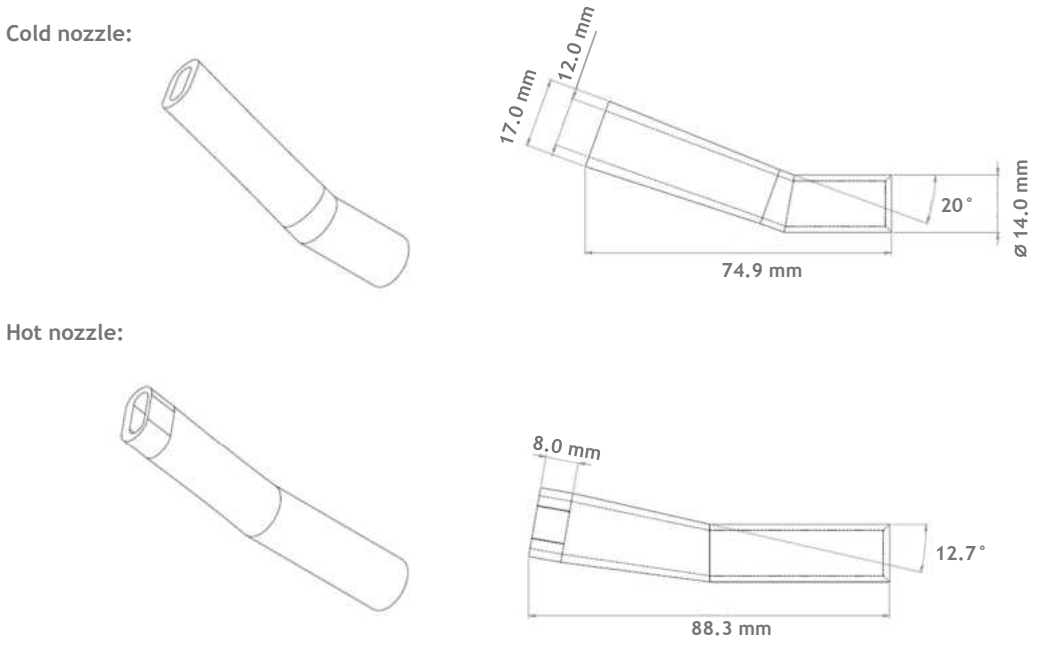

Figure 4.14 – Divergent nozzles fabricated in PETG plastic to allow the fluid to fill, simultaneously, four channels formed among three adjacent fins : (a) warm stream nozzle; (b) cold stream nozzle and (c) both nozzles, highlighting the difference of their lateral inclinations.

(a)

(b)

(c)

After the plate heat exchanger, a flow meter (IFM, model SBG 234) is installed, followed by a manifold that evenly distributes the fluid streams to their respective rotor regions. At the manifold shell, a pressure transducer (IFM, model PN 2515) and a calibrated T-type thermocouple are installed. Fig. 4.15 shows the distribution lines and the measurement instruments for both two- and four-magnetic-volumes configuration. The measurement instruments uncertainties, along with the data acquisition process, will be further detailed in Sec. 4.7.

During TMM operation, the warm and cold fluids discharged from the channels between adjacent MM fins are mixed and temporarily stored in an acrylic collection container. After the test is completed, the fluid mixture returns to the thermal reservoirs via a return pipeline, where it is reconditioned in preparation for the next test.

The total flow rates for the warm and cold sides are independently adjusted using control valves and a bypass system positioned before the plate heat exchanger. These valves are adjusted whenever the total flow rate or the temperature of the cold or warm reservoirs need to be changed, ensuring they match the prescribed values before each test. At the exit of the manifold, four independent control valves are regulated to guarantee equal

Figure 4.15 – Distribution lines and measurement instruments: (a) two-magnetic-volumes configuration; (b) four-magnetic-volumes-configuration and (c) overall view, highlighting measurement instruments.

(a)

(b)

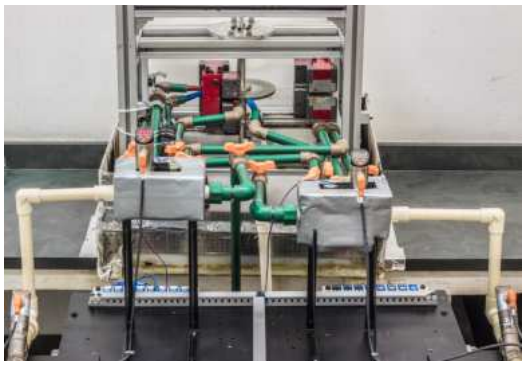

(c)

flow rates at each nozzle. Finally, a secondary bypass system is installed at the manifold to direct the fluid back to the conditioning reservoir prior to motor startup. This allows the fluid remaining in the main pipeline between operations to be replaced with pre-conditioned fluid, thereby reducing the motor's transient operating period. A schematic drawing of the station for the two-magnetic-volume configuration is shown in Fig. 4.16. The unique difference in the four-magnetic-volume configuration is the increased number of fluid outlets from the manifold and nozzles.

4.7 INSTRUMENTATION AND DATA ACQUISITION

The technical specifications and the corresponding uncertainties of the measurement instruments used in the experiments are summarized in Table 4.2. The pressure and flow rate measurements were acquired using a programmable logic controller (PLC) (Altus, model XP340). The temperature readings were obtained through a Field Logger (Novus, model 128-K), which was connected with the same PLC to ensure synchronized data acquisition. The measures were processed in a computer supplied with Master Tools integrated development environment, where the measured variables are graphically evaluated and saved for further post-processing. Except for the temperature probes, whose uncertainties were determined through an in-house calibration procedure, all other instrument uncertainties were obtained from their respective technical catalogs.

Figure 4.16 – Schematic drawing of the fluid treatent station for the two-magnetic-volumes configuration depicting all its main components.

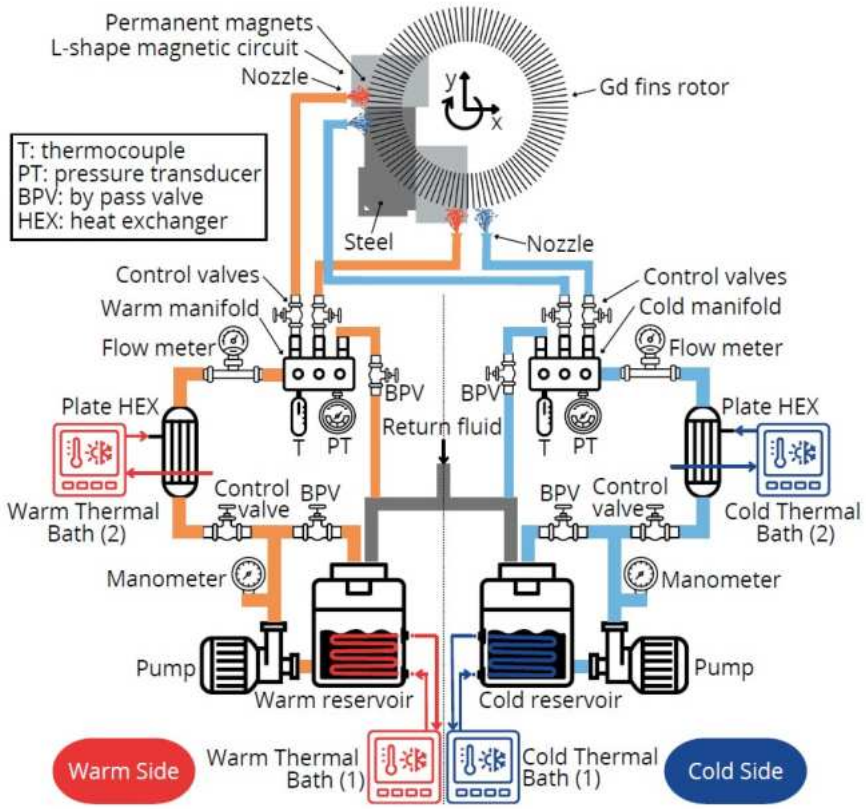

The temperature probes consist of T-type thermocouples, which were calibrated using a reference RTD with an uncertainty of 0.22°C. During calibration, the thermocouples and the RTD were closely placed inside a thermostatic bath to ensure uniform thermal conditions. The bath temperature ranged from 0°C to 50°C within a 5°C interval. After the reference temperature stabilization, the probe's readings were collected over 5 minutes and subsequently averaged. The maximum uncertainty obtained was 0.49°C, which was taken as the reference value to all the temperature measurements. In addition, each thermocouple calibration curve was directly implemented into the PLC for real-time correction.

To measure torque and rotational speed, a servomotor was coupled to the rotating shaft using a flexible mechanical coupling, as in Fig. 4.17. During the test, the servomotor and its servo drive were used to apply a controlled load to the shaft, while simultaneously measuring the torque and the rotor's rotational velocity. Note that the servo drive input

Table 4.2 – Instruments technical specifications.

Sensor	Comp.	Model	Uncertainty
Temperature probe	Omega	PR-T-24-SLE-100	0.49°C
Pressure transducer	IFM	PN 2512	0.007 bar
Volumetric flow rate transducer	IFM	SBG 234	0.5 LPM

Figure 4.17 – Servomotor used for imposing loading to the shaft and for torque measurements coupled to the rotating shaft using a flexible mechanical coupling.

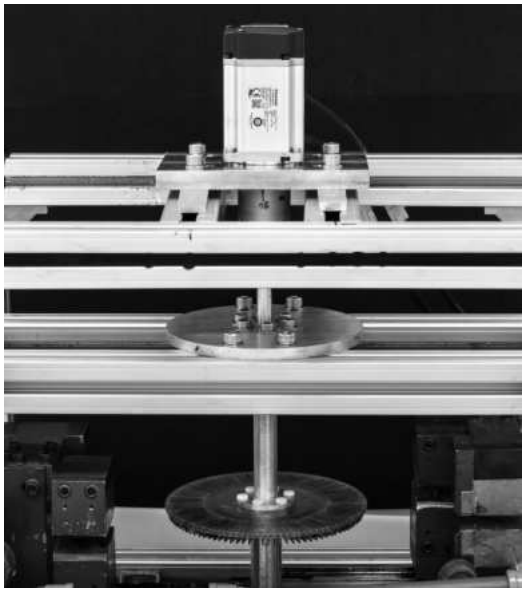

speed must be set to zero, ensuring that only the specified load is applied. A lower-capacity servomotor (Panasonic, model MSMF042L1S2), with a rated torque of 1.27 N·m, was used for tests involving lower torque outputs, while a higher-capacity unit (Panasonic, model MDMF202L1H6M), with a rated torque of 9.55 N·m, was employed for tests involving larger torque output. This innovative approach for measuring torque and rotational speed is presented and discussed elsewhere (MICHEL et al., 2025).

The torque and rotational speed measurements were acquired in a PLC (Altus, model XP340), which is time-synchronized with the operational parameters acquisition (pressure, volumetric flow rate and temperature). In this work, systematic and random errors in the rotational speed measurements were disregarded.

A data acquisition rate of 500.0 ms was used for the performance characterization tests, resulting in approximately 120 data points per test. Each test had an average duration of one minute. The final rotational speed is the average value over 10 s to 30 s interval, depending on the test conditions. Additionally, a digital first-order low-pass filter, with a time constant of 1.0 s, was applied to the rotational speed measurements to smooth out fluctuations caused by transmission system misalignment.

The uncertainty for the rotational speed combines the uncertainties from the servomotor and the type A uncertainties. The latter were obtained from a sample of five measurements, and further calculated using the same methodology detailed in Sec 4.3.3. The expanded uncertainty of the digital encoder is significantly smaller than that of the type A. The final uncertainty in rotational speed was evaluated at 3.73 RPM, while the torque uncertainties for the lower- and higher-capacity servomotors were 0.006 N·m and 0.06 N·m, respectively.

Figure 4.18 – Tested combinations of the warm and cold nozzle positioning with respect to the magnetic field gradient distribution. Regions (1) and (2) are for warm blow, and (3) and (4) for the cold blow.

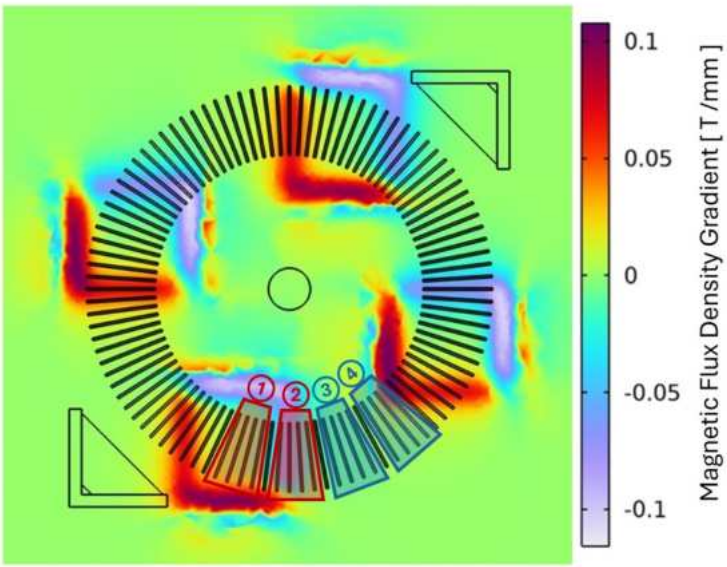

4.8 PRELIMINARY ADJUSTMENTS

Prior to conducting the performance tests, some preliminary adjustments were required. These included: (A) adjusting the flow rates for each nozzle; (B) identifying the positions of the cold and warm nozzles; and (C) determining the residual torque resulting from mechanical losses and component inertia.

Initially, after assembling the manifold, piping, and nozzles, it was essential to ensure equal flow rates through each nozzle. To verify this, a test setup was conducted in which the fluid exiting each cold or warm nozzle was collected over a fixed time period, and the resulting volumes were measured. If discrepancies were observed in the collected volumes, the control valves at the manifold outlets were adjusted accordingly and the test was repeated until uniform volumes were obtained across all nozzles. This procedure was carried out for the minimum and maximum tested flow rates, and for the TMM prototype configured with either two or four magnetic volumes.

The positioning of the nozzles around the rotor circumference is defined in accordance with the magnetic field gradient distribution. Multiple position combinations of the warm and cold blow nozzles were tested to evaluate its impact on the rotational speed and generated torque. For both, two different positions were selected, as illustrated in Fig. 4.18. Regions (1) and (2) correspond to the warm fluid stream, while regions (3) and (4) correspond to the cold fluid stream.The tests considered the combination (1)-(3); (1)-(4), and (2)-(3), and the main observations and conclusions are summarized in Table 4.3.

The motor operated continuously for the combination (1)-(3), and failed to operate for the combination (1)-(4). As a conclusion, the cold nozzle should be fixed at position (3).

Table 4.3 – Observations and conclusions from positioning investigation of the warm and cold flow nozzles.

Combination	Continuous Operation	Results
(1)-(3)	Yes	Achieved higher torques
(1)-(4)	No	-
(2)-(3)	Yes	Achieved higher rotational velocities

Next, for the combination (2)-(3) it was also able to operate continuously. Comparing now the cases (1)-(3) and (2)-(3), the first resulted in greater torque output, while the latter achieved higher rotational speeds.

These results can be attributed to the relationship between the warm flow region and the peak magnetic field gradient. Notably, position (2) coincides with the location of the peak field gradient, which reduces the net force and consequently lowers the generated torque. As the MM is transitioning to the paramagnetic phase upon entering the high-field region, this decreases motion resistance, thereby enabling higher rotational speeds. However, to meet the primary objectives of the prototype design, higher torque was prioritized over angular speed. As a result, the (1)-(3) nozzle configuration was identified as the most favorable. Images of the final nozzle positions are presented in Fig. 4.19, where the red nozzle corresponds to the warm side and the blue nozzle to the cold side.

Lastly, an experimental test was carried out to determine the residual load of the transmission system. This load can be attributed to mechanical losses, mainly due to misalignmentsalong the transmission system (shaft, rotor and torque measurement system), as well as to the inertia of the components. For this test, the MC was moved away from the MM rotor, as showed in Fig. 4.17. This prevents the interference of the magnetic forces. The residual load was evaluated as the minimum torque input where the MM rotor starts to rotate at a prescribed rotational speed. Thus, unlike the tests that use the servomotor and servo drive to measure torque and rotational speed, these tests require setting a specific speed on the servo drive. The speeds used were 20, 30, 50, 75, 100, 150, 200, and 300

Figure 4.19 – Warm (red) and cold (blue) nozzles positions along the rotor circumference: (a) MC overall view; (b) detailed view.

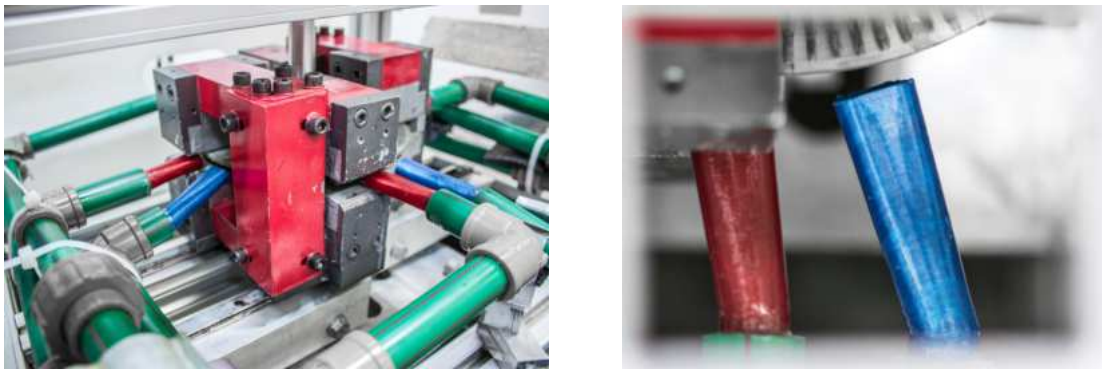

(a) (b)

Figure 4.20 – TMM configurations for the performance characterization tests: (a) two-magnetic-volumes configuration (I); (b) four-magnetic-volumes configuration (II).

(a) (b)

RPM. The residual load was ultimately determined to be 0.05 N·m for the lower-capacity and 0.17 N·m for the higher-capacity servomotor, independent of the rotor's speed. The higher load in the latter is attributed to its greater inertia.

4.9 PERFORMANCE CHARACTERIZATION TESTS

The performance characterization tests involved measuring the motor's rotational speed (ω) and torque (τ) under various operating conditions. Then, the produced power can be calculated by Eq. 4.9, where ω is in units of (rad/s):

$$\dot{W}_{prod} = \omega\tau \tag{4.9}$$

In this way, the performance tests are evaluated and compared using of two different curves: torque as a function of the rotational speed ($\tau \times \omega$) and power as a function of the rotational speed ($\dot{W}_{prod} \times \omega$). These curves were obtained for the two different configurations of the prototype: (I) using a single L-shaped assembly (Fig. 4.20a), resulting in two magnetic volumes and, (II) employing the complete MC (Fig. 4.20b), comprising four magnetic volumes.

Distinct operating parameters were applied to configurations (I) and (II). In configuration (I), the prototype was tested under different heat source temperatures (T_H), heat sink temperatures (T_C), and varying warm and cold blow volumetric flow rates ($\dot{\vartheta}_H$ and $\dot{\vartheta}_C$). In configuration (II), only the flow rates were varied, while T_H and T_C were kept constant. It is important to mention that for all tests $\dot{\vartheta}_H = \dot{\vartheta}_C$.

The operating conditions are detailed in the next section. The combination of the two prototype configurations and all operating conditions resulted in a total of 252 experimental tests.

Table 4.4 – Operating conditions for the experimental tests.

Configuration	Volumetric Flow Rate per Nozzle [LPM/nozzle]	Total Volumetric Flow Rate [LPM]	Cold Stream Temperature [°C]	Warm Stream Temperature [°C]
(I) 2-poles	10	20	5	35 to 50; steps of 5°C
(I) 2-poles	10	20	10	45 and 50
(I) 2-poles	5, 6.25, 7.5, 8.5, 10, 12.5, 15, 17, 20 and 22.5	10, 12.5, 15, 17, 20, 25, 30, 34, 40 and 45	5	45
(II) 4-poles	5, 7.5, 8.5, 10 and 11.75	20, 30, 34, 40 and 47	5	45

4.10 OPERATING CONDITIONS

Table 4.4 summarizes the test conditions for both configurations (I) and (II). The cold and warm temperatures were selected around the magnetic phase transition temperature of gadolinium (T_T = 293 K). Due to limitations of the available cooling system, the minimum temperature was set to 5°C, while the maximum temperature was set to 50°C with no constraints on heating. This range allowed for testing under both balanced and unbalanced temperature differences. The balanced condition occurs when the cold and warm stream temperatures have equal differences from T_T, such as 5°C and 35°C. All other combinations correspond to unbalanced conditions.

Volumetric flow rate values were selected to evaluate the dependence of $\tau \times \omega$ and $\dot{W}_{prod} \times \omega$ curves with respect to flow rate variations, especially when doubling, tripling, and quadrupling the flow rate values. However, the fluid treatment station is limited to a maximum of 45 LPM for the two-magnetic-volumes configuration (I) and of 47 LPM for the four-magnetic-volumes one (II).

The flow rate and fluid temperature directly influence both the flow regime and the associated heat transfer characteristics. These influences can be represented by the Reynolds number (Re) and the Nusselt number (Nu). The former represents the ratio between inertial and viscous forces in the flow, while the latter indicates the ratio between heat transfer by convection and that by conduction alone. To qualitatively estimate the expected ranges of these dimensionless numbers, several assumptions are made: (a) the working fluid is mixture of water and ethylene glycol (10%vol); (b) the flow is uniformly distributed into three channels; (c) the channel geometry is a closed rectangular cross-section; (d) the channel cross-section varies with the channel length. The correlations employed for calculating the Nusselt number are those proposed by EES (2024) and Nellis e Klein (2021), presented in Eq. 4.10 and for laminar flows and Eq. 4.11 for turbulent flows. In these

expressions, AR denotes the duct aspect ratio (the ratio of its minimum to maximum dimensions), PR is the Prandtl number, and f_{fd} is the fully developed friction factor. According to these correlations, the transition from laminar to turbulent flow is assumed to occur at Re values in the range of 2300 to 3000. The Re and Nu values are further analyzed under the operating conditions specified in Table 4.4.

$$Nu_{D_h,T,f_{fd}} = 7.541\left(1 - 2.610AR + 4.970AR^2 - 5.119AR^3 + 2.702AR^4 - 0.548AR^5\right) \tag{4.10}$$

$$Nu_{D_h,f_{fd}} = \frac{\left(\frac{f_{fd}}{8}\right)\left(Re_{D_h} - 1000\right)Pr}{1 + 12.7\left(Pr^{\frac{2}{3}} - 1\right)\sqrt{\frac{f_{fd}}{8}}} \tag{4.11}$$

Due to the converging geometry of the channel, the cross-sectional area varies along its length, resulting in changes in the local Re and Nu. These parameters are presented in Fig. 4.21a and Fig. 4.21b for inlet temperatures of $T_C = 5°C$ and $T_H = 45°C$, and volumetric flow rates of 5 LPM/nozzle and 10LPM/nozzle. At the lower flow rate of 5 LPM/nozzle, the Re is within the transitional flow regime. Furthermore, it is observed that along the channel length, the thermal boundary layers are not fully developed. As a result, elevated Nu values are expected. As shown in Fig. 4.21b, the Nusselt number tends to increase with Reynolds number; however, for the case of 5LPM/nozzle, Nu initially decreases along the channel length, which can be attributed to the gradual development of the boundary layer in the transitional flow regime. Beyond approximately 10 mm, the flow becomes fully turbulent, and Nu increases almost linearly along the channel.

Because of their approximately linear variation along the channel length, the following analysis considers the average values of Re and Nu, evaluated at the average channel cross-sectional area. Table 4.5 shows the average Re and Nu values for different combinations of warm (Re_H, Nu_H) and cold (Re_C, Nu_C) fluid inlet temperatures, at a fixed flow rate of 10 LPM/nozzle. The results indicate that the increasing temperatures, lead to higher Re and Nu values, thereby enhancing the heat transfer rates. Lastly, Fig. 4.22 presents the dependence of the average Re and Nu on the flow rate across the tested range, with inlet temperatures fixed at 5°C for the cold stream and 45°C for the warm stream. It is evident that the flow regime is always turbulent. Also, higher flow rates result in increased Re and Nu values, which correspond to improved heat transfer performance. Furthermore, for the same flow rate, the hot fluid stream consistently exhibits higher Re and Nu values than the cold stream.

Figure 4.21 – Local dimensionless numbers as a function of the converging channel length: (a) Reynolds number; (b) Nusselt number.

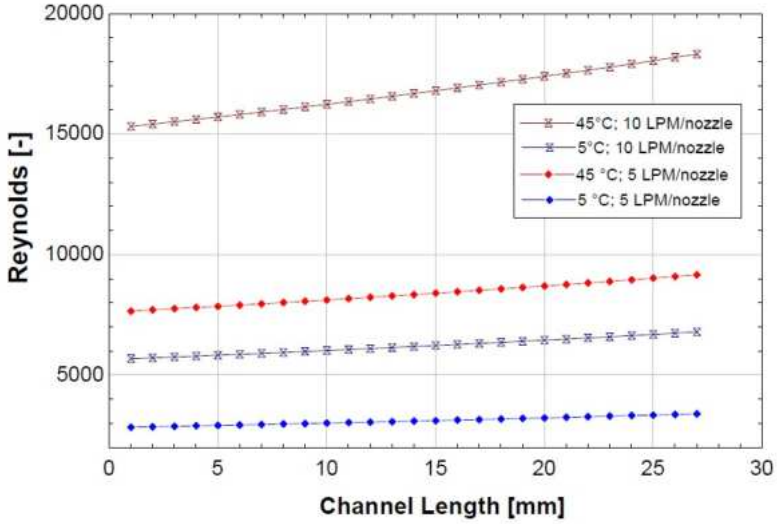

(a)

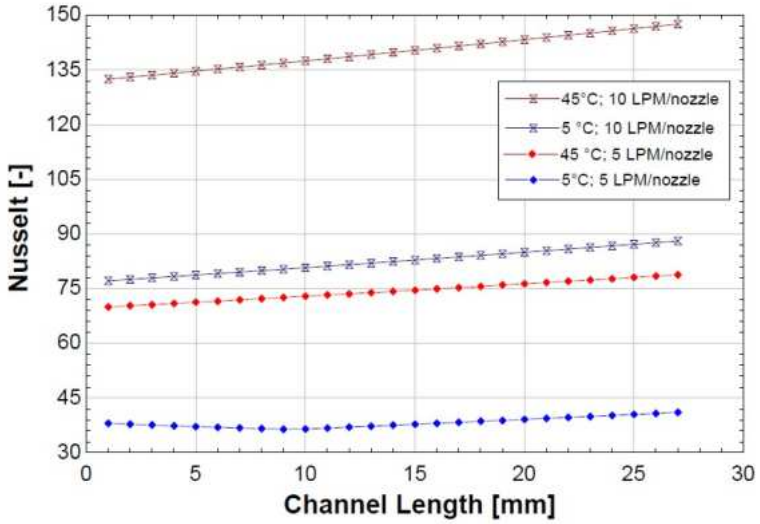

(b)

Table 4.5 – Average Re and Nu for different combinations of warm and cold fluid temperatures at a flow rate of 10 LPM/nozzle

T_C [°C]	T_H [°C]	Re_C	Re_H	Nu_C	Nu_H
5	35	6206	13738	82.65	128.1
	40	6206	15219	82.65	134.3
	4	6206	16740	82.65	140.1
	5	6206	18290	82.65	145.6
10	45	7258	16740	91.08	140.1
	50	7258	18290	91.08	145.6

Figure 4.22 – Avarage dimensionless numbers with inlet temperatures fixed at 5°C for the cold stream and 45°C for the hot stream: (a) Reynolds number; (b) Nusselt number.

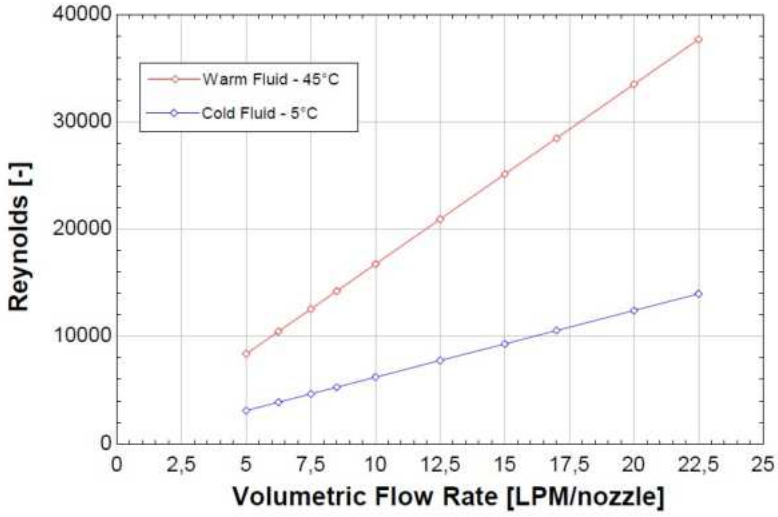

(a)

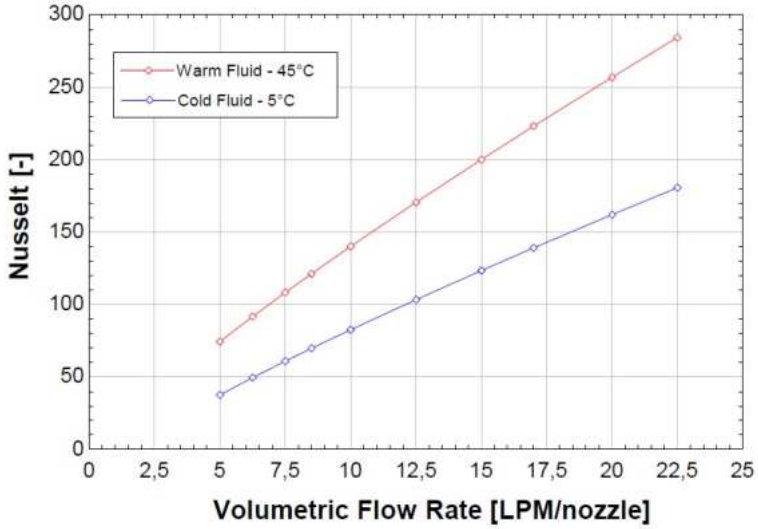

(b)

5 RESULTS AND DISCUSSION

5.1 MAGNETIC CIRCUIT

One of the design strategies considered for the MC design was the incorporation of side concentrators to reduce the magnetic flux leakage, thereby improving the magnetic field intensity and uniformity within the magnetic air gap. Fig 5.1 presents the magnetic flux density distribution in a cross-section view of the magnetic volume, including a pair of permanent magnets and their respective side concentrators. The black arrows indicate the magnetic flux direction.

Moreover, Fig. 5.2 shows the simulation results for the magnetic flux density and its gradient distribution along the MM rotor circumference, obtained by averaging their values in the gadolinium fin volume. Fin number one corresponds to the 0 ° angular position indicated in Fig 4.5, and the profile is evaluated in the clockwise direction from that reference point. In accordance with the simulations, the maximum numerical magnetic field intensity is 1.03 T, while the peak magnetic flux density gradient reached 0.07 T/deg. In addition, the simulation results for the magnetic flux density and its gradient distribution along the MC angular position, calculated in a cut plane at the center of the magnetic volume air gap, are depicted in Fig. 5.3. The figure also illustrates the positions of the Gd fins relative to these distributions.

Regarding the MC experimental characterization, a comparison between the experimental and simulated magnetic flux density values is presented in Fig. 5.4. These results were

Figure 5.1 – Simulation result for the magnetic flux density distribution in a magnetic volume cross section, highlighting the side concentrators effect on the produced magnetic field.

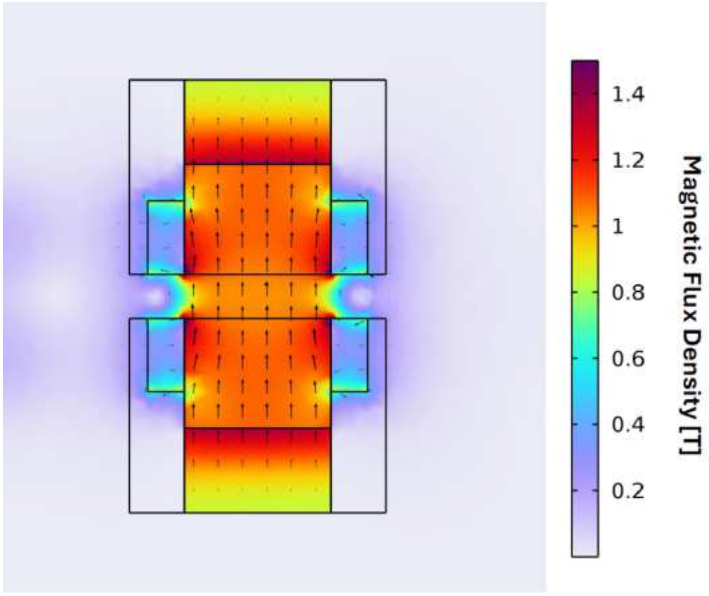

Figure 5.2 – Simulation results, averaged in the Gd fin volume, along the rotor circumference: (a) magnetic flux density distribution; (b) magnetic flux density gradient distribution.

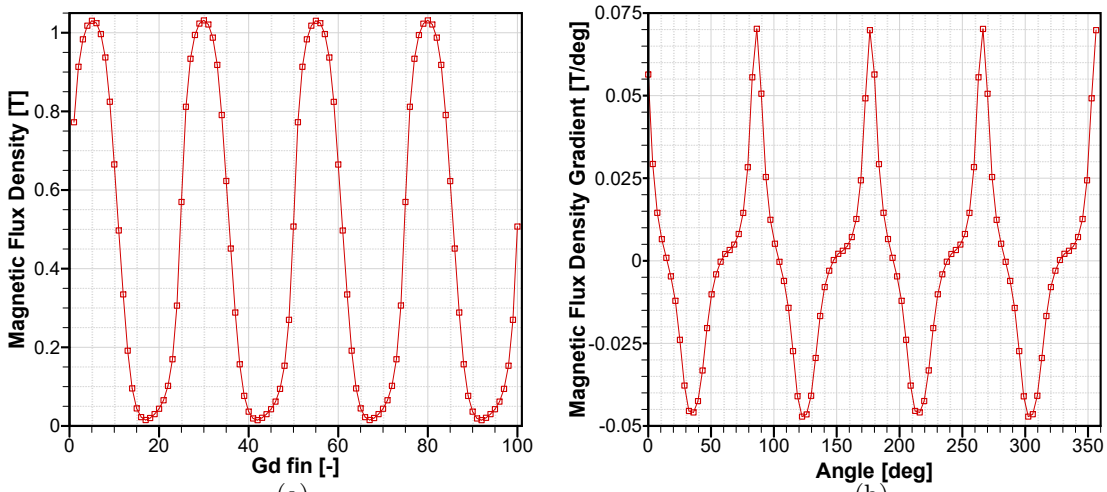

(a) (b)

Figure 5.3 – Simulation results in a cut plane at the magnetic gap center: (a) magnetic flux density intensity distribution ; (b) magnetic flux density gradient distribution.

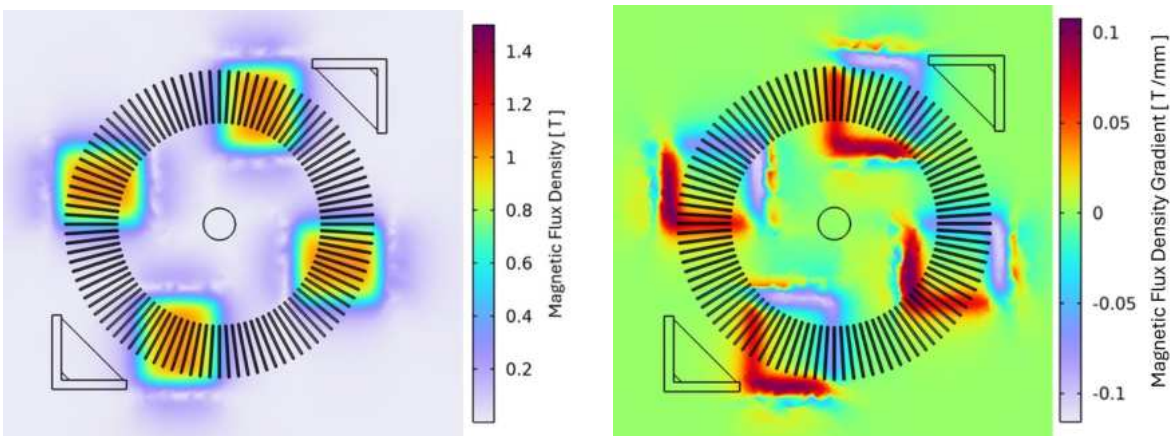

(a) (b)

obtained along the angular position at the center of the air gap, represented by the dashed circle in Fig. 4.5, where the angular position corresponding to 0° is also indicated. Results obtained along other radial positions are presented in Appendix B.

The maximum differences between the numerical and experimental results are observed at the peak values, where the largest one is about 0.029 T out of 1.06 T (2.7%). This falls within the range of experimental uncertainty of ±0.07 T. These discrepancies can be attributed to some deviations from the designed specifications during production and assembly, as well as some irregularities in the permanent magnets used. As a result, some regions of the magnetic field presented a thinner air gap than the designed value. However, notably the experimental results show a good agreement with the simulated values, reinforcing confidence in the reliability of the design, production, and assembly methodologies employed.

Figure 5.4 – Magnetic flux dentisty along the angular position at the center of the air gap: comparison between the experimental and numerical results.

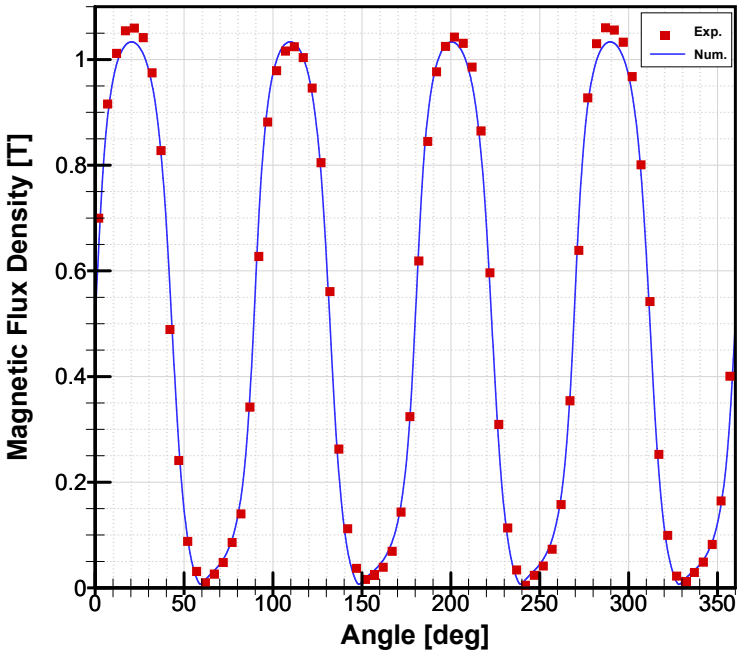

5.2 DEMONSTRATING THE PROOF-OF-CONCEPT

According to the current laboratory structure, performance tests can be conducted at a maximum volumetric flow rate of 47 LPM distributed across four cold or four warm flow lines, in the four-magnetic-volumes configuration; or up to 45 LPM distributed between two cold or two warm flow lines, in the two-magnetic-volumes configuration. Hence, for the latter configuration, the maximum flow rate at each nozzle is 22.5 LPM/nozzle. The nozzles have a cross-sectional area of 49.7 mm^2, resulting in flow velocities of up to 7.5 m/s (at 22.5 LPM/nozzle). Although the fin rotor was not designed to experience reactive forces from the flow, it can be pointed out that the rotary motion may, at least in part, be influenced by flow forces rather than the balance of magnetic forces.

To determine whether flow forces contribute to the rotary motion, two separate tests were conducted in the two-magnetic-volumes configuration. The first test used only warm fluid at 45 °C and 17 LPM/nozzle at all four nozzles. The second test involved supplying warm fluid at 45 °C and 17 LPM/nozzle at the two warm nozzles, and cold fluid at 5 °C and 17 LPM/nozzle at the two cold nozzles. Both tests were supported by thermographic visualization, as shown in Fig. 5.5.

The expected result was that, when operating the rotor at 45 °C, the paramagnetic phase would be established, thereby minimizing magnetic forces and allowing the rotor to rotate freely. Thus, if flow forces are significant, this would cause the rotor to spin. However, as shown in Fig. 5.5a, the rotor remained stationary throughout the test. In contrast, when

Figure 5.5 – Thermographic images of the thermomagnetic motor during operation: (a) first test condition with only warm fluid at 45 °C and 17 LPM/nozzle at all four nozzles; (b) second test condition with warm fluid at 45 °C and 17 LPM/nozzle at the two warm flow nozzles, and cold fluid at 5 °C and 17 LPM/nozzle at the two cold flow nozzles.

(a)

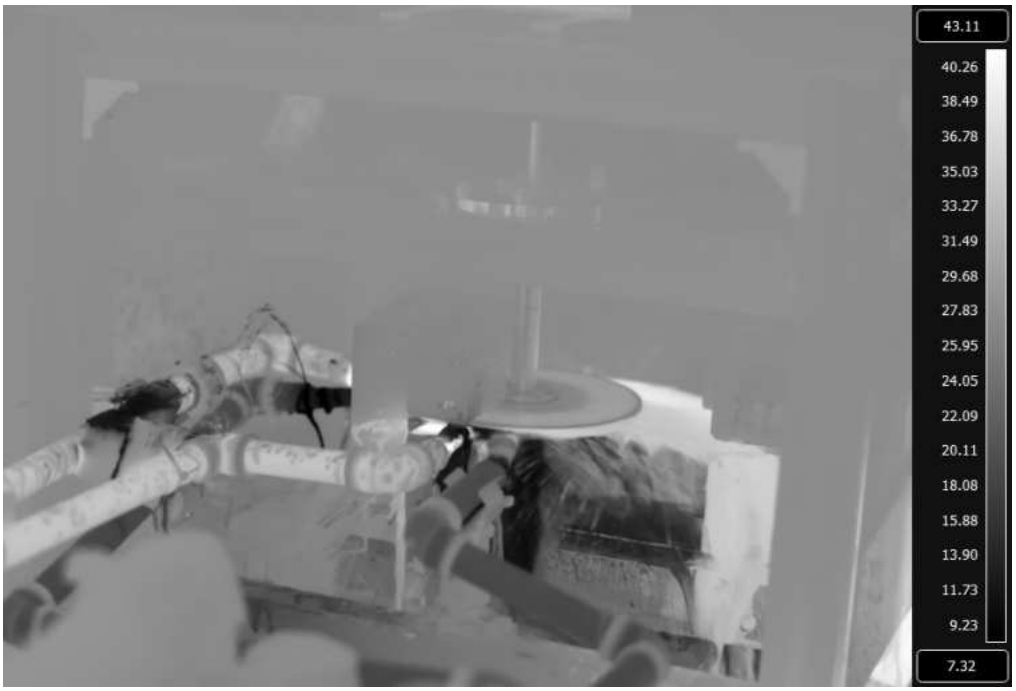

(b)

the second test condition with both cold and warm fluids was applied, the rotor spun, as seen in Fig. 5.5b. This demonstrates that the movement is solely due to the imbalance of magnetic forces, with no contribution from flow forces.

5.3 MEASUREMENTS AND DATA ANALYSIS

Typical time-dependent measurement data for warm and cold streams temperatures, volumetric flow rates, and pressure are shown in Fig. 5.6. As can be noted, the system requires a few seconds to stabilize at the desired input conditions for temperature and flow rates. Consequently, data analysis should focus on the final stabilized values, using the averaged values for these variables.

Throughout the tests, the rotor demonstrated continuous and smooth rotary motion under most operating conditions, fulfilling one of the key requirements of the prototype. Exceptions were observed during tests at lower flow rates, specifically: (i) 5 LPM/nozzle and 6.25 LPM/nozzle for the two-magnetic-volume configuration;(ii) 5 LPM/nozzle, 7.5 LPM/nozzle, and 8.5 LPM/nozzle for the four-magnetic-volumes configuration; and (iii) under high load inputs. At these conditions, the rotor exhibited a few oscillations on its direction of movement, however, the net displacement still occurred correctly in the clockwise direction.

Figure 5.7 shows comparisons of the time-dependent rotational speed under two different conditions. Fig 5.7a presents the results from no-load tests, in which no load (aside from the residual one) is applied to the rotational shaft, for the two-magnetic-volumes configuration. In this figure two different flow rates are taken: the lowest tested rate of 5 LPM/nozzle and a higher rate of 17 LPM/nozzle. As can be observed, after an initial transient period caused by inertia, the rotor spins continuously at approximately 217.7 RPM for the 17 LPM/nozzle condition. In contrast, for the 5 LPM/nozzle condition, the rotor exhibits non-continuous operation, with the rotational speed fluctuating between high and low values.

In Fig. 5.7b a comparison between two tests performed in the four-magnetic-volumes configuration is presented. Both tests were conducted at the flow rate of 11.75 LPM/nozzle, and under load conditions of: 0.16 N·m and 0.86 N·m. The load condition refers to the application of a load to the TMM shaft, resulting in a generated torque. For the 0.16 N·m load input, the rotor spins continuously at approximately 132.4 RPM after the initial transient period. In contrast, the rotor exhibits a non-continuous operation for the 0.86 N. load input. The rotational speed value is then calculated as the average over a 10 s interval. It is important to mention that the interval is defined after the temperature and flow rates have stabilized, as shown in Fig. 5.6.

The non-continuous operation observed at the lowest flow rates in no-load tests can be

Figure 5.6 – Time-dependent measurement data for warm and cold streams temperatures, volumetric flow rate, and inlet pressure.

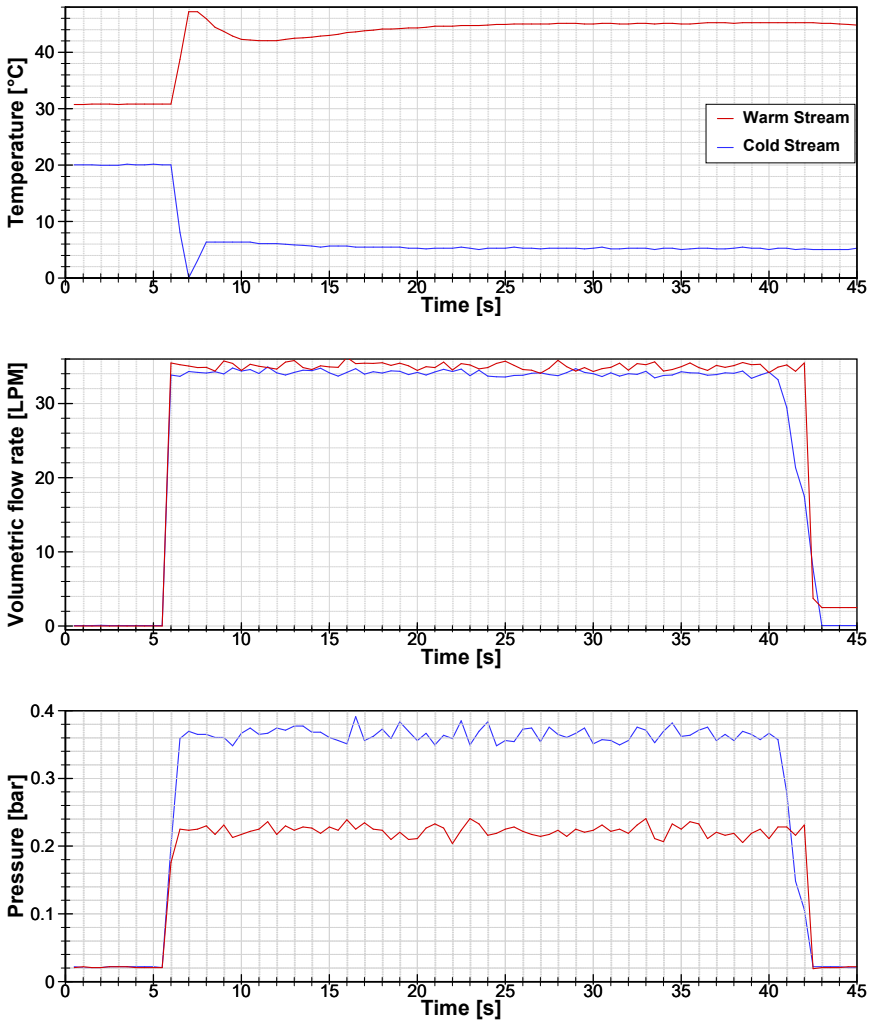

Figure 5.7 – Time-dependent rotational speed under different operating conditions: (a) no-load condition and flow rates of 5 LPM/nozzle (total of 10 LPM) and 17 LPM/nozzle (total of 34 LPM); (b) load condition of 0.16 N·m and 0.86 N·m and fixed flow rate of 11.75 LPM/nozzle. The cold and warm fluid streams temperatures are 5 °C and 45 °C, respectively.

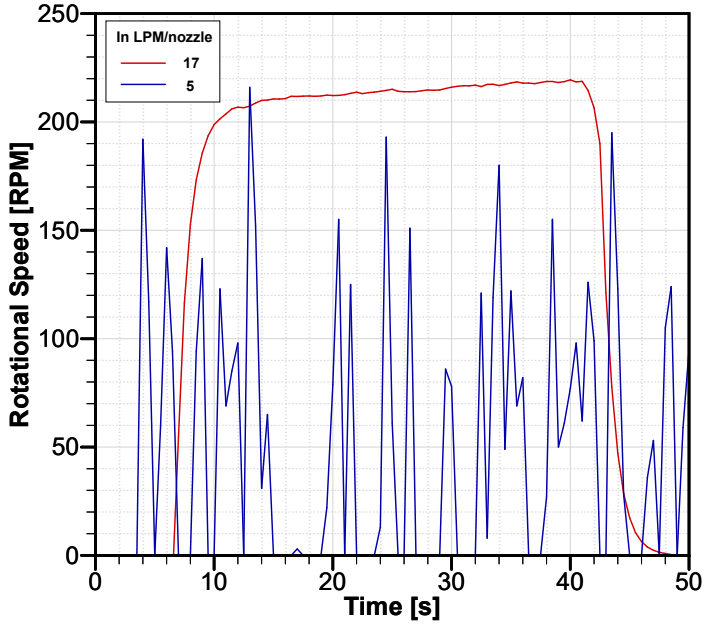

(a)

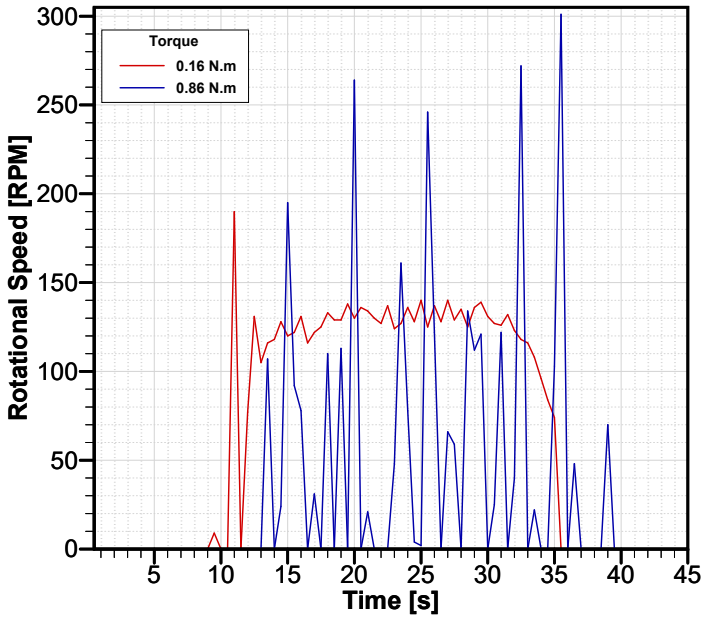

(b)

attributed to the poorer heat transfer under these conditions. The present rotary TMM operates based on the magnetic force balance between the ferromagnetic and paramagnetic phases, which is established in the cold and warm flow regions (nozzles). If the phase transition is not properly achieved, the rotor tends to stop or even rotate in the opposite direction due to the imbalance in magnetic forces. Therefore, a key characteristic of this prototype is the need for high flow rates during operation, to enhance heat transfer, as presented in Fig. 4.22a and 4.22b.

Furthermore, the non-continuous operation under high load inputs can also be associated with the heat transfer rates between the warm and cold fluid streams and the MM. When a load is applied to the rotating shaft, the magnetic force must overcome the opposing mechanical resistance in order to maintain motion. For this to occur, the ferromagnetic phase transition must be properly achieved, thereby increasing the magnetic force. As a result, the rotor may decelerate or even come to a stop while exchanging heat with the fluid streams, and will resume spinning once the magnetic force becomes sufficiently strong to overcome the imposed load. Consequently, as load input increases, the rotor motion becomes more fragmented, approaching the behavior of a stepper motor, until the maximum torque is found, at zero rotational speed.

The raw torque measurements data were post-processed and corrected by adding the residual load, which was experimentally determined as described in Sec. 4.8. The performance characteristic curves, for $\dot{W}_{prod} \times \omega$ and $\tau \times \omega$, with and without the applied correction, are compared in Fig. 5.8. These curves were obtained for both two- and four-magnetic volume configurations at a 10 LPM/nozzle and 11.75 LPM/nozzle flow rates, respectively. The largest discrepancies observed in torque and power values for the four-magnetic-volume configuration are attributed to the use of the larger-capacity servomotor. The servomotors are swapped when the applied load tests exceeds 1.27 N·m. This servomotor, in turn, exhibits greater inertia and residual load.

It is important to mention that all performance curves, whether measured or corrected, exhibited the expected trends for a motor. As shown in Fig.5.8a and Fig.5.8c, at zero or low load input, the TMM operates continuously and achieves high ω at low τ values. As the input load increases, resulting in higher τ, ω is significantly reduced. At certain load conditions, the rotor ceases continuous operation. At zero rotation, the applied load corresponds to the maximum (or static) torque produced by the TMM. As will be discussed later, the maximum torque is dependent on the TMM configuration (two-magnetic or four-magnetic volumes).

Additionally, as in Fig.5.8b and Fig.5.8d, $\dot{W}_{prod}$ approaches zero at the extremes of speed and torque. Specifically, τ tends toward zero at the maximum ω, and the ω reaches zero at maximum τ. At a certain combination of torque and velocity, $\dot{W}_{prod}$ exhibits a peak value. As will be further discussed, the location of this peak, along with the corresponding

Figure 5.8 – Comparison between performance characteristic curves with and without the residual load correction: (a) $\tau \times \omega$ curve for two-magnetic-volumes and 10 LPM/nozzle; (b) $\dot{W}_{prod} \times \omega$ curve for two-magnetic volumes and 10 LPM/nozzle; (c) $\tau \times \omega$ curve for four-magnetic volumes and 11.75 LPM/nozzle and; (d) $\dot{W}_{prod} \times \omega$ curve for four-magnetic-volumes and 11.75 LPM/nozzle.

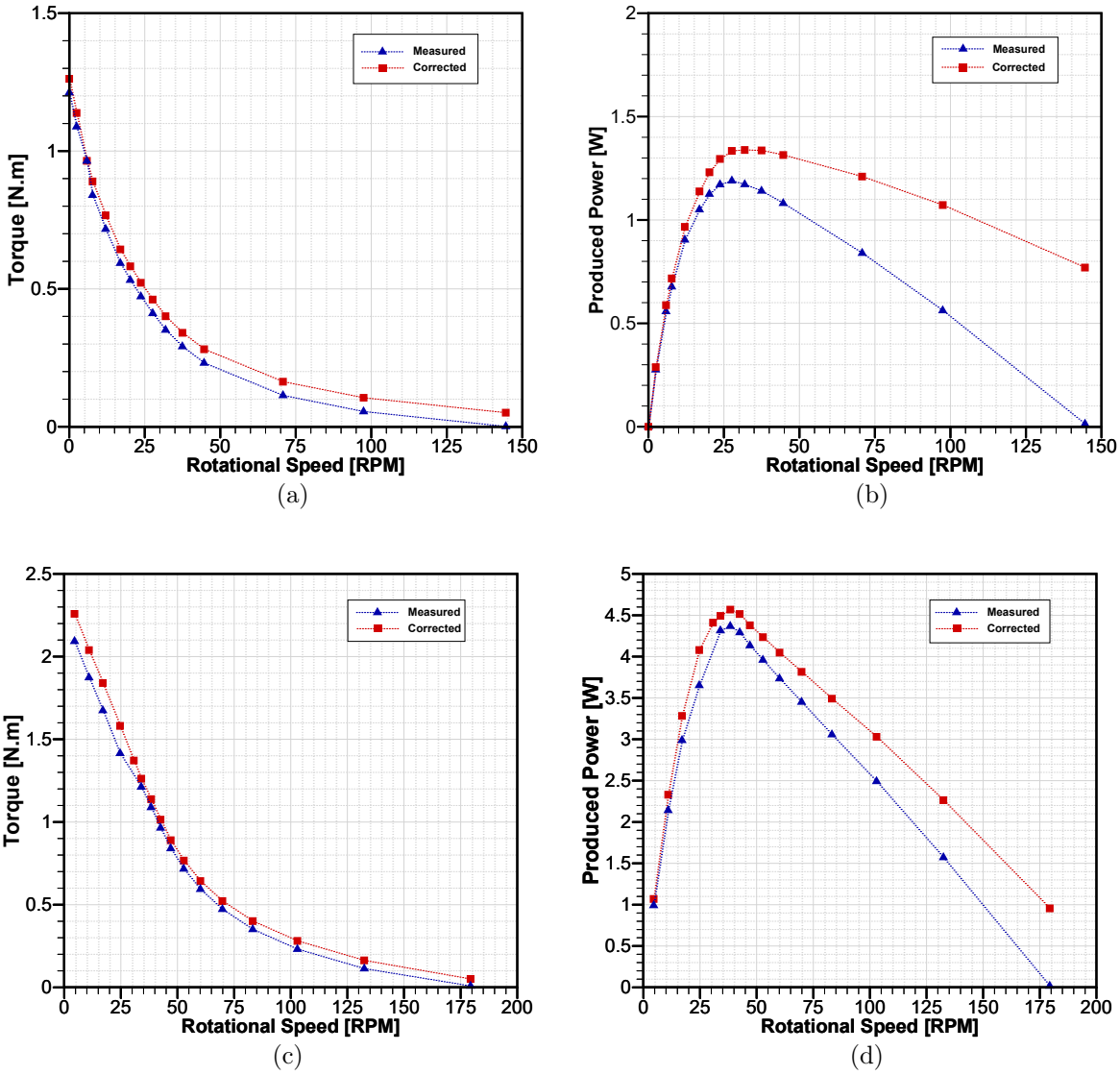

τ and ω values, is influenced by the operating conditions.

All the performance curves and results presented in the following sections account for this residual load correction. Additionally, the presence of the residual load prevents the experimental characterization of the maximum rotational speed attained by the rotor during no-load tests. Consequently, it is likely that higher speeds could be reached in the absence of mechanical losses.

5.4 PERFORMANCE RESULTS

The performance of the proposed TMM is evaluated through measurements of torque and the resulting rotational speed under various operating conditions, including different

stream temperatures (warm and cold) and flow rates. Regarding the TMM configuration, both the two-magnetic-volumes and the four-magnetic-volumes setups are considered. In this context, the $\tau \times \omega$ and $\dot{W}_{prod} \times \omega$ curves are obtained by varying input load, while ω results from the combination of the operating conditions. Notably, $\dot{W}_{prod}$ is an indirect result of the measured torque and rotational speed. Again, the torque and produced power presented in this section are corrected by the residual load due to component inertia and mechanical losses.

5.4.1 INFLUENCE OF THE WARM AND COLD STREAM TEMPERATURES

The influence of the warm and cold fluid streams' temperatures on the TMM performance was evaluated using the two-magnetic-volumes configuration and a flow rate fixed at 10 LPM/nozzle. The first analysis considered the cold fluid temperature fixed at 5°C, while the the warm stream temperature ranged from 35°C to 50°C. The results for both the torque and produced power as functions of the rotor speed are presented in Fig. 5.9. Notice that the maximum torques for the conditions 35°C, 40°C, and 50°C were obtained through an extrapolation method and are shown as hollow symbols in Fig. 5.9a.

It can be observed in Fig. 5.9 that the conditions for $T_H = 45$°C and $T_H = 50$°C resulted in the highest maximum values for the rotational speed (Fig. 5.9c) and for the peak produced power (Fig. 5.9b). This can also be observed on the $\tau \times \omega$ characteristic curves in Fig. 5.9a, as the T_H increases, the resulting rotational speed is higher at the same load input, especially for 45°C. For a warm stream temperature of 35°C, the TMM reaches a maximum rotational speed of 103.3 RPM, a peak produced power of 0.90 W, and a maximum extrapolated torque output of ≈0.9 N·m (Fig. 5.9d). At 45°C, these values increase to 144.5 RPM, 1.34 W, and ≈1.26 N·m, respectively. Nevertheless, no improvement in the motor's performance is observed when T_H is further increased to 50°C. At this temperature, the maximum rotational speed remains almost the same, at 145.2 RPM, the peak produced power decreases to 1.23 W, and the maximum torque reduces to ≈1.0 N·m.

There is a noticeable similarity between the curves of $\tau \times \omega$ and $\dot{W}_{\text{prod}} \times \omega$ for T_H values of 35°C, 40°C, and 45°C. In these cases, the peak power occurs at lower rotational speeds ($\omega \leq 40$ RPM). However, for $T_H = 50$°C, the trends of these curves differ significantly. For $\tau \times \omega$, the results resemble those at 45°C for $\omega > 70$ RPM and those at 35°C for $\omega < 30$ RPM, with a transition between $30 < \omega < 70$ RPM. Moreover, the peak power is observed at a higher rotational speed (≈87.3 RPM.)

The results shown in Fig.5.9 can be attributed to the impact of the warm fluid temperature on the MM specific magnetization. Fig.5.10 illustrates the specific magnetization of Gd as a function of temperature for different magnetic flux densities.

First, as T_H increases, the temperature of the Gd rises away from the magnetic phase transition temperature (around 293 K) entering the paramagnetic phase. This leads to a

Figure 5.9 – Influence of the warm fluid temperature on the TMM performance for the two-magnetic-volumes configuration, at fixed cold fluid temperature of 5°C and flow rate of 10 LPM/nozzle: (a) $\tau \times \omega$; (b) $\dot{W}_{prod} \times \omega$; (c) maximum measured rotational speed; (d) maximum torque from measurement or extrapolation.

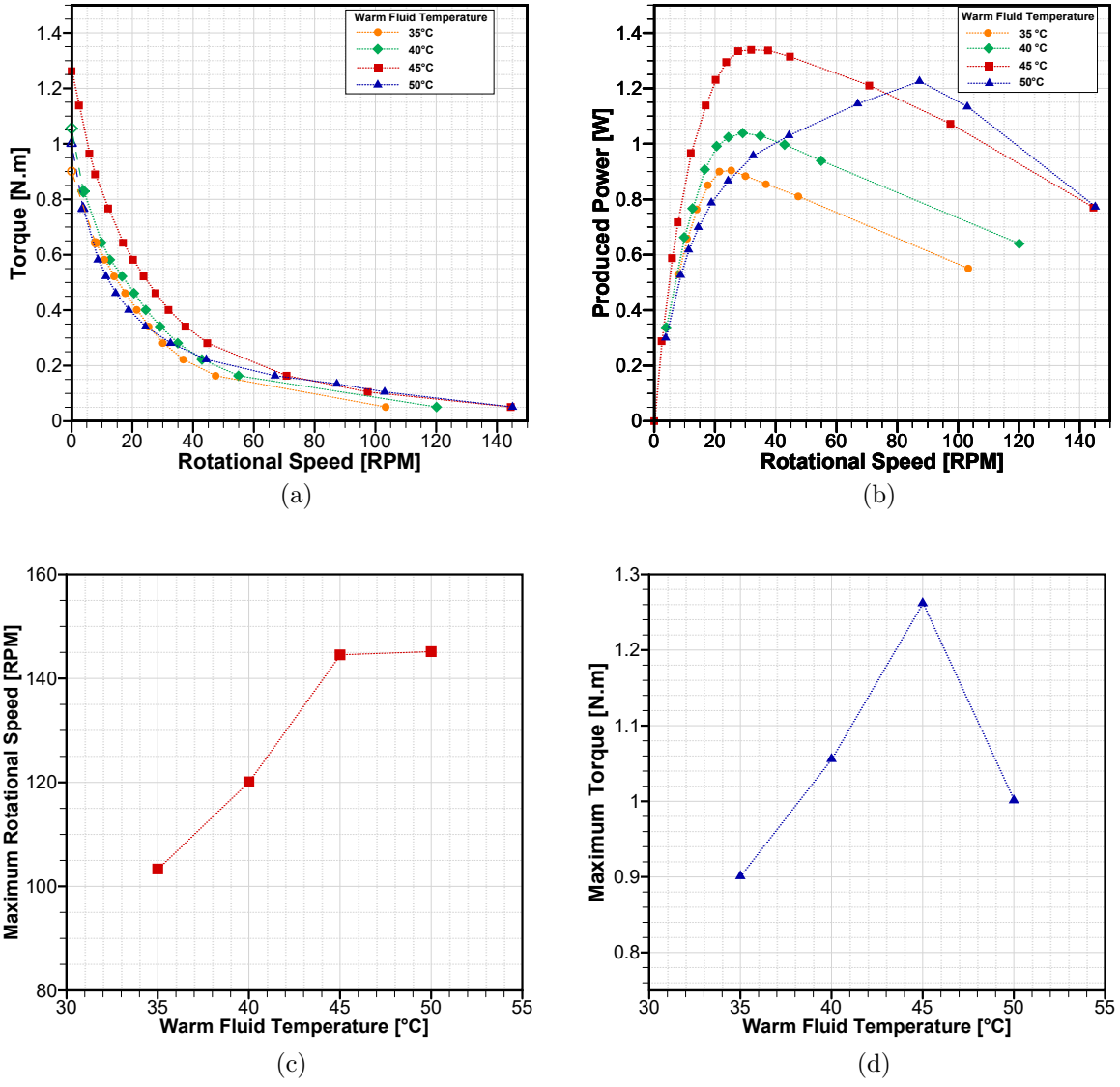

Figure 5.10 – Gadolinium specific magnetization as a function of temperature, obtained through the Weiss-Debey-Sommerfeld theory (MORRISH, 2001).

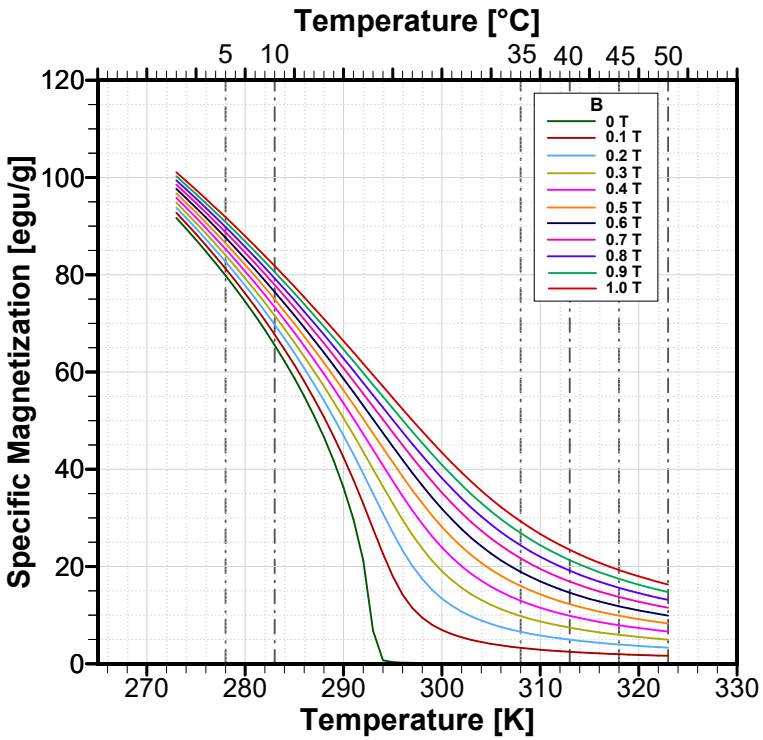

reduction in magnetization and magnetic force values, especially at high flux densities. This effect is further amplified by the enhanced heat transfer rate at higher temperatures, as evidenced by the Nusselt numbers in Tab. 4.5. This is beneficial to the net magnetic force balance between the fins in the ferromagnetic and paramagnetic phases, up to the condition of $T_H = 45°C$. As the rotor motion experiences lower resistance due to the reduction on magnetization at high flux densities, it is able to achieve higher maximum rotational speeds and torques, as in Fig. 5.9c and Fig. 5.9d, respectively. As discussed in Section 2.3.3, the heating process occurs when the MM is in the high-field region, while cooling takes place in the low-field region.

Nevertheless, the cold fluid temperature is fixed at 5.0°C, and under this condition, the heat transfer of the cold blow is less effective compared to the warm fluid blow. As T_H increases to 50°C, the Gd temperature moves even further away from the transition temperature. Due to insufficient cooling rates and the further reduction in motion resistance resulting from decreased magnetization, the proper establishment of the ferromagnetic phase is prevented. Consequently, the MM fins may undergo a thermal cycle at higher average temperatures after the heating and cooling processes, moving further away from the cold reservoir temperature.[1]

[1] The specific heat capacity of Gd is higher at lower magnetic flux densities and temperatures below the magnetic phase transition. This also affects the heat transfer in the cold stream region. Although this effect is well known, it possibly plays a secondary role in the proposed explanation, which focuses on specific magnetization in order to keep it as simple as possible.

As a result, no improvement is observed when comparing the results for 45.0°C and 50.0°C in terms of maximum rotational speed. This is because, at high rotor speeds, the average temperatures after the heating and cooling processes are, to some extent, similar around the transition temperature, regardless of T_H. However, as the imposed load on the shaft increases, reducing ω, the more effective heat transfer from the warm stream starts to make a noticeable difference, raising the average temperature after the heating process. Meanwhile, the poorer heat transfer from the cold stream is insufficient to achieve lower temperatures. Consequently, the rotor becomes unable to sustain high ω under elevated load conditions, leading to a reduction in torque (as observed at $\omega < 70$ RPM) and a shift in the point at which peak power is observed. Lastly, this also affects the maximum torque, which is lower compared to the 45.0°C condition.

The influence of the cold stream temperature on the TMM performance was evaluated by testing two cold temperatures (5.0°C and 10.0°C) in combination with two warm temperatures (45.0°C and 50.0°C). As observed in Fig 5.10, the gadolinium specific magnetization at 10°C is considerably lower than at 5°C, reducing the net magnetic force difference between the fins in the ferromagnetic and paramagnetic phases. Therefore, it is expected that increasing the cold stream temperature to 10°C reduces the maximum rotational speed, produced power and torque for both warm fluid temperatures, as shown in Fig. 5.11. Hence, operating this prototype, with Gd fins rotor, at temperatures above 5°C offers no advantage under any of the tested conditions.

It is observed that the influence of the cold fluid temperature on the performance parameters is more pronounced at $T_H = 45.0$°C (Fig. 5.11a and 5.11b) than at $T_H = 50.0$°C (Fig. 5.11c and 5.11d). Also notice that the $\tau \times \omega$ and $\dot{W}_{prod} \times \omega$ curves for $T_C = 10.0$°C and $T_H = 45.0$°C (Fig. 5.11a and 5.11b) are very similar to those for $T_H = 50.0$°C (Fig. 5.11c and 5.11d). As previously explained, this can be attributed to insufficient cooling rates and the improper establishment of the ferromagnetic phase, which leads to higher average temperatures after the heating and cooling processes. Thus, at 50.0°C, the performance becomes less sensitive to T_C. Therefore, the results in Fig. 5.11 also supports the proposed explanation.

Finally, the most suitable heat sink and source temperature conditions for the current version of the prototype are $T_C = 5.0$°C and $T_H = 45.0$°C, resulting in a temperature difference of 40.0°C. In relation to the Gd transition temperature, the heat sink is at a ΔT of 15°C lower, while the heat source is at a ΔT of 25°C higher. Although the prototype's performance may improve by reducing T_C, for the TMM to operate properly, it is expected that T_H must be increased simultaneously to maintain a non-balanced temperature difference with respect to the transition temperature.

Figure 5.11 – Influence of cold and warm fluid temperature on the TMM performance, at a fixed flow rate of 10 LPM/nozzle: (a) $\tau \times \omega$ at $T_H = 45.0°C$; (b) $\dot{W}_{prod} \times \omega$ at $T_H = 45.0°C$; (c) $\tau \times \omega$ at $T_H = 50.0°C$; (d) $\dot{W}_{prod} \times \omega$ at $T_H = 50.0°C$.

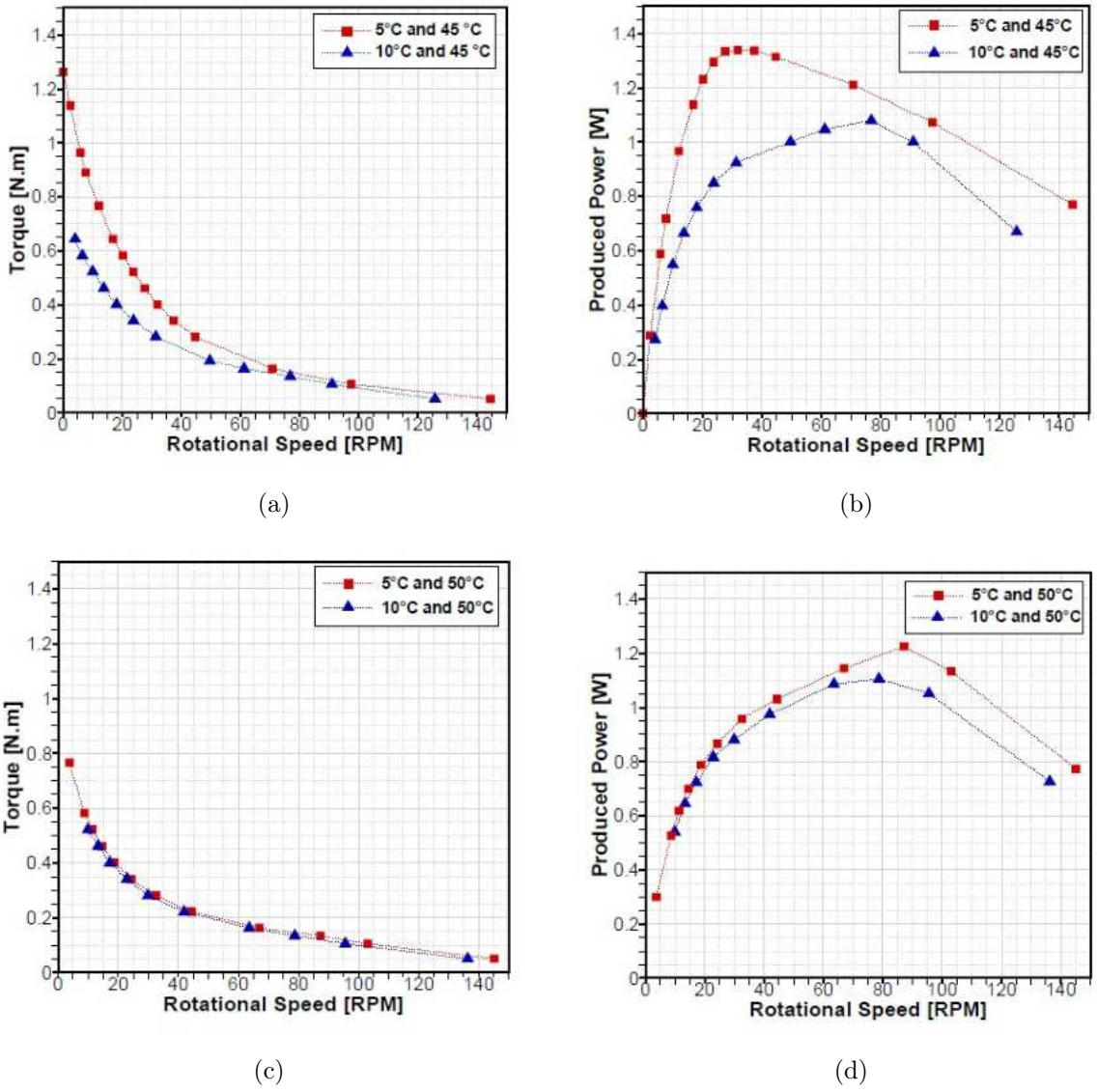

5.4.2 INFLUENCE OF THE FLOW RATE

The influence of the flow rate on the TMM performance was evaluated for both the two- and four-magnetic-volumes configurations. The cold sink and heat source temperatures are fixed at 5°C and 45°C, respectively. The performance curves, $\tau \times \omega$ and $\dot{W}_{prod} \times \omega$, are shown in Fig. 5.12 for the two-magnetic-volumes configuration and in Fig 5.13 for the four-magnetic-volumes configuration. In the $\dot{W}_{prod} \times \omega$ curves (Fig 5.12b and Fig 5.13b), the isotorque lines are included to facilitate the comparisons of the results.

At higher rotational speeds, an increase in flow rate results in greater power and torque outputs for both configurations. This behavior is attributed to enhanced heat transfer at higher Reynolds numbers (as shown in Fig. 4.22a and Fig. 4.22b), along with the increased thermal capacity of the working fluid. As a result, the gadolinium fins experience more

Figure 5.12 – Influence of the flow rate on the TMM performance for the two-magnetic volume configuration. The cold and warm temperatures are fixed at 5°C and 45°C, respectively: (a) $\tau \times \omega$; (b) $\dot{W}_{prod} \times \omega$, including the isotorque lines.

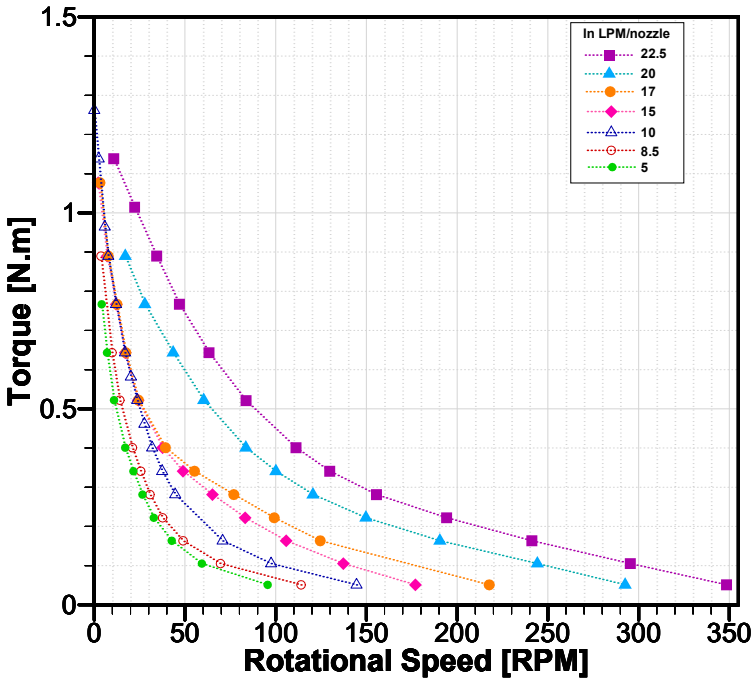

(a)

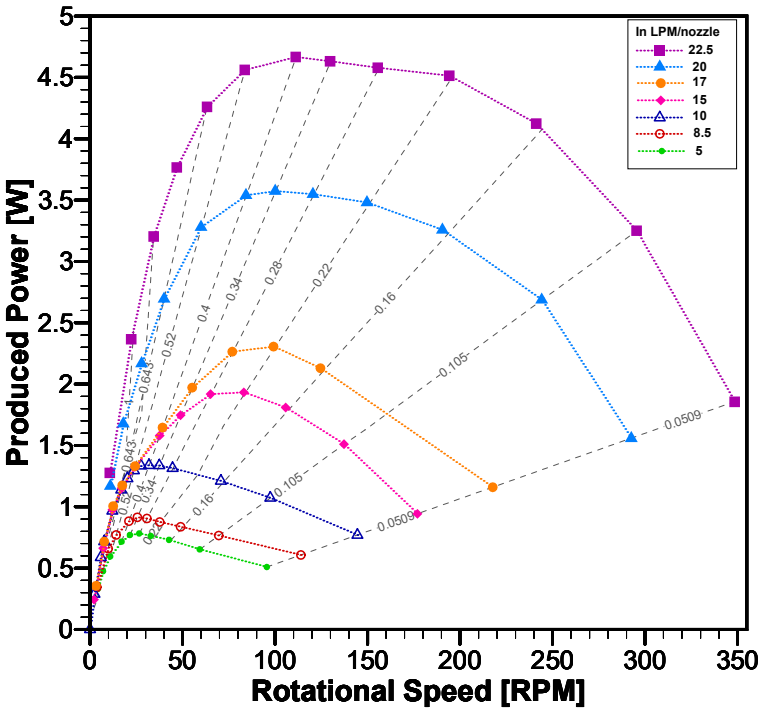

(b)

Figure 5.13 – Influence of the flow rate on the TMM performance for the four-magnetic volume configuration. The cold and warm temperatures are fixed at 5°C and 45°C, respectively: (a) $\tau \times \omega$; (b) $\dot{W}_{prod} \times \omega$, including the isotorque lines.

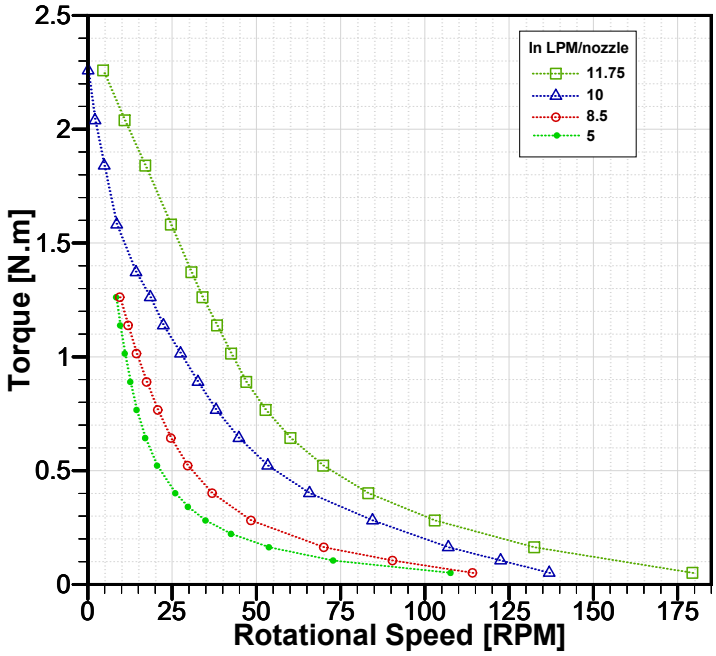

(a)

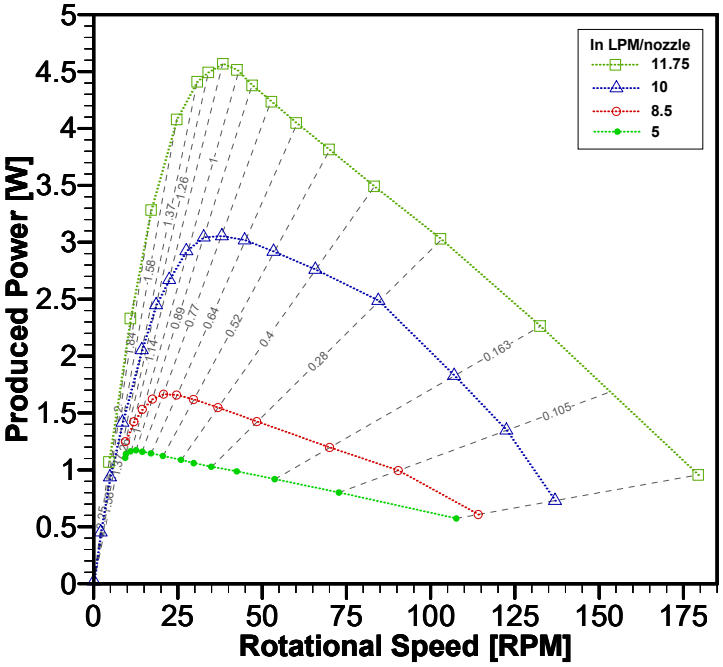

(b)

rapid temperature changes, consequently, accelerating the magnetic phase transitions, and thereby increasing the rotor speed and the produced power.

In Fig. 5.12, there are two significant performance improvements with increased flow rates that deserve attention. The first occurs between 8.5 and 10 LPM/nozzle, where a relatively small increase of 1.5 LPM/nozzle leads to a notable rise in torque and generated power. This improvement is attributed to the gadolinium fins crossing the transition temperature into the ferromagnetic phase, thereby substantially enhancing the magnetic force.

The second improvement is observed between 17 and 20 LPM/nozzle. In this range, a 3 LPM/nozzle increase again yields a marked performance gain. This is attributed to a significant enhancement in the heat transfer rates within that range, as evidenced by the marked rise in Nusselt number shown in Fig. 4.22b. Nevertheless, a more precise understanding of the underlying phenomena, requires numerical simulations that couple the heat transfer and the thermomagnetic properties.

When comparing the results at the same rotational speed, a more rapid temperature change due to the higher flow rate causes the fins' temperatures to deviate further from the transition temperature.This increases the magnetic force imbalance between the ferromagnetic and paramagnetic fins and, as a result, enhances the resulting torque. As the imposed load increases and the rotational velocity approaches zero, regardless of the set flow rate, the rotor delivers a non-continuous rotation. In this condition, the Gd fins are exposed to the warm and cold fluid streams for longer durations, allowing them to approach thermal equilibrium with the respective reservoirs. As a result, the maximum torque converges to a single value, independent of the flow rate.

Therefore, it can be concluded that the maximum torque is a function of the MM mass, the magnetic flux gradient and the temperatures of the heat sink and source, but it is independent of the flow rate. Comparing the maximum torque values for the two- and the four-magnetic field volume configurations, the former achieved ≈ 1.26 N·m, while the latter reached ≈ 2.30 N·m. This indicates that, under the same magnetic field gradients and temperature conditions, doubling the MM active mass results in a proportional increase in maximum torque, within the bounds of measurement uncertainty.

Conversely, the maximum rotational speed (under no-load conditions) is linearly proportional to the flow rate. Fig. 5.14 shows the maximum measured rotational velocity at zero load condition as a function of the flow rate. This figure comprises the results for both two- and four-magnetic field volumes. However, this linear dependency is expected to hold only up to a certain limiting flow rate value. Beyond this point, the thermal capacity of the flow becomes sufficiently large for the Gd fins to approach thermal equilibrium with the reservoirs, even though the rotor operates continuously at high ω. This will likely cause the system to reach a maximum achievable rotational speed.

Figure 5.14 – Maximum measured rotational velocity, at no-load condition, as a function of the flow rate. The cold and warm temperatures are fixed at 5°C and 45°C, respectively. The results were obtained for two-magnetic field volumes (squares) and four-magnetic field volumes (triangles).

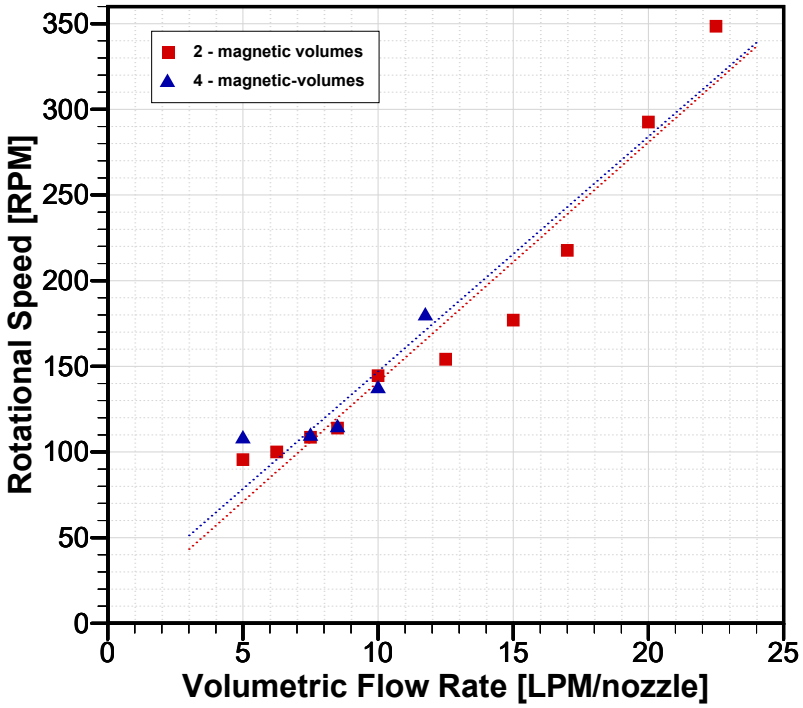

Within the tested flow rate range, the highest supplied flow rate of 22.5 LPM/nozzle is still insufficient to allow the fins to reach thermal equilibrium during continuous high-speed operation. The maximum measured rotational speed, under no-load conditions, for the two- and four-magnetic field volumes configurations are, respectively, 348.5 RPM at 22.5 LPM/nozzle, and 179.4 RPM at 11.75 LPM/nozzle. In terms of the peak produced power, 4.67 W at 22.5 LPM/nozzle was measured for the two-magnetic field volumes; and 4.57 W at 11.75 LPM/nozzle for the four-magnetic field volumes.

To further assess the influence of the flow rate on the peak produced power, the dimensionless parameter, denoted as $\dot{W}^*$, is introduced. As defined in Eq. 5.1, $\dot{W}^*$ represents the ratio of the maximum power output at a given flow rate ($\dot{W}_{max}$) to the maximum power achieved at the reference (lowest) flow rate ($\dot{W}^R_{max}$):

$$\dot{W}^* = \frac{\dot{W}_{max}}{\dot{W}^R_{max}} \tag{5.1}$$

In this way, when the flow rate is two, three, or four times greater than the lowest flow rate, $\dot{W}^*$ indicates how the maximum power output scales accordingly. Fig. 5.15 shows the results for different reference flow rates for the two-magnetic field volumes configuration, with the cold and warm stream temperatures are 5°C and 45°C, respectively. The

Figure 5.15 – Dimensionless parameter ($\dot{W}^*$) as a function of the flow rate for the two-magnetic field volumes configuration, with the cold and warm stream temperatures at 5°C and 45°C, respectively: (a) $\dot{W}^R_{max} = 0.82$ W; (b) $\dot{W}^R_{max} = 0.91$ W; (c) $\dot{W}^R_{max} = 0.84$ W; (d) $\dot{W}^R_{max} = 0.78$ W.

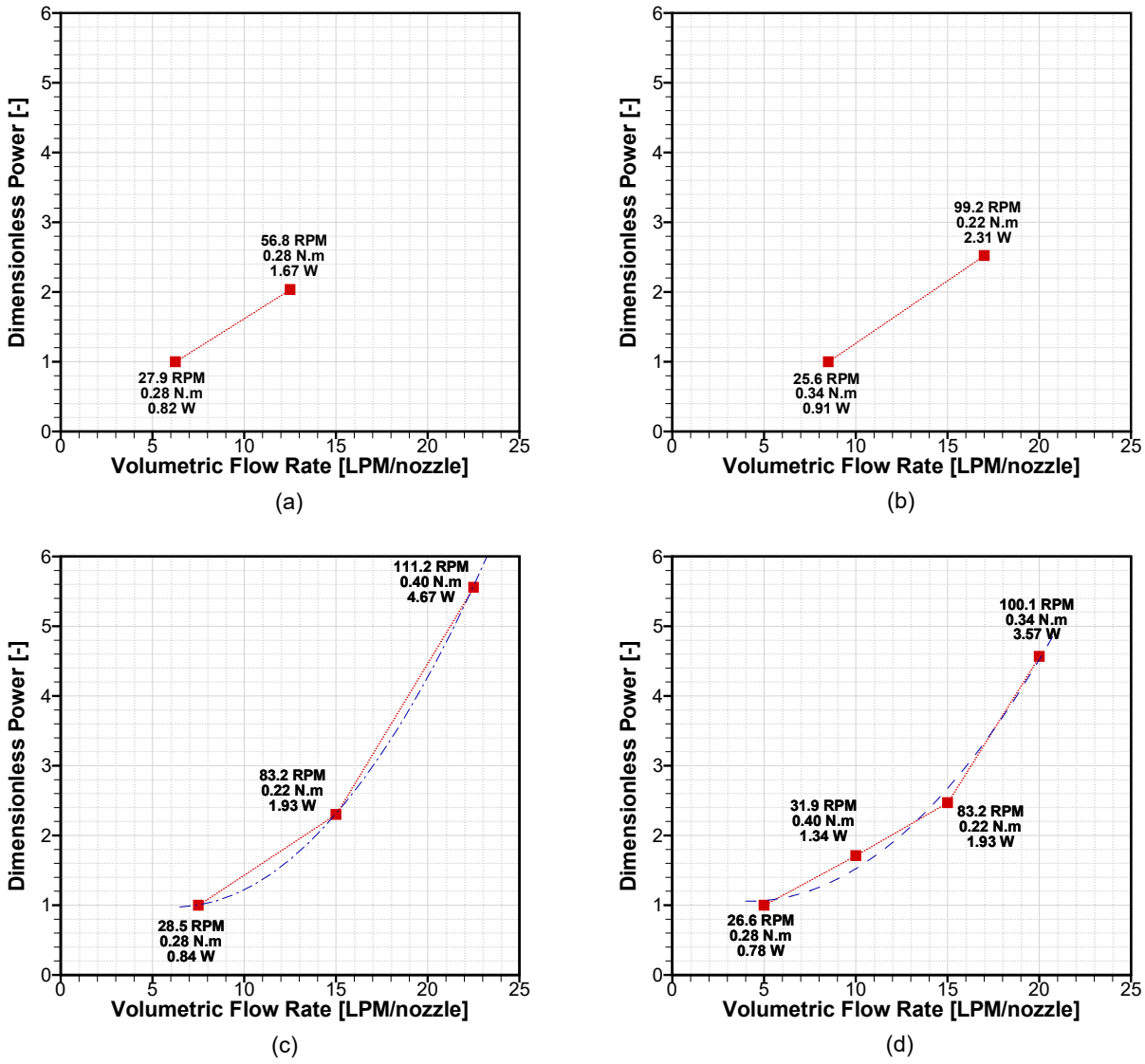

corresponding reference $\dot{W}^R_{max}$ values are provided in Table 5.1.

The results in Fig. 5.15 include the corresponding rotational speed, torque, and power value. Fig. 5.15a and 5.15b allow for comparison when the flow rates is twice the reference value given in Table 5.1, while Fig. 5.15c corresponds to a flow rate three times the reference, and Fig. 5.15d to four times the reference value. In all cases, doubling the flow rate led to an approximately twofold increase in produced power. For the cases with more data points (Fig.5.15c and 5.15d), a quadratic relationship between produced power and flow rate is observed. The most significant relative increase, by a factor of 5.6, occurred when the flow rate was tripled from 7.5 to 22.5LPM/nozzle. This substantial improvement

Table 5.1 – Reference $\dot{W}^R_{max}$ values for their corresponding flow rates and associated data in Fig. 5.15

$\dot{\vartheta}_{min}$ [LPM/nozzle]	$\dot{W}^R_{max}$ [W]	Fig.
5	0.78	d
6.25	0.82	a
7.5	0.84	c
8.5	0.91	b

is attributed to the enhanced heat transfer rates and increased thermal capacity of the working fluid, as indicated by the increase in the Nusselt number shown in Fig. 4.22b.

5.4.3 INFLUENCE OF THE MAGNETIC VOLUMES NUMBER

The number of magnetic volumes in a TMM is directly associated with the active mass of MM at its ferromagnetic and paramagnetic phases, thereby influencing the magnetic force balance. Multiple tests were performed under the same operating conditions of heat sink and source temperatures (fixed at 5°C and 45°C, respectively) and warm and cold flow rates. These tests were conducted for both two- and four-magnetic-volume configurations, enabling the assessment of the impact of magnetic volume number on the motor's performance.

The performance curves, $\tau \times \omega$ and $\dot{W}_{prod} \times \omega$, are presented in Fig. 5.16 and Fig. 5.17, respectively. The results were obtained for the same flow rates of 5, 7.5, 8.5 and 10 LPM/nozzle. It is evident that the increase in the number of magnetic volumes results in higher torque and produced power values, regardless of the flow rate.

In terms of torque measurements, the differences become more pronounced as the rotational speed decreases. Increasing the number of magnetic volumes, and consequently, the active mass of MM at the ferromagnetic phase, enhance the motor's magnetic force and torque. Nonetheless, the net increase in the magnetic force, and consequently in the produced torque, is more significant as the temperature of the Gd fins approaches thermal equilibrium with the thermal reservoirs. This occurs as the fins move further from T_T, completing their transition into the ferromagnetic and paramagnetic phases. As previously discussed in Section 5.4.2, this condition tends to be achieved at lower rotational speeds. The largest difference on the maximum torque values are 1.26 N·m for the two-magnetic-volumes configuration, compared to 2.26 N·m for the four-magnetic field volumes configuration (Fig. 5.16d).

As the produced power is a function of torque (Eq. 4.9), the four-magnetic field volumes configuration demonstrates a significant performance improvement as shown in Fig. 5.17. This increasing in $\dot{W}_{prod}$ becomes more pronounced as the flow rate increases. At a flow rate of 10 LPM/nozzle (Fig 5.17d), the power output rises from 1.34 W in the two-magnetic-volume configuration to 3.05 W in the four-magnetic one.

Figure 5.16 – Influence of the number of magnetic volumes on the TMM torque at the same flow rate per nozzle. The cold and warm temperatures are fixed at 5°C and 45°C, respectively.

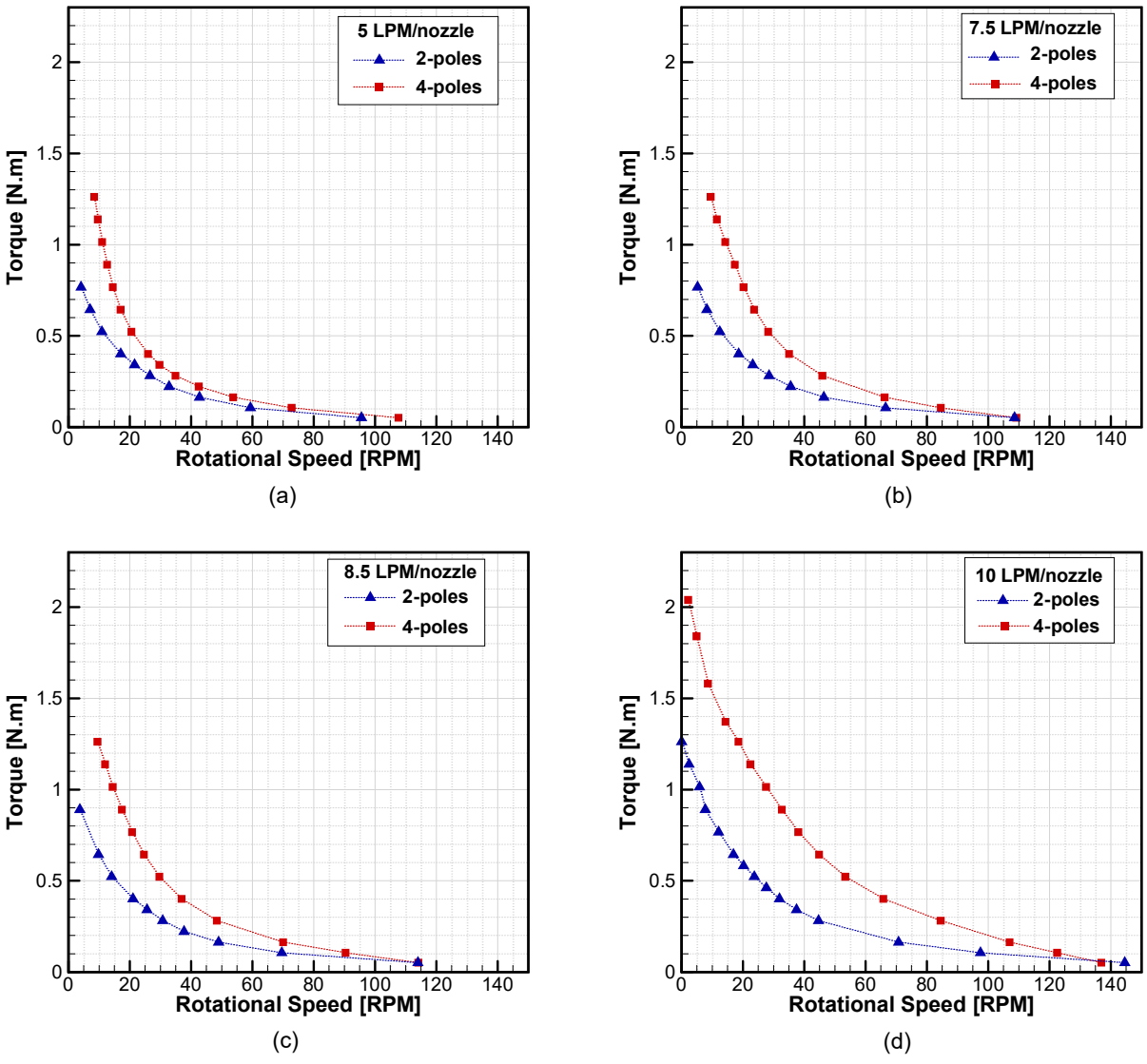

Figure 5.17 – Influence of the number of magnetic volumes on the TMM produced power at the same flow rate per nozzle. The cold and warm temperatures are fixed at 5°C and 45°C, respectively.

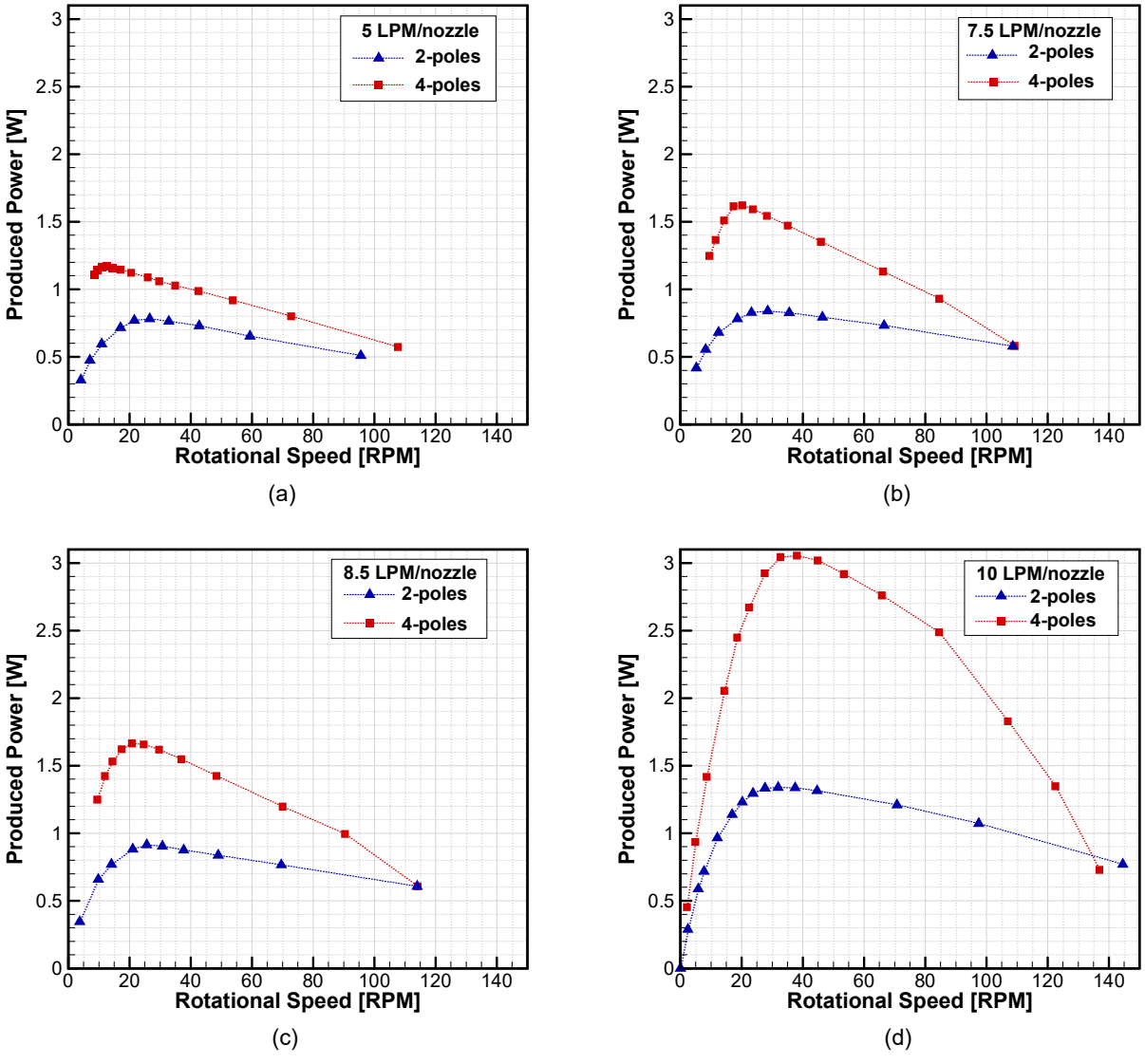

Table 5.2 – Maximum produced power and pressure drop values for the operating conditions corresponding to the best $\dot{W}_{prod} \times \omega$ curves for the two- and four-magnetic field volumes configurations, shown in Fig. 5.18.

Configuration	$\dot{\vartheta}$ [LPM/nozzle]	$\dot{W}_{max}$ [W]	ΔP [kPa]	Fig. 5.18
2-pole	22.5	4.67	77.8	a
4-pole	11.75	4.57	32.15	a
2-pole	20	3.57	59.6	b
4-pole	10	3.05	23.6	b

However,the presence of multiple magnetic field regions also increases the MM mass in the non-magnetic phase, which diminishes overall benefit, as the fins in the paramagnetic phase introduce more resistance to rotor movement. This effect becomes more pronounced at higher rotational speeds, where the average temperatures after the heating and cooling processes tend to remain closer to the transition temperature, limiting the extent of phase transition. As a result, no improvement in the maximum rotational speed under no-load conditions is observed when comparing the two- and four-magnetic field volume configurations, as can be seen in the $\dot{W}_{prod} \times \omega$ curves shown in Fig. 5.17. This discussion is further supported by Fig. 5.14, which shows that the maximum rotational speed exhibits a linear dependence on the flow rate. The linear fittings for the two- and four-magnetic field volume configurations are very similar, indicating that increasing the number of magnetic volumes has minimal effect on the no-load rotational speed.

Lastly, it is important to compare the best $\dot{W}_{prod} \times \omega$ curves for the two- and four-magnetic field volumes configurations, as in Fig. 5.18. In Fig. 5.18a, the curve for the two-magnetic volume at a flow rate of 22.5 LPM/nozzle is compared with that of the four-magnetic volume at 11.75 LPM/nozzle. Under these conditions, each configuration achieved its highest produced power, and the power outputs have very similar values, of about 4.5 W. Additional important results are presented in Fig. 5.18b, where the flow rates are 20 LPM/nozzle and 10 LPM/nozzle, respectively, for the two- and the four-magnetic-volume configurations.

A distinct difference in the shape of the $\dot{W}_{prod} \times \omega$ curves can be observed. For the four-volume configuration, a sharp peak appears at a lower rotational speed (< 50 RPM), whereas in the two-volume configuration, the maximum power is sustained across a broader range of rotational speeds and torque values, specifically within the range $100 < \omega < 200$ RPM. This difference can be mainly attributed to the higher flow rate per nozzle used in the two-volume case. It is possible that operating the four-volume configuration at the same flow rate would also result in a similar plateau, but at a higher produced power. This behavior can be advantageous for TMM operation, as it allows for maintaining consistent power output while adjusting torque and rotational speed according to the demands of a specific application.

Figure 5.18 – Comparison of the best $\dot{W}_{prod} \times \omega$ curves for the two- and four-magnetic field volumes configurations. The cold and warm temperatures are fixed at 5°C and 45°C, respectively. The flow rates are: (a) 22.5 LPM/nozzle for the two-volume configuration and 11.75 LPM/nozzle for the four-volume configuration; (b) 20 LPM/nozzle for the two-volume configuration and 10 LPM/nozzle for the four-volume configuration.

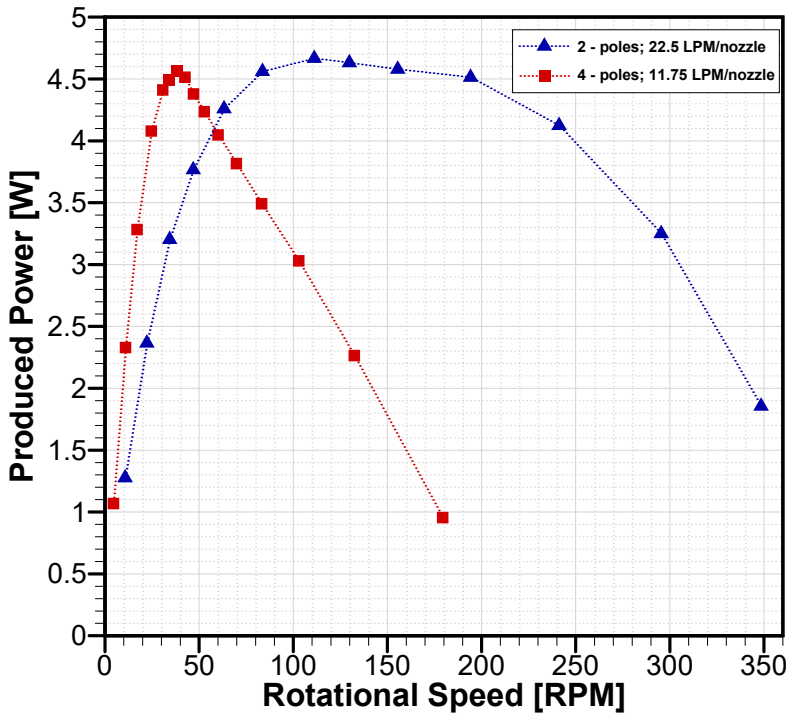

(a)

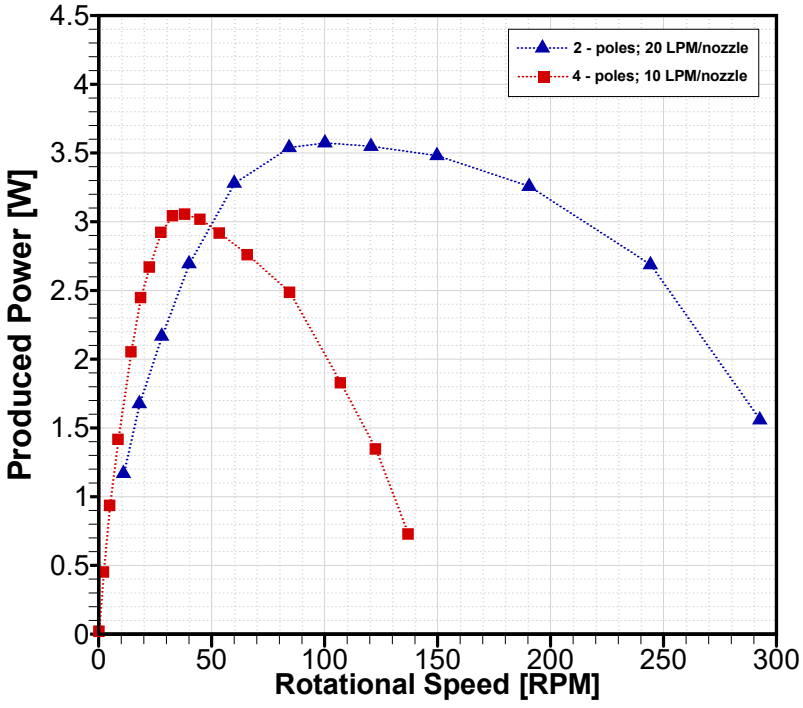

(b)

The maximum produced powers for the operating conditions corresponding to the best $\dot{W}_{prod} \times \omega$ curves for the two- and four-magnetic field volumes configurations, shown in Fig. 5.18, are presented in Table 5.2. Although approximately the same peak produced power values can be achieved using different numbers of magnetic volumes by adjusting the operating flow rate, the associated viscous losses must also be considered.

Table 5.2 also presents the average pressure drop measured in the fluid distribution system. It can be noted that, for similar produced powers, the four-magnetic-volume configuration exhibits lower pressure drops compared to the two-volume configuration. For energy harvesting applications, where the input heat is recovered from heat wastes, the pumping power is effectively the only external power input required. In such cases, it is essential that thermomagnetic motors present minimal viscous losses. Consequently, the back work ratio[2] becomes a more appropriate metric for the design and optimization of thermomagnetic motors, as previously proposed by Corrêa et al. (2023). Therefore, increasing the number of high magnetic field regions, along with the active mass of the magnetic material, appears to be the most effective strategy to both enhance produced power and reduce pumping power requirements, and thus minimizing the back work ratio.

[2] The back work ratio (BWR) is defined as the ratio between the pumping power and the total produced power. In this way, an optimized thermomagnetic motor should have BWR values tending to zero.

6 CONCLUSIONS

6.1 FINAL CONSIDERATIONS

The work presented in this master's thesis dealt with the design, production (*in-house*), and experimental characterization of a novel rotary thermomagnetic motor (TMM) prototype for energy harvesting applications. In alignment with the specific objectives of this study, a patent of the prototype's design was successfully filed with the Brazilian Patent and Trademark Office (*INPI*) under application number BR1020240254597.

The prototype is mainly composed of a magnetic circuit (MC), a magnetocaloric material (MM) rotor, and a transmission system. The MC is stationary and generates its magnetic field using high-BH energy permanent magnets. In addition, its geometry enables the TMM to operate in either a two or four magnetic field volumes configuration. The MM rotor consists of a non-magnetic material disc with radially arranged MM fins attached to its lower surface. Converging channels for the working fluid flow are formed between adjacent fins. Additionally, a fluid treatment station that conditions and distributes the working fluid was used to supply the warm and cold fluid flow streams to specific regions of the rotor. Divergent nozzles were designed to fill, simultaneously, the four channels formed among three adjacent fins, increasing the MM active mass. This kind of rotary TMM offers some advantages when compared with reciprocating devices, as well as to other designs of rotary prototypes, such as the use of continuous fluid streams, which eliminates the need for control valves and facilitates the attainment of continuous motion at high frequencies.

The designed MC reached the expected magnetic field intensity of 1.0 T, with a peak value of 1.03 T, according to the numerical results. Following its production and assembly, the experimental characterization showed a peak intensity of 1.06 T, corresponding to a maximum deviation of about 0.029 T from the numerical results. The good agreement between the experimental and the simulated values attest to the reliability of the design, production, and assembly methodologies employed.

A proof-of-concept demonstration was fundamental to confirm that reactive forces from the fluid flow do not influence the rotor's motion. To this end, a test was performed using only warm fluid streams in all nozzles. In this condition, only the paramagnetic phase is established, which minimizes the magnetic forces and allows the rotor to spin freely. As expected, the rotor remained stationary throughout the test. Subsequently, warm and cold streams were supplied and the rotor spun continuously. These results demonstrate that the motion is solely due to the imbalance of magnetic forces, with no contribution from flow forces.

The performance of the TMM prototype was evaluated through measurements of torque (τ) and the resulting rotational speed (ω) under various operating conditions, including different stream temperatures (warm and cold) and flow rates. The produced power ($\dot{W}_{prod}$) is an indirect result of these measured parameters. In this context, the performance tests were evaluated and compared using of two different curves: torque as a function of the rotational speed ($\tau \times \omega$) and power as a function of the rotational speed ($\dot{W}_{prod} \times \omega$). These curves were obtained for both the two-magnetic-volumes and the four-magnetic-volumes setups.

The rotor exhibited the desired continuous and smooth rotation under most of the operating conditions tested, thereby fulfilling one of the specific objectives of this work. Exceptions were observed at the lowest flow rates and in tests with elevated load inputs. Under these conditions, the rotor showed some oscillations in the direction of motion and a non-continuous rotation. However, in all tests, a net displacement was observed in the correct clockwise direction.

The results for varying warm stream temperatures (T_H) corroborated the expectation that, up to a threshold of 45°C, an increase in T_H leads to higher ω, τ and consequently, $\dot{W}_{prod}$ values. Higher T_H results in reduced magnetization of the Gd fins, as well as enhanced heat transfer, as indicated by increased Nusselt numbers (Nu). As a result, the resistance to motion is reduced, increasing the motor's net magnetic force and, consequently, its torque and rotational speed. However, since the heat sink temperature (T_C) was fixed in 5°C, the cooling rate of the fins became insufficient when T_H was increased to 50°C. Consequently, no further improvement in the maximum rotational speed is observed. Additionally, the limited cooling capacity increases the resistance to motion, shifting the thermal cycle of the Gd fins to higher average temperatures. As a result, the net magnetic force is reduced and the rotor is unable to sustain high ω under elevated load inputs, which reduces the maximum achievable torque and shifts the rotational speed at which the peak produced power is observed.

In terms of the heat sink temperature variation, no advantage was observed by increasing T_C from 5°C to 10°C. The gadolinium magnetization is significantly lower at 10°C, reducing the net magnetic force and, thereby, the torque and resulting rotational speed. Hence, the most suitable heat sink and source temperature conditions for the current version of the prototype are $T_H = 45$°C and $T_C = 5$°C.

Regarding the influence of the fluid flow rate, the results showed that, under low load conditions, thereby high rotational speeds, increasing the flow rate led to higher values of ω and $\dot{W}_{prod}$. Higher flow rates and, thus, Reynolds numbers (Re) are associated with enhanced heat transfer and increased thermal capacity of the working fluid. As a result, the Gd fins' temperature varies more rapidly, accelerating the magnetic phase transitions and increasing the rotor's speed. The maximum rotational velocity (under no-load conditions)

exhibits a linear trend with the flow rate.

In contrast, under higher load inputs, the rotor began to operate discontinuously and at a lower speed. In this scenario, the Gd fins remained exposed to the working fluid for longer periods, approaching thermal equilibrium with the heat source and sink. Consequently, the torque values tended to converge, making the maximum torque independent of the flow rate.

Comparing the $\tau \times \omega$ and $\dot{W}_{prod} \times \omega$ curves for the two- and four-magnetic volumes configurations, the results showed that increasing the number of magnetic volumes and, thus, the active MM mass at the ferromagnetic state, led to an increase in the motor's torque output. This is more pronounced at lower ω, when the Gd fins' temperatures approach thermal equilibrium with the heat source and sink, moving away from T_T and completing their transitions into the paramagnetic and ferromagnetic phases. The maximum (holding) torque value duplicates, within the experimental uncertainty range, when the number of magnetic volumes goes from two to four.

On the other hand, more magnetic volumes also imply an increased mass of MM in the paramagnetic state, which reduces the benefit generated by the increasement of those in the ferromagnetic state. This reduction is more evident under higher ω, in which the fins' thermal cycle occurs at temperatures closer to T_T. Therefore, the increase in the number of magnetic volumes did not result in any significant enhancements to the maximum rotational speeds achieved by the rotor.

The same power output peak was achieved for different numbers of magnetic volumes by adjusting the fluid streams flow rates. Nevertheless, a higher number of these volumes reduced the system's viscous losses. Therefore, increasing magnetic volumes numbers is more advantageous because it reduces the system's pumping power. However, at the highest flow rates (over 20 LPM/nozzle) and two-magnetic volumes configuration, the maximum power is sustained across a wide range of rotational speeds and torque values. This result indicates an advantage of TMM operation, as it allows for maintaining consistent power output while adjusting torque and rotational speed according to the demands of a specific application.

Finally, the maximum values of the performance parameters obtained for each configuration were as follows: a maximum rotational speed of 348.5 RPM, a peak produced power of 4.67 W, and a holding torque of 1.3 N·m for the two-magnetic volume configuration at a flow rate of 22.5 LPM/nozzle; and 179.4 RPM, 4.57 W and 2.3 N·m for the four-magnetic-volume configuration at a flow rate of 11.75 LPM/nozzle. These results surpass the current state-of-the-art values of 242 RPM (MEHMOOD et al., 2021), 3.7 W (TAKAHASHI et al., 2006) and 1.3 N·m(FRANZITTA et al., 2013). These results exceeded initial expectations and successfully met both the specific and primary objectives of this master's thesis.

6.2 RECOMMENDATIONS FOR FUTURE WORKS

Based on the advances presented in this master's thesis, some recommendations for future works is listed as follows:

1. Use thinner plates for the Gd fins, in order to reduce the thermal mass of the magnetocaloric material and, consequently, enable faster magnetic phase transitions. However, this modification comes at the cost of a reduced net magnetic force. Thus, an optimal design trade-off must be achieved to enhance overall prototype performance, which may include incorporating a greater number of fins.

2. Use different MM geometries to enhance its heat transfer with the working fluid and promote faster magnetic phase transition.

3. Perform experimental tests with T_C lower than 5°C to evaluate. However, to ensure TMM proper operation, T_H should be simultaneously increased to maintain a non-balanced temperature difference with respect to T_T.

4. Perform experimental tests using uneven flow rates between the warm and cold fluid streams. Since Nusselt number values increase at higher temperatures, performance can potentially be improved by employing higher flow rates in the cold fluid stream.

5. Use first-order magnetocaloric materials, ideally with a T_T above ambient temperature.

6. Scale up the prototype by simultaneously assembling multiple MC and MM rotor sets onto a single shaft, as proposed in the filed patent.

Bibliography

AVIROVIK, D.; KISHORE, R.; VUCKOVIC, D.; PRIYA, S. Miniature shape memory alloy heat engine for powering wireless sensor nodes. *Energy Harvesting and Systems*, Walter de Gruyter GmbH, v. 1, n. 1-2, p. 13–18, 2014. ISSN 2329-8774.

BAHL, C. R.; ENGELBRECHT, K.; GIDEON, A.; LEVY, M. A. V.; MARCUSSEN, J. B.; IMBAQUINGO, C.; BJØRK, R. Design, optimization and operation of a high power thermomagnetic harvester. *Applied Energy*, Elsevier, v. 376, p. 124304, 2024.

BAKKER MAGNETS. 2024. Available at: <http://www.bakkermagnetics.com/>.

BESSA, C.; FERREIRA, L.; HORIKAWA, O.; GAMA, S. On the relevance of temperature, applied magnetic field and demagnetizing factor on the performance of thermomagnetic motors. *Applied Thermal Engineering*, v. 145, p. 245–250, 2018.

BJøRK, R.; BAHL, C.; SMITH, A.; PRYDS, N. Review and comparison of magnet designs for magnetic refrigeration. *International Journal of Refrigeration*, v. 33, n. 3, p. 437–448, 2010.

CERNOMAZU, D. *Thermo-magnetic motor*. 2008. RO127786A2.

CHOI, H. S.; HUR, S.; KUMAR, A.; SONG, H.; Min Baik, J.; SONG, H.-C.; RYU, J. Continuous pyroelectric energy generation with cyclic magnetic phase transition for low-grade thermal energy harvesting. *Applied Energy*, v. 344, p. 121271, 2023. ISSN 0306-2619.

CHRISTIAANSE, T.; BRÜCK, E. Proof-of-concept static thermomagnetic generator experimental device. *Metallurgical and Materials Transactions E*, Springer, v. 1, p. 36–40, 2014.

CHRISTIAANSE, T.; CAMPBELL, O.; TREVIZOLI, P.; MISRA, S.; ASTEN, D. van; ZHANG, L.; GOVINDAPPA, P.; NIKNIA, I.; TEYBER, R.; ROWE, A. A concise approach for building the diagram for mn–fe–p–si hysteretic magnetocaloric material. *Journal of Physics D: Applied Physics*, v. 50, n. 36, p. 365001, 2017.

COELHO, A. d. A. *Dispositivo termomagnético rotativo e uso do mesmo*. 2012. BR1020120128241B1.

COELHO, A. d. A. *Dispositivo termomagnético reciprocativo linear e uso do mesmo*. 2019. BR1020120128225A2.

COEY, J. Permanent magnet applications. *Journal of Magnetism and Magnetic Materials*, v. 248, 2002.

COEY, J. M. D. *Magnetism and Magnetic Materials*. Cambridge: Cambridge University Press, 2010. ISBN 9780521816144.

COMSOL Multiphysics ®. *AC/DC Module User's Guide*. 2024. <https://www.comsol.com/documentation>. V.6.2.

CORRêA, L. S.; ROWE, A.; TREVIZOLI, P. V. Thermodynamic optimization of a linear thermomagnetic motor. *Applied Thermal Engineering*, v. 219, p. 119344, 2023. ISSN 1359-4311.

CROAT, J. J.; HERBST, J. F.; LEE, R. W.; PINKERTON, F. E. High-energy product nd-fe-b permanent magnets. *Applied Physics Letters*, AIP Publishing, v. 44, n. 1, p. 148–149, 1984.

DAN'KOV, S. Y.; TISHIN, A. M.; PECHARSKY, V. K.; GSCHNEIDNER, K. A. Magnetic phase transitions and the magnetothermal properties of gadolinium. *Phys. Rev. B*, American Physical Society, v. 57, p. 3478–3490, Feb 1998.

de JESUS, V.; SANTOS, M.; SILVA, C.; CâMARA, M.; MICHEL, H.; BRAGA, C.; ROWE, A.; TREVIZOLI, P. Thermodynamic evaluation of thermomagnetic motors with first and second order transition magnetocaloric materials. *Applied Thermal Engineering*, v. 253, p. 123737, 2024. ISSN 1359-4311.

DÖRING, A. M.; REIF, D. D.; ROSA, M. A.; PEIXER, G. F.; MACCARI, F.; SKOKOV, K.; GUTFLEISCH, O.; WENDHAUSEN, P. A.; LOZANO, J. A.; JR, J. R. B. et al. Long-time aging of la (fe, si, mn) 13hz microparticles using different fluids for magnetic refrigeration systems. *Journal of Magnetism and Magnetic Materials*, Elsevier, v. 591, p. 171721, 2024.

DUAN, J.; FENG, G.; YU, B.; LI, J.; CHEN, M.; YANG, P.; FENG, J.; LIU, K.; ZHOU, J. Aqueous thermogalvanic cells with a high seebeck coefficient for low-grade heat harvest. *Nature communications*, Nature Publishing Group UK London, v. 9, n. 1, p. 5146, 2018.

DUPONT, M.; MACFARLANE, D.; PRINGLE, J. Thermo-electrochemical cells for waste heat harvesting–progress and perspectives. *Chemical communications*, Royal Society of Chemistry, v. 53, n. 47, p. 6288–6302, 2017.

EES. *Engineering Equation Solver (EES)*. [S.l.], 2024. Disponível em: <https://www.fchart.com/ees/>.

EVARISTO, E.; COLMAN, F.; ALVES, C.; TREVIZOLI, P. Mathematical modelling and simulation results of a linear thermomagnetic motor with gravity return. *Journal of Magnetism and Magnetic Materials*, v. 544, 2022.

FARIA, L. F. C. P. L. R. N. *Introdução ao Magnetismo dos Materiais*. [S.l.]: Livraria da Física, 2005.

FERNANDEZI, J. J. *Thermomagnetic motor*. 2019. ES2639624A2.

FIRTH, A.; ZHANG, B.; YANG, A. Quantification of global waste heat and its environmental effects. *Applied energy*, Elsevier, v. 235, p. 1314–1334, 2019.

FORMAN, C.; MURITALA, I. K.; PARDEMANN, R.; MEYER, B. Estimating the global waste heat potential. *Renewable and Sustainable Energy Reviews*, v. 57, p. 1568–1579, 2016.

FRANZITTA, V.; VIOLA, A.; TRAPANESE, M. Design and test of a thermomagnetic motor using a gadolinium rotor. *Applied Mechanics and Materials*, Trans Tech Publ, v. 432, p. 324–329, 2013.

FUERTHALLER, W. *Thermomagnetischer motor*. 1993. US4730137.

FURLANI, E. P. *Permanent Magnet and Electromechanical Devices: Materials, Analysis, and Applications*. San Diego: Academic Press, 2001. ISBN 9780122699515.

GAMA, S.; FERREIRA, L. D.; BESSA, C. V.; HORIKAWA, O.; COELHO, A. A.; GANDRA, F. C.; ARAUJO, R.; EGOLF, P. W. Analytic and experimental analysis of magnetic force equations. *IEEE Transactions on Magnetics*, IEEE, v. 52, n. 7, p. 1–4, 2016.

GEE, C. W. *Hybrid type power conversion system with materials showing a magnetocaloric effect(Gadolinium) in harnessing low-temperature differentials*. 2019. KR101940141B1.

GRIGORIJ, O. *Thermal magnetic step motor device*. 1995. RU2044159C1.

GRIGORIJ, O. *Thermomagnetic motor*. 1996. RU2067213C1.

GSCHNEIDNER, K. A.; PECHARSKY, V. K. Magnetocaloric materials. *Annual Review of Materials Science*, Annual Reviews, v. 30, n. 1, p. 387–429, 2000.

GUOHUA, X. *Thermomagnetic engine*. 2004. CN2641918Y.

GUTFLEISCH, O.; GOTTSCHALL, T.; FRIES, M.; BENKE, D.; RADULOV, I.; SKOKOV, K. P.; WENDE, H.; GRUNER, M.; ACET, M.; ENTEL, P. et al. Mastering hysteresis in magnetocaloric materials. *Philosophical Transactions of the Royal Society A: Mathematical, Physical and Engineering Sciences*, The Royal Society Publishing, v. 374, n. 2074, p. 20150308, 2016.

HALBACH, K. Design of permanent multipole magnets with oriented rare earth cobalt material. *Nuclear Instruments and Methods*, Elsevier, v. 169, n. 1, p. 1–10, 1980.

HAO, F.; QIU, P.; TANG, Y.; BAI, S.; XING, T.; CHU, H.-S.; ZHANG, Q.; LU, P.; ZHANG, T.; REN, D.; CHEN, J.; SHI, X.; CHEN, L. High efficiency bi2te3-based materials and devices for thermoelectric power generation between 100 and 300 °c. *Energy Environ. Sci.*, The Royal Society of Chemistry, v. 9, p. 3120–3127, 2016.

HAZELWOOD, J. *Special thermo magnetic motor device*. 2012. US8242662B2.

HOLMAN, J. P. *Experimental Methods for Engineers*. 6. ed. [S.l.]: McGraw-Hill, 1993. ISBN 978-0-07-0296664.

HONGBIN, W. *Thermomagnetic engine*. 2001. CN2419739Y.

HUNG, T. C.; SHAI, T. Y.; WANG, S. K. A review of organic rankine cycles (orcs) for the recovery of low-grade waste heat. *Energy*, v. 22, n. 7, p. 661–667, 1997.

HUR, S.; KIM, S.; KIM, H.-S.; KUMAR, A.; KWON, C.; SHIN, J.; KANG, H.; SUNG, T. H.; RYU, J.; BAIK, J. M.; SONG, H.-C. Low-grade waste heat recovery scenarios: Pyroelectric, thermomagnetic, and thermogalvanic thermal energy harvesting. *Nano Energy*, v. 114, p. 108596, 2023. ISSN 2211-2855.

INTERNATIONAL ENERGY AGENCY. *World Energy Outlook 2021*. 2021. Disponível em: <www.iea.org/>.

JIANG, C.; ZHU, S.; YU, G.; LUO, E.; LI, K. Numerical and experimental investigations on a regenerative static thermomagnetic generator for low-grade thermal energy recovery. *Applied Energy*, v. 311, p. 118585, 2022. ISSN 0306-2619.

JøRGENSEN, A. *Thermo-magnetischer motor*. 1994. WO199415393A1.

KALINA, A. I. Combined-cycle system with novel bottoming cycle. *Journal of Engineering for Gas Turbines and Power*, v. 105, n. 4, p. 718–723, 1983.

KALISKý, A. *Thermomagnetic engine*. 2006. SK3522004A3.

KANEKO, G.; CONCEIÇÃO, W.; COLMAN, F.; COCCI, A.; ALVES, C.; PUPIM, G.; KUBOTA, G.; OLIVEIRA, V.; TREVIZOLI, P. Design and experimental evaluation of a linear thermomagnetic motor using gadolinium: Preliminary results. *Applied Thermal Engineering*, Elsevier, v. 186, p. 116472, 2021.

KANEKO, G. H. *Motor do tipo Tesla puramente magnético*. 2019. BR202019022592-6U2.

KATAYAMA, A. *Non self-starting thermal magnetic energy recycling ferrite ring engine*. 1984. US4447736.

KEMENCZKY, M. *Termomagnetisk motor*. 1976. DK133719B.

KIM, Y.; MEHMOOD, M. U.; HAN, H. J.; KIM, Y. J.; OH, S. J.; LIM, S.-H. Reclaiming power potential from low temperature waste heat by thermomagnetic heat engines. *Energies*, MDPI, v. 15, n. 8, p. 2817, 2022.

KISHORE, R. A.; PRIYA, S. A review on design and performance of thermomagnetic devices. *Renewable and Sustainable Energy Reviews*, Elsevier, v. 81, p. 33–44, 2018.

KISHORE, R. A.; PRIYA, S. A review on low-grade thermal energy harvesting: Materials, methods and devices. *Materials*, v. 11, 2018.

KISHORE, R. A.; SINGH, D.; SRIRAMDAS, R.; GARCIA, A. J.; SANGHADASA, M.; PRIYA, S. Linear thermomagnetic energy harvester for low-grade thermal energy harvesting. *Journal of Applied Physics*, v. 127, n. 4, 2020.

KUO, C.-J. *Thermal magnetic engine and thermal magnetic engine system*. 2015. US8984885B2.

LHERITIER, P.; TORELLÓ, A.; USUI, T.; NOUCHOKGWE, Y.; ARAVINDHAN, A.; LI, J.; PRAH, U.; KOVACOVA, V.; BOUTON, O.; HIROSE, S. et al. Large harvested energy with non-linear pyroelectric modules. *Nature*, Nature Publishing Group UK London, v. 609, n. 7928, p. 718–721, 2022.

LI, C. *Permanent-magnet motor*. 2008. CN201018432Y.

LYUBINA, J. Magnetocaloric materials for energy efficient cooling. *Journal of Physics D: Applied Physics*, v. 50, n. 5, p. 053002, 2017.

MASAHIRO, N. *Opposing magnet type thermomagnetic engine*. 2002. JP2002281774A.

MASAHIRO, N. *Thermomagnetic engine*. 2009. JP4234235B2.

MEHMOOD, M. U.; KIM, Y.; AHMED, R.; LEE, J.; CHUN, W. Design and operation of a thermomagnetic engine for the exploitation of low-grade thermal energy. *International Journal of Energy Research*, Wiley Online Library, 2021.

MERKL, G. *Step-by-step thermo-magnetic motor*. 1969. US3445740.

MICHEL, H. C. C.; PIRES, A.; BRAGA, C. M. P.; COSTA, P. B.; CâMARA, M. A.; TREVIZOLI, P. V. Arquitetura de automação para medição de torque via servomotr. In: *Proceedings of the 17th Simpósio Brasileiro de Automação Inteligente*. [S.l.: s.n.], 2025.

MORIMOTO, T. *Thermomagnetic engine device and reversible thermomagnetic cycle device*. 2013. JP5278486B2.

MORRISH, A. H. *The Physical Principles of Magnetism*. Piscataway, NJ: IEEE Press, 2001. ISBN 9780780310060.

MURAKAMI, K.; NEMOTO, M. Some experiments and considerations on the behavior of thermomagnetic motors. *IEEE Transactions on Magnetics*, IEEE, v. 8, n. 3, p. 387–389, 1972.

MURATA, K. *Thermomagnetic engine*. 2009. JP2009203879A.

MURATA, K. *Thermomagnetic engine*. 2009. JP2009203875A.

NELLIS, G.; KLEIN, S. *Introduction to Engineering Heat Transfer*. 1st. ed. [S.l.]: Cambridge University Press, 2021. ISBN 9781107179530.

NIELSEN, K. K.; BAHL, C. R. H.; SMITH, A.; BJøRK, R.; PRYDS, N.; HATTEL, J. Detailed numerical modeling of a linear parallel-plate active magnetic regenerator. *International Journal of Refrigeration*, v. 32, p. 1478–1486, 2009.

NISHIKAWA, M. *Thermomagnetic engine*. 1997. JPH09268968A.

NORTON, R. P. *Thermo-magnetically operated device*. 1928. US1839165A.

PECHARSKY, V.; GSCHNEIDNER, J.; PECHARSKY, A.; TISHIN, A. Thermodynamics of the magnetocaloric effect. *Phys. Rev. B*, v. 64, 2001.

PECHARSKY, V. K.; GSCHNEIDNER JR., K. A. Giant magnetocaloric effect in $gd_5(si_2ge_2)$. *Phys. Rev. Lett.*, American Physical Society, v. 78, p. 4494–4497, 1997.

PIRC, A. *Rotary curie point magnetic engine*. 1973. US3743866.

PLANES, A.; MAñOSA, L.; ACET, M. Magnetocaloric effect and its relation to shape memory properties in ferromagnetic heusler alloys. *Journal of Physics: Condensed Matter*, v. 21, n. 23, p. 233201, 2009.

RIOS, H. C.; MICHEL, H. C. C.; TADIM, M.; SOLEDADE, L.; BASTOS, M.; SILVA, C. E. L.; TORRES, D. L. B.; CORRêA, L. dos S.; BRAGA, C. M. P.; CâMARA, M. A.; ROWE, A.; TREVIZOLI, P. V. Experimental evaluation of a linear thermomagnetic motor coupled to a spring mechanism. In: *Proceedings of the 20th Brazilian Congress of Thermal Sciences and Engineering*. [S.l.]: ABCM, 2024.

ROBINSON, T. W. *Thermo-magnetic engine*. 2011. AU2005205732A1.

SAGAWA, M.; FUJIMURA, S.; TOGAWA, N.; YAMAMOTO, H.; MATSUURA, Y. New material for permanent magnets on a base of nd and fe (invited). *Journal of Applied Physics*, AIP Publishing, v. 55, n. 6, p. 2083–2087, 1984.

SCHWARTZ, M. *Magnetic distortion motor*. 1922. US1431545A.

SILVA, C. E. L. Monografia (Bachelor's degree) — Universidade Federal de Minas Gerais, Belo Horizonte, 2022.

SILVA, C. E. L.; TREVIZOLI, P. V. Numerical analysis of the magnetic flux density profile impact on the total power produced by a linear thermomagnetic motor. In: *Proceedings of the 27th ABCM International Congress of Mechanical Engineering*. [S.l.]: ABCM, 2023.

SKOKOV, K.; KHOVAYLO, V.; MüLLER, K.-H.; MOORE, J.; LIU, J.; GUTFLEISCH, O. Magnetocaloric materials with first-order phase transition: thermal and magnetic hysteresis in $lafe_{11.8}si_{1.2}$ and $ni_{2.21}mn_{0.77}ga_{1.02}$. *Journal of Applied Physics*, v. 111, n. 7, p. 07A925, 2012.

SOLOMON, D. Improving the performance of a thermomagnetic generator by cycling the magnetic field. *Journal of Applied Physics*, v. 63, p. 915–921, 1988.

SPALDIN, N. A. *Magnetic Materials: Fundamentals and Applications*. 2nd. ed. Cambridge: Cambridge University Press, 2010. ISBN 9780521141963.

STEPANOVICH, B. V. *Thermomagnetic device*. 2001. RU2167338C1.

TAKAHASHI, Y.; YAMAMOTO, K.; NISHIKAWA, M. Fundamental performance of triple magnetic circuit type cylindrical thermomagnetic engine. *Electrical Engineering in Japan*, Wiley Online Library, v. 154, n. 4, p. 68–74, 2006.

TANAKA, T. *Thermomagnetic engine*. 2013. JP3185539U.

TANAKA, T. *Thermomagnetic engine*. 2014. JP3188724U.

TANAKA, T. *Thermomagnetic engine*. 2014. JP3191137U.

TESLA, N. *Thermo-Magnetic Motor*. 1889. US396121A.

TISHIN, A. M.; SPICHKIN, Y. I. *Magnetocaloric Effect and Its Applications*. Bristol and Philadelphia: Institute of Physics Publishing, 2003. ISBN 9780750307444.

TREVIZOLI, P. V. *Development of Thermal Regenerators for Magnetic Cooling Applications*. Tese (Doutorado) — Universidade Federal de Santa Catarina, 2015.

UNFCCC. *Paris Agreement under the United Nations Framework Convention on Climate Change*. 2015. <https://unfccc.int/sites/default/files/english_paris_agreement.pdf>. Adopted at COP 21, Paris, 12 December 2015.

VLADISLAV, V. *Thermomagnetic motor*. 1993. RU2002109C1.

VOLLERS, G. L. *Energy conversion system*. 1988. US4730137.

VOZNESENSKIJ, N. P. *Thermomagnetic motor*. 1947. SU72669A1.

WASKE, A.; DZEKAN, D.; SELLSCHOPP, K.; BERGER, D.; STORK, A.; NIELSCH, K.; FÄHLER, S. Energy harvesting near room temperature using a thermomagnetic generator with a pretzel-like magnetic flux topology. *Nature Energy*, Nature Publishing Group UK London, v. 4, n. 1, p. 68–74, 2019.

WEISS, P. La variation du ferromagnétisme avec la température. *Comptes Rendus*, v. 143, p. 1136–1139, 1906.

YOSHIDA, Y. *Thermal magnetic step motor device*. 1978. JPS54145909A.

ZEBARJADI, M.; ESFARJANI, K.; DRESSELHAUS, M. S.; REN, Z. F.; CHEN, G. Perspectives on thermoelectrics: from fundamentals to device applications. *Energy Environ. Sci.*, The Royal Society of Chemistry, v. 5, p. 5147–5162, 2012.

ZHANG, Y.; PHUONG, P. T. T.; ROAKE, E.; KHANBAREH, H.; WANG, Y.; DUNN, S.; BOWEN, C. Thermal energy harvesting using pyroelectric-electrochemical coupling in ferroelectric materials. *Joule*, Elsevier, v. 4, n. 2, p. 301–309, 2020.

A APPENDIX A : Magnetic Circuit Production and Assembly

The present appendix details the MC production and assembly process.

A.1 PRODUCTION

All the MC aluminum and steel parts were produced in-house, at the Laboratório de Usinagem e Automação from Universidade Federal de Minas Gerais, from raw materials. Conventional machining operations, mostly milling and drilling, were carried out employing the Machine Center (model ROMI Discovery 560) and some auxiliary tools, such as the bench drill, the band saw and sandpapers. Cutting tools and parameters were carefully selected to guarantee the achievement of the designed dimensional tolerances. High-Speed Steel (HSS) tools were employed for machining the aluminum parts, while carbide tools were utilized for working on the steel components. Also, appropriate cutting fluids were applied. Figure A.1 depicts some of the MC parts produced.

A.2 ASSEMBLY

The MC assembly was also carried out in-house, at the Laboratório de Sistemas Térmicos Emergentes - *Stream Lab* - from the Universidade Federal de Minas Gerais. Due to the strong magnetic forces involved, the assembly process requires careful handle and the use of auxiliary tools to assist the parts approaching.

A.2.1 PREPARATION

Before starting the assembly process, a Gaussmeter model LMP – HALL - 20k and a T1 Hall probe (GlobalMag) were employed to identify all the permanent magnet's remanence directions, as illustrated in Fig. A.2, securing its correct positioning within the MC.

Figure A.1 – Magnetic circuit parts produced: (a) long and short steel portions of the L-shaped set; (b) aluminum structural parts.

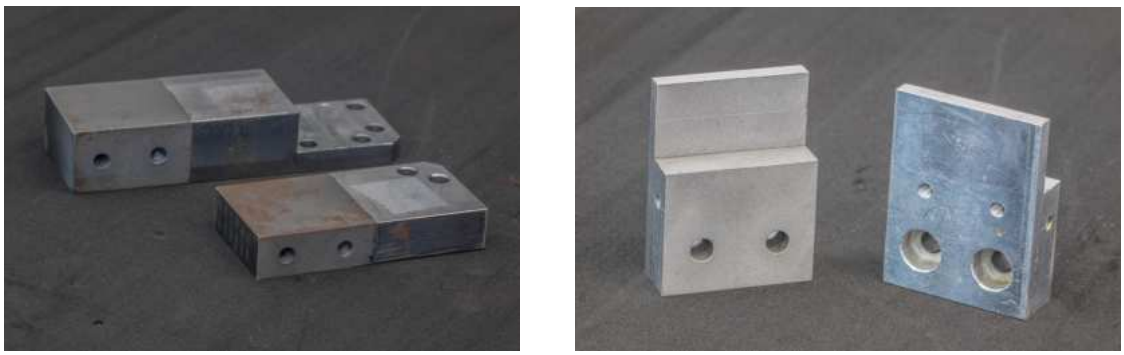

(a) (b)

Figure A.2 – Permanent magnet's remanence direction identification

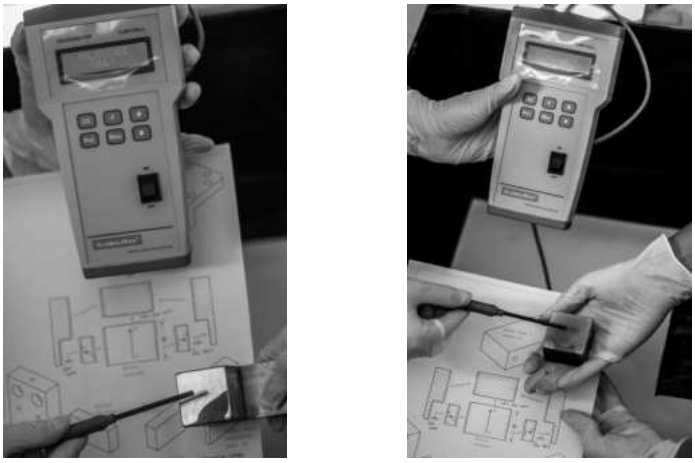

(a) (b)

Subsequent, all the surfaces to be bonded underwent a sand filling blasting procedure to remove the nickel protection layer from the permanent magnets and enhance the surfaces roughness, guaranteeing the best epoxy adhesion. The surfaces that would not be bonded were protected from the blasting with adhesive tape. The blasted surfaces, which can be seen in Figs. A.1 and A.3, were then cleaned and the parts were properly stored.

A.2.2 BONDING

The permanent magnets surfaces were bonded using an epoxy adhesive (3M Scotch Weld DP 460MS), which was applied with the assist of a pistol and a mixing nozzle and distributed on the surface with a spreader. Latex gloves were used during the entire procedure to prevent the adhesive of entering in contact with the skin. To ensure safety during the assembly, the entire bonding process was conducted inside a wooden case.

The bonding process involves several steps. Before starting, the remanence directions, already identified, are checked and the surfaces once again cleaned. Then, the epoxy is spread over the faces that will be joined together. Subsequently more epoxy is added to the joining edges between the parts, to ensure the bond quality. Finally, after full epoxy cure, the excess adhesive is removed, and the set is properly stored in wooden boxes specially designed for this purpose, depicted in Figure A.4.

Initially, the side concentrators permanent magnets were bonded to the aluminum parts, as shown in Figure A.5. For this procedure, steel parts were placed underneath the aluminum ones to attract the magnet and guarantee the surfaces joining until the epoxy full cure, as detailed in Figure A.5d. Then, the main permanent magnets were bonded to their respective steel parts. There was no need for the employment of any auxiliary tool, as the attraction force between the magnets and the steel was enough to keep them together until the adhesive full cure. The process is depicted in Figure A.6.

Subsequent, due to the strong repulsive magnetic forces involved, threaded bars were used for

coupling the main permanent magnets to the side concentrators structures, forming the portions of the L-shaped sets. The epoxy adhesive was spread over the clean surfaces and the structures were then approximated with the threaded bars help. Next, the threaded bars were replaced, one by one, by the screws responsible for the final assembly. Again, more epoxy was added to the joining edges between the parts and a straining clamp was employed to hold the set together until the epoxy full cure. Finally, the excess adhesive was removed, and the set was properly stored. Figure A.7 illustrates the described process.

After the bonding process was completed, the parts were painted so that the paint layer protects them from oxidation. For didactic purposes, the steel parts were painted in red, the aluminum parts in dark grey and the permanent magnets in chrome. The painted components are presented in Figure A.8.

A.2.3 FINAL ASSEMBLY

For the final assembly, the short and long portions of the L-shaped set were connected, as presented in Figure A.9. The long portion was attached to the working bench with a straining clamp while the short portion was coupled to it with the help of threaded bars for controlling the magnetic attraction force and assuring the right positioning. The threaded bars were then replaced by the screws responsible for the final assembly.

Two guideway slider blocks along with their respective aluminum parts are connected to the assembled L-shaped set. This parts are responsible for allowing the L-shaped structures to slide away from each other in the motor rack, easing the remaining components assembly. The described process is presented in Figure A.10.

Following, the triangular cross section steel part was connected to the lower L-shaped set using screws, as shown in Figure A.11a. Then, the lower set was attached to the working bench with a straining clamp while the upper set was coupled to the opposite end of the triangular cross section steel part with the help of threaded bars. To ensure the process safety, wood pieces were placed between the main permanent magnets. The last described process, depicted in Figure A.11, was carried out twice, completing the MC final assembly. The completed MC can be seen in Figure A.12.

Figure A.3 – Permanent magnets: (a) side concentrator prepared for the blasting process, with the adhesive tape protecting the not bonded surfaces and the identified remanence direction; (b) main permanent magnet prepared for the blasting process, with the adhesive tape protecting the not bonded surfaces and the identified remanence direction; (c) side concentrator blasted surfaces; (d) main permanent magnet blasted surfaces.

(a)

(b)

(c)

(d)

Figure A.4 – Wooden boxe specially designed for properly storing the permanent magnets.

Figure A.5 – Side concentrators and aluminum parts bonding process.

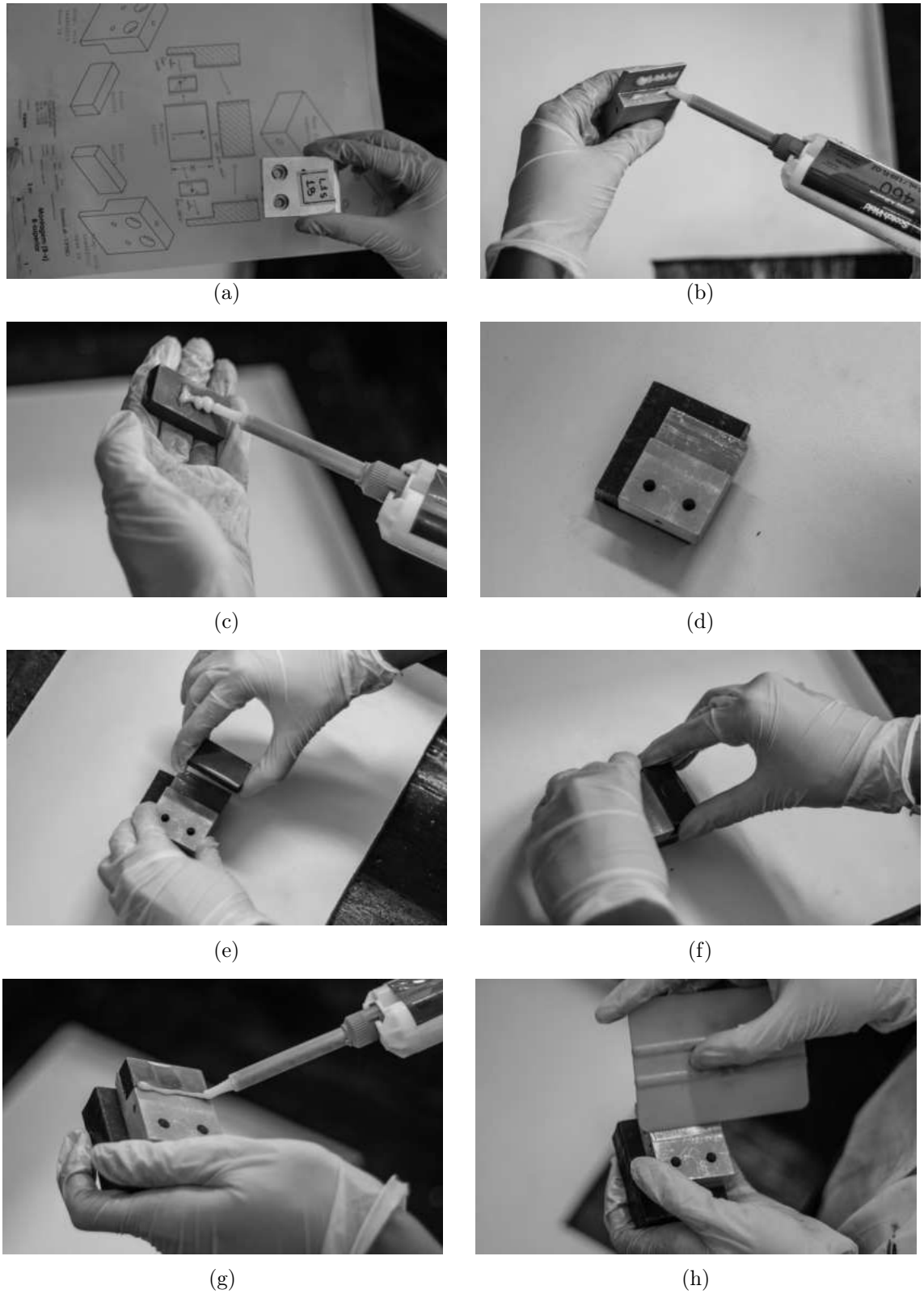

(a) (b)

(c) (d)

(e) (f)

(g) (h)

Figure A.6 – Main permanent magnets and steel parts bonding process.

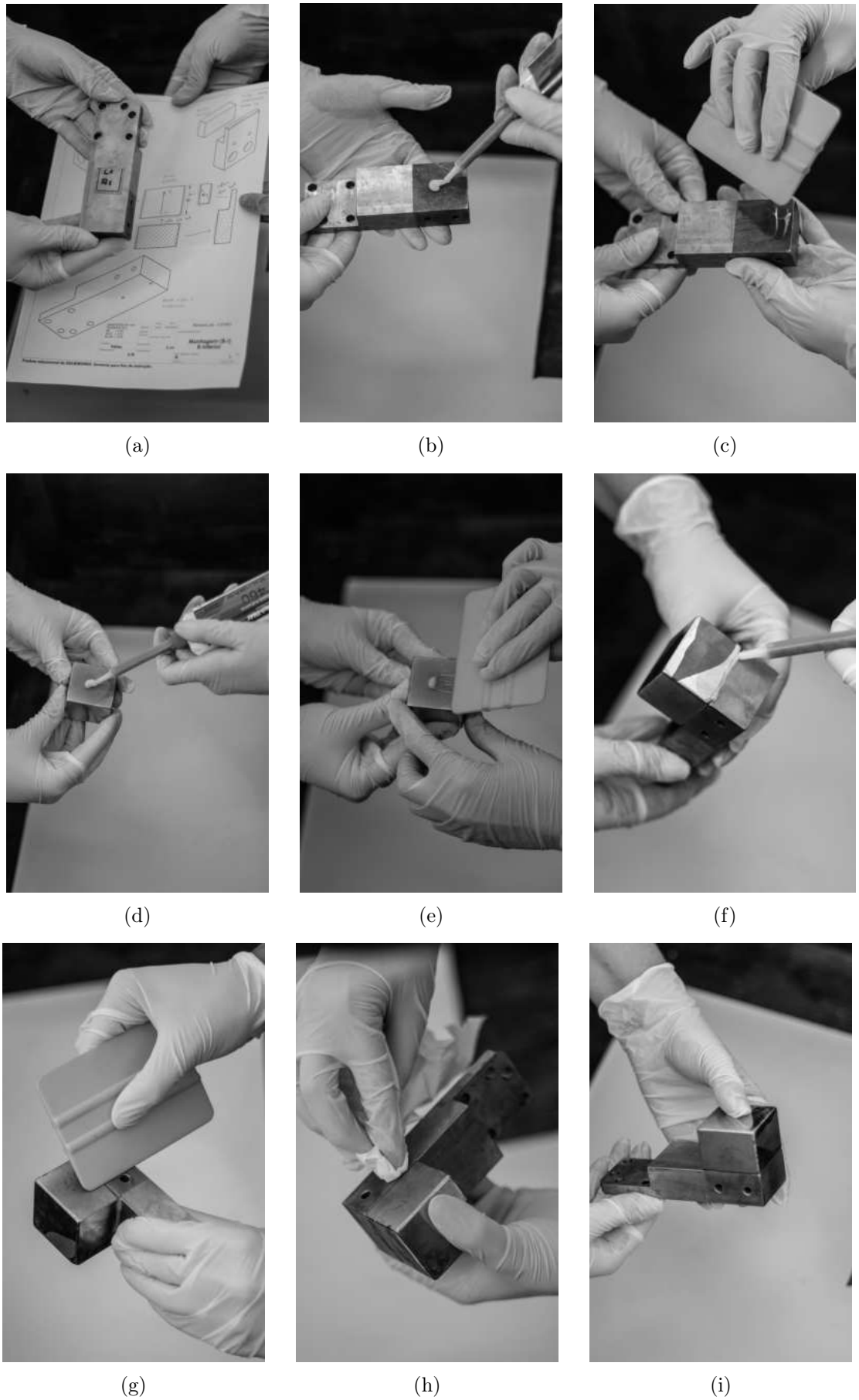

(a) (b) (c)

(d) (e) (f)

(g) (h) (i)

Figure A.7 – Assembly of the main permanent magnets to the side concentrators structures with the help of threaded bars.

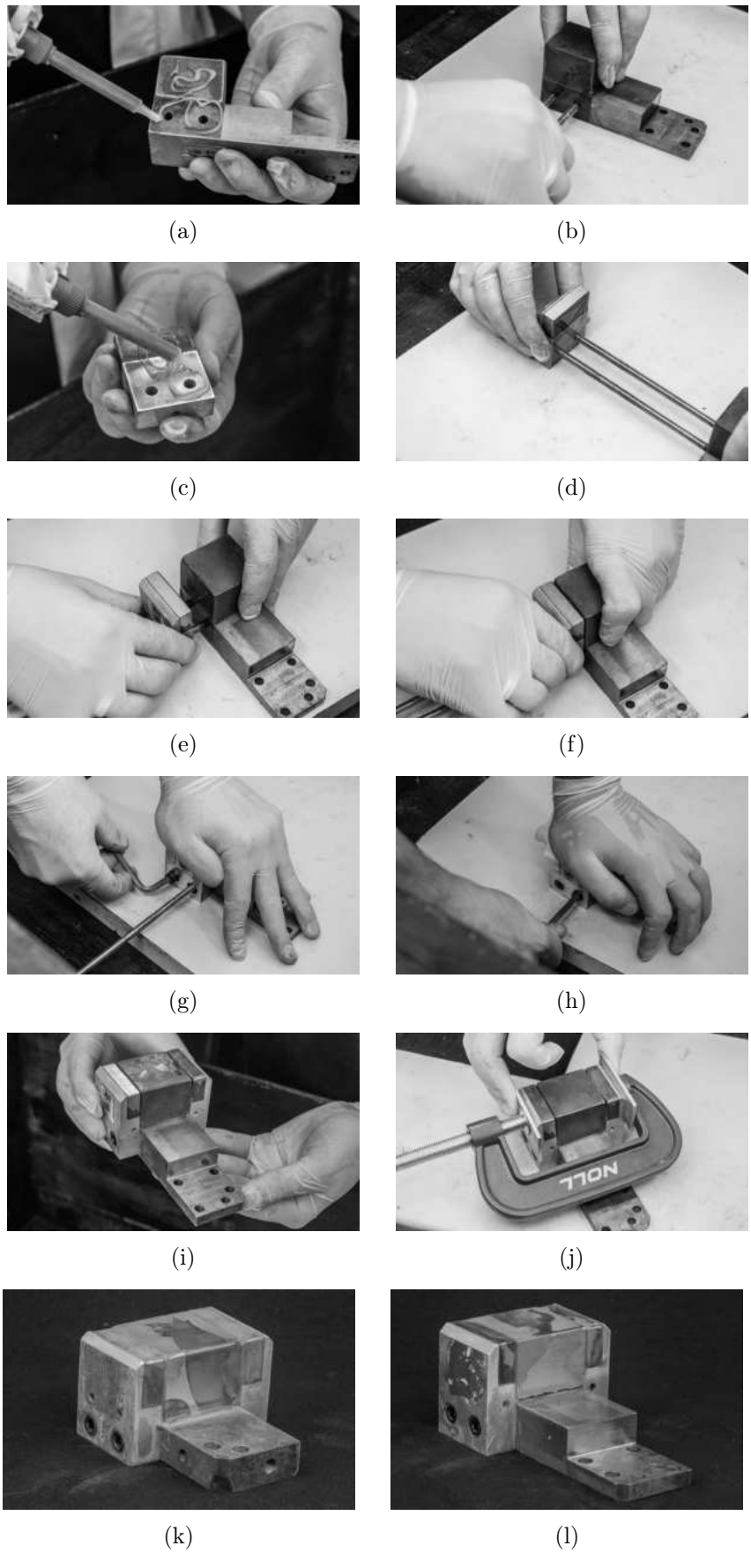

(a) (b)

(c) (d)

(e) (f)

(g) (h)

(i) (j)

(k) (l)

Figure A.8 – Magnetic circuit components after being painted. The red parts are made of steel, the dark grey parts are made of aluminum and the parts in chrome are the permanent magnets.

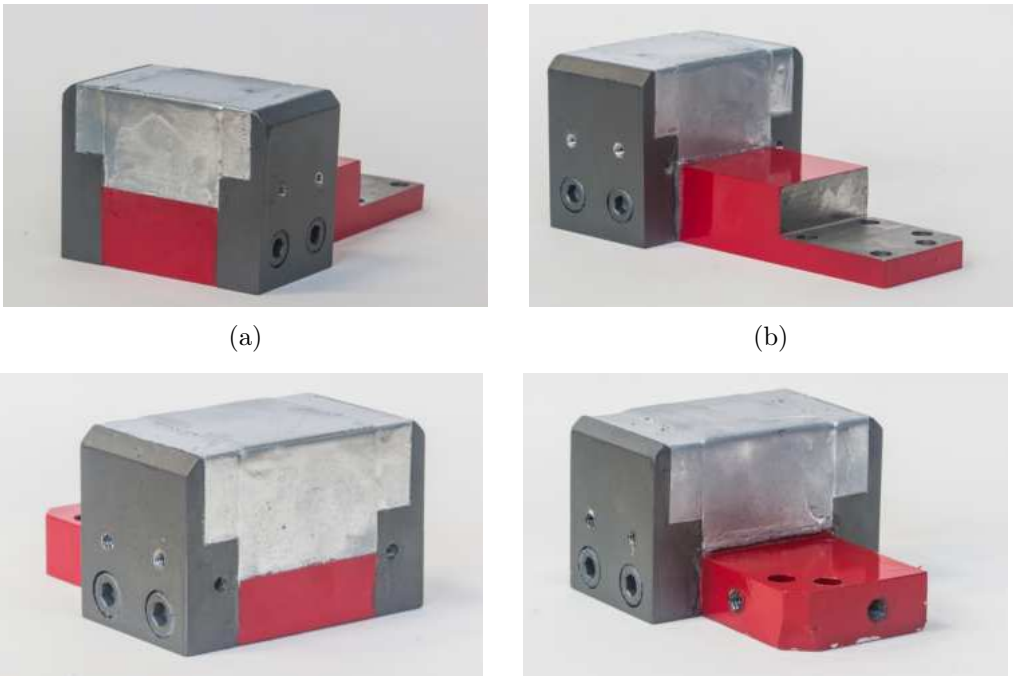

(a) (b)

(c) (d)

Figure A.9 – Assembly of the L-shaped set short and portions.

(a)

(b)

(c)

(d)

(e)

(f)

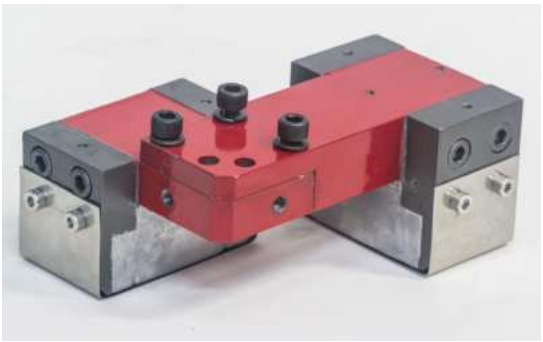

(g)

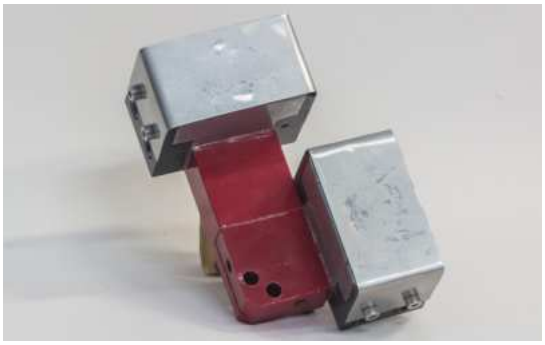

(h)

Figure A.10 – Assembly of the guideway slider blocks to the L-shaped set.

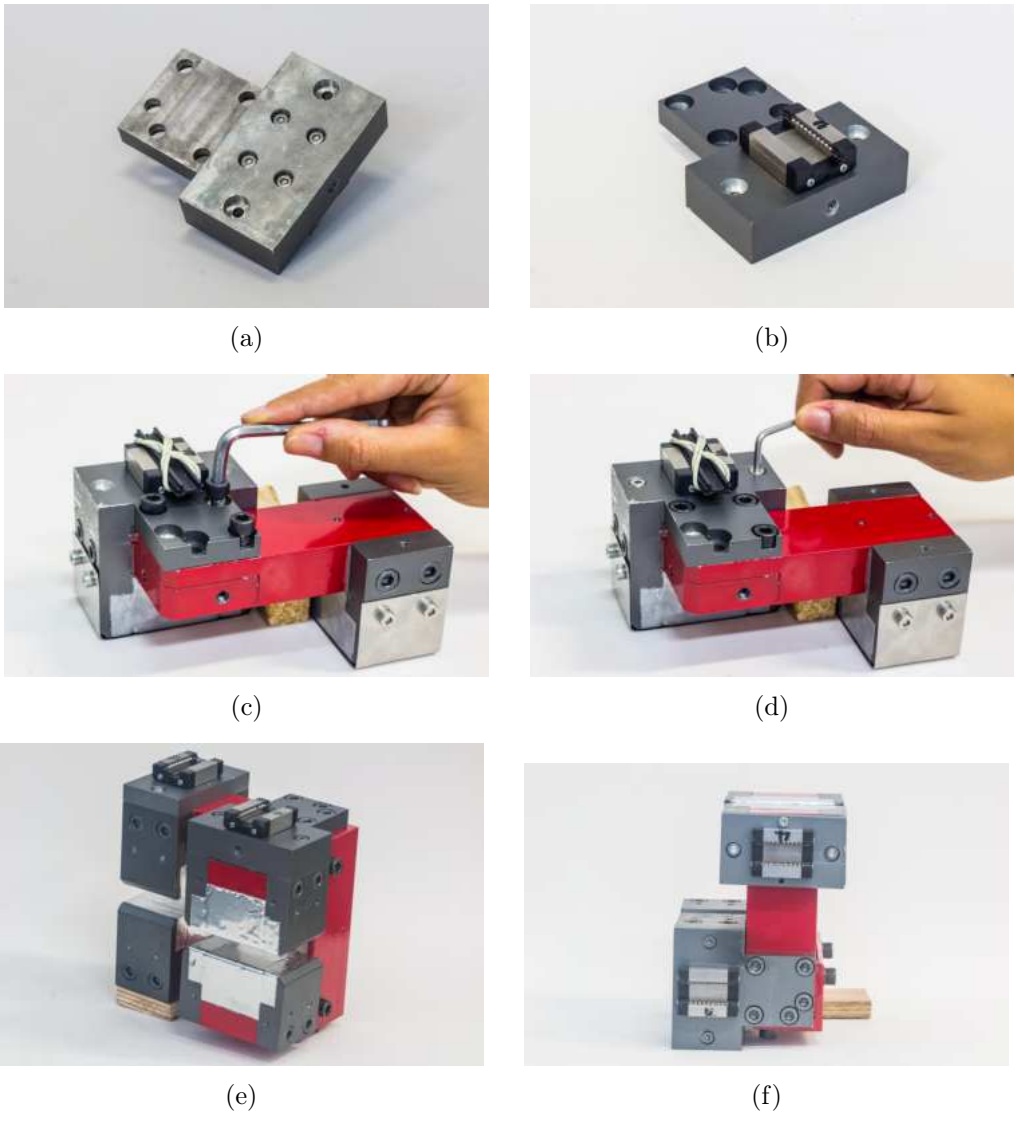

(a) (b)

(c) (d)

(e) (f)

Figure A.11 – L-shaped set final assembly.

(a)

(b)

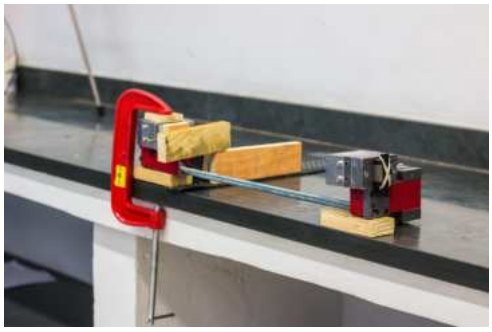

(c)

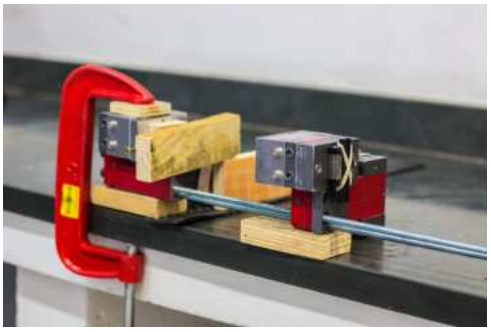

(d)

(e)

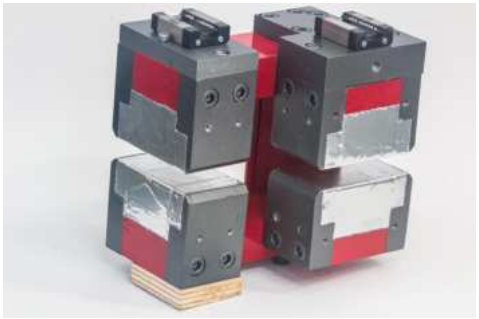

(f)

Figure A.12 – Completed magnetic circuit.

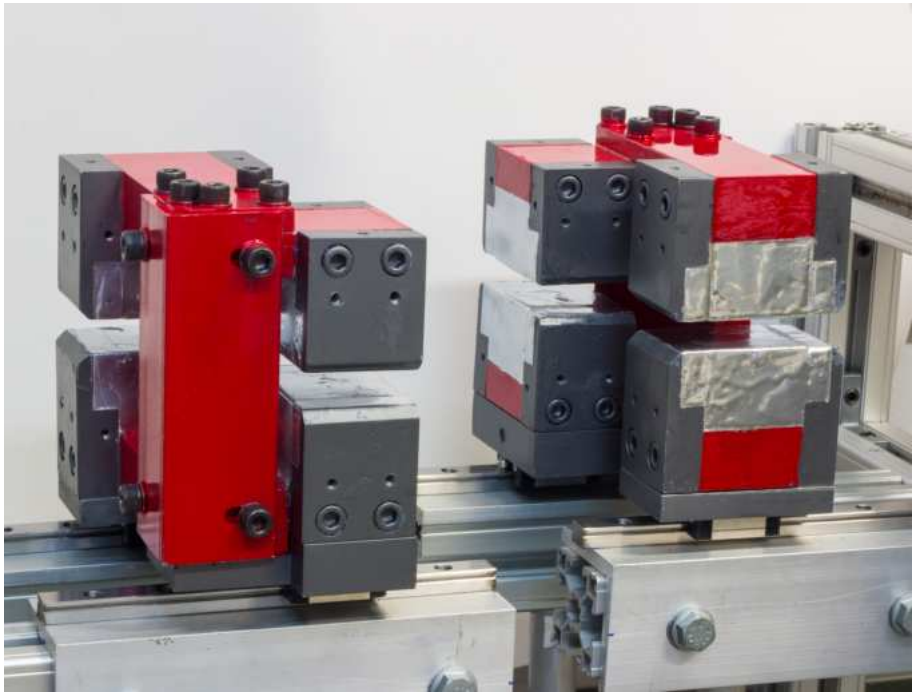

B APPENDIX B : Magnetic Circuit Experimental Characterization Results

As mentioned in Sec. 4.3.3, the magnetic flux density distribution was evaluated along a series of concentric circles plotted on a cross-sectional plane at the center of the air gap (plane $x-y$ at $z=0$). The measurement circumferences are illustrated by the blue circles in Fig. B.1, where the angular position corresponding to 0° is also indicated. The comparison between the experimental and simulated magnetic flux density values, obtained along the angular position at these circumferences are presented in Fig. 4.5. The parameter R denotes the radial distance between the inner concentrator's edge and the measurement circumference. The results for the circumference corresponding to $R = 30$ mm are not illustrated as they have already been presented in Fig. 5.4.

It is noted that the good agreement between the experimental results and the simulated values, previously observed at the center of the air gap, is also achieved at other radial positions. Additionally, the similarity between the results for R values ranging from 15 mm to 50 mm indicates that the desired uniform magnetic field distribution was attained.

Figure B.1 – Magnetic flux dentisty along the angular position at the center of the air gap: comparison between the experimental and numerical results.